Doctoral Dissertation, 2015

Imbibition of Micro-Patterned Surfaces

OCHANOMIZU UNIVERSITY
Advanced Science,
Graduate School of Humanities and Science

Marie TANI

March, 2016

Contents

Part I

Introduction

Chapter 1

Introduction

If someone likes coffee, he might have cried with a coffee spot on his important document. Coffee immediately penetrates into the paper on his desk when he falls down a cup of coffee on the desk. The coffee spot grows up with decreasing its velocity, and then finally stops growing. On the other hand, coffee probably becomes some spherical drops on a new tablecloth instead of penetrating into it when he falls down a cup of coffee on the tablecloth. As shown in these examples, wetting phenomena are familiar to us in daily life. Physical understanding of the dynamics of penetration or the controlling of wettabilities of materials is useful for us.

In nature, there are various surfaces that have some advantages in wettability. For example, lotus leaves repel well water drops with their super-hydrophobic surfaces. These super-hydrophobic surfaces are composed of the micro structures on the surfaces [1]. Micro structures enhance their wettabilities (hydrophobicity or hydrophilicity) compared with smooth surfaces made of the same materials; hydrophobic surfaces with micro structures become super-hydrophobic surfaces, and hydrophilic surfaces with the same structures become super-hydrophilic. In nature, not only lotus leaves, but also other plants [2], insects [3, 4], and animals [5, 6] have advantages in wettability originating from their micro-patterned surfaces.

On the other hand, a micro-patterned surfaces that imbibies liquid efficiently would lead to broad technological applications for liquid transport in areas ranging from microfluidics and biomedical mixing devices to fuel transport. Extensive studies on micro-patterned surfaces have been devoted for understanding and controlling specific wetting properties such as super-hydrophobicity [7] and

leophobicity [8]. Accordingly, such textured surfaces have allowed various applications, which include microfluidic devices [9, 10] such as liquid drop transport [11, 12, 13], controlled and patterned film coating [14, 15], and slippery pre-suffered surfaces [16, 17, 18]. In particular, combinatorial mixing of small amounts of liquids [19, 20, 21] has recently become more important than ever from various needs in chemistry, biology, medical sciences and pharmaceutical industries [10, 22, 23, 24] especially when liquids are expensive, as in the cases of DNA microarray [25, 26, 27, 28] and crystallization of proteins [29, 30].

Therefore, partly because of inspirations from nature and partly because of some demands in applied fields, in addition, owing to recent technological progress, wetting phenomena on micro-patterned surfaces have extensively been studied for both hydrophobic [7, 31] (or oleophobic [17]) and hydrophilic (or oleophilic) surfaces; in particular, imbibition of textured surfaces, which are surfaces covered with an array of micro pillars, has actively been studied. Quite frequently, the imbibition length z scales with the square root of elapsed time t in the viscous regime (in which gravity and inertia are negligible) [14, 32, 33], while another scaling law $z \sim t^{1/3}$ has also been found for capillary rise into corners [34, 35] and for imbibition of textured surfaces with short and round pillars [36]. Similar and other slowing down dynamics of imbibition have also been found in the cases of polygonal penetration into textured surfaces [14], ink spreading on papers [33], and so on.

Capillary rise in tubes, which may be one of the simplest cases of imbibition, was studied around 1900's, but imbibition dynamics has actively been studied still in these days because of its importance and various unsolved problems. Washburn published an article in 1921 [37], in which he reported a scaling law for the viscous regime of capillary rise; rising height z scales with the square root of elapsed time t, *i.e.*, $z \sim t^{1/2}$. This scaling law is well known as "Washburn's law", however, it is sometimes called "BCLW imbibition law", for example in [38], because the scaling law had also been reported by Bell and Cameron in 1906 [39], and Lucas in 1918 [40]. Although Bell and Cameron did not take into account liquid features, *e.g.*, surface tension and viscosity, Lucas did that and reported the same scaling law as Washburn's one. Anyway, after Washburn's article in 1921, many related works have been reported. Then, studying imbibition dynamics of textured surfaces has become more active than ever by virtue of the technological progress in these days, while there are still many unsolved problems; for example,

the difference between the exponents appearing in the scaling laws, $t^{1/2}$ and $t^{1/3}$, seems to be caused by geometries and sizes of the micro structures on the surfaces, but the cross-over between the exponents has yet to be found.

With this background, we experimentally and theoretically investigate imbibition of two different types of micro-patterned surfaces: one is the surface of a leg of a small animal (wharf roach) and surfaces mimicking it [6] (chapter 6), and the other "open capillaries" [41] (chapter 7). For the former, a unusual non-slowing down dynamics was found for capillary rise on the surface of the leg of a wharf roach (imbibition dynamics generally slows down with time). Motivated by this unusual feature, we fabricated artificial surfaces partially mimicking the surface of the leg, and then confirmed that a composite model developed by us well describes experimental results for capillary rise on the artificial surfaces. For the latter, we carried out experiments with open capillary channels whose cross-sections are rectangular shapes on a submillimeter scale, and then confirmed that our scaling laws well describe the experimental results both for the statics and dynamics of liquid column and for the dynamics of "precursor film". Furthermore, we demonstrated two applications in order to show capabilities of devices that utilize open channels and that are driven not by pumps but by capillary force.

The present thesis is organized as follows: in the rest of part I, capillary phenomena (chapter 2) and fluid dynamics (chapter 3) are briefly reviewed. Then, in part II devoted to previous works, we discuss the statics and dynamics of capillary rise (chapter 4) and previous works on imbibition of textured surfaces (chapter 5). Finally, in part III, we investigate imbibition of two different types of micro-patterned surfaces (chapter 6 and 7) as mentioned above.

Chapter 2

Capillary Phenomena

Capillary phenomena are phenomena that are observed at interfaces between two immiscible liquids or between liquid and gas. Capillarity plays important roles in various fields of science, industry, and so on. In this chapter, some fundamental examples of capillary phenomena are reviewed on the basis of the textbook [42].

2.1 Surface tension

A liquid flows readily; yet it can adopt extremely stable shapes. For example, a soap bubble or an oil droplet in water forms a perfect sphere if it is so small that the effect of gravity is negligible. The interface looks like a membrane on which some tension opposes deformations. This macroscopic "tension" is called "surface tension".

The origin of surface tension is, however on a microscopic scale, comparable to the sizes of molecules. Liquid is one of the three phases of matter (solid, liquid and gas states). The phase transition from gas to liquid occurs when the interactive force between molecules (intermolecular force) is stronger than thermal agitation. Here, we shall denote the cohesive energy of a molecule in a liquid bath by U. A molecule on the surface loses a half of the energy, *i.e.*, $U/2$, because it loses a half of molecules attracting it (Fig.2.1). When the size of a molecule is a, and thus the surface area per molecule is a^2, the energy loss per unit surface area is equal to

$$\gamma \sim \frac{U}{2a^2}. \tag{2.1}$$

Here, γ is called "surface energy" or "surface tension". Its unit is $\mathrm{J/m^2}$.

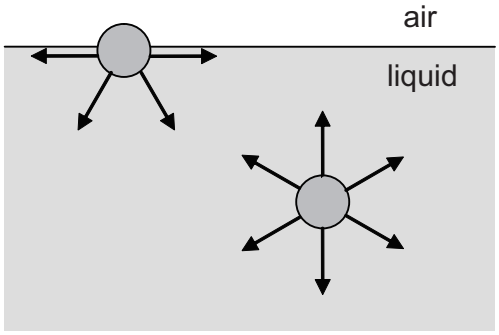

Fig. 2.1. a molecule in the liquid bath and that on the interface

The surface energy of most oils is about 20mJ/m^2 because interactions are of van der Waals type, which are comparable to thermal agitation, *i.e.*, $U \sim kT$. On the other hand, the surface energy of water is larger because of hydrogen bonds; $\gamma \simeq 72\text{mJ/m}^2$. Similar to these, the interfacial energy between two immiscible liquids A and B is characterized by interfacial tension γ_{AB}. The interfacial tension of water-oil surface is $\gamma_{wo} \simeq 50\text{mJ/m}^2$.

Here, we describe another meaning of surface tension on a macroscopic scale. In order to minimize the surface energy, liquids tend to minimize their exposed interfaces. Now, let us consider the situation in which some force is added to liquid and its surface increases by dA. Then, the required work δW is proportional to the number of molecules moved from the inside of the bath to the surface, *i.e.*, proportional to the increased surface area dA. Thus,

$$\delta W = \gamma \, dA, \tag{2.2}$$

where γ is surface tension. As a result, surface tension is also regarded as the energy needed to increase the surface by unit area.

Surface tension can be also regarded as a force per unit length (capillary force). This may be clearly understood from the fact that the unit of surface tension is rewritten as $\text{J/m}^2 = \text{N m/m}^2 = \text{N/m}$. Here, we describe the following experiment in which γ manifests itself as a force (Fig.2.2): (1) make a rectangular metal frame; (2) put a mobile rod on the rectangular frame; (3) dip the frame into a bath of soapy water and make a soap film inside of the frame (regions of both the left and right sides of the mobile rod); (4) break the soap film at one region (the right side of the mobile rod in Fig.2.2); (5) then, the mobile rod

moves spontaneously in the direction where the surface area of the film decreases (in the left in Fig.2.2). If we try to keep the film surface constant, we have to pull the film in the opposite direction (in the right in Fig.2.2) with a force F. When we move the mobile rod by a distance dx (see Fig.2.2), the liquid receives work

$$\delta W = F\ dx. \tag{2.3}$$

The increasing surface area dA is equal to $2ldx$, where l is the width of the frame defined in Fig.2.2 and the factor 2 reflects the presence of two interfaces: the upper and lower surfaces of the film, *i.e.*, the contact length of the mobile rod and the soap film is written as $2l$. Eq.(2.2) and eq.(2.3) lead to

$$F\ dx = \gamma\ 2l\ dx, \tag{2.4}$$

namely,

$$F = \gamma\ 2l. \tag{2.5}$$

Thus, we can regard γ as a force per unit length.

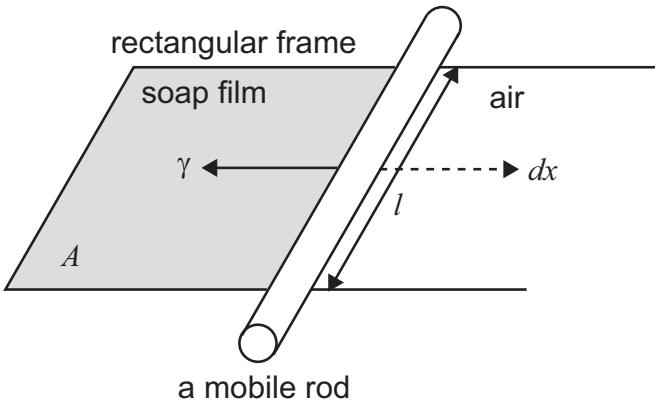

Fig. 2.2. Manifestation of surface tension γ as a force per unit length. The soap film (indicated as gray region) pulls the mobile rod put on a parallel side of the rectangular frame in order to decrease the surface area of the film.

2.2 Laplace pressure

Surface tension is the origin of the overpressure existing in the interior of drops and bubbles; pressure jumps up across a convex surface or interface. This pres-

sure jump is called "Laplace pressure".

Let us consider an oil drop in a water bath (Fig.2.3). In order to minimize the surface energy, the drop takes a spherical shape of radius R. As the radius increases from R to $R+dR$ (Fig.2.3), the work δW originating from the pressure and capillary force is described as

$$\delta W = -p_o \, dV_o - p_w \, dV_w + \gamma_{ow} \, dA, \tag{2.6}$$

where $dV_o = 4\pi R^2 dR = -dV_w$ and $dA = 8\pi R dR$ mean the increases in the volume and surface area of the drop, respectively. p_o and p_w are the pressures in oil and water, respectively, and γ_{ow} is the interfacial tension between oil and water. From the condition for mechanical equilibrium $\delta W = 0$, it follows

$$\Delta p = p_o - p_w = \frac{2\gamma_{ow}}{R}. \tag{2.7}$$

Eq.(2.7) implies that the smaller the drop, the greater its inner pressure.

In general, the hydrostatic pressure jump across the interface between two immiscible liquids, *i.e.*, Laplace pressure Δp, is written as

$$\Delta p = \gamma C = \gamma \left(\frac{1}{R} + \frac{1}{R'} \right), \tag{2.8}$$

where γ is the interfacial tension, $C = 1/R + 1/R'$ is the mean curvature and both R and R' are the radii of the curvature of the surface.

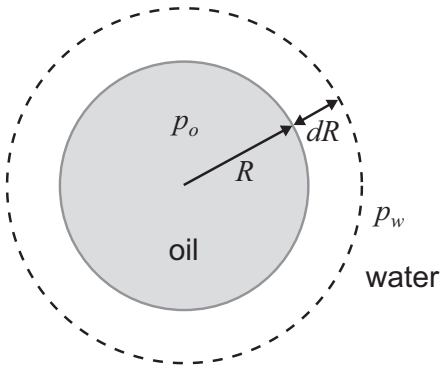

Fig. 2.3. A spherical oil drop in a water bath. The pressure in the oil drop p_o is larger than that in water p_w. The pressure jump $\Delta p = 2\gamma_{ow}/R$ is called "Laplace pressure".

2.3 Contact between three phases: wetting

When we put a water drop on a quite clean glass plate, the drop completely spreads over the plate. On the other hand, the same water drop put on a plastic plate remains stuck in place. Thus, there are two regimes of wetting: total wetting and partial wetting (Fig.2.4). They are distinguished by "spreading parameter";

$$S = E_D - E_W, \tag{2.9}$$

where E_D and E_W are the surface energies per unit area of dry and wet surfaces, respectively. By rewriting both energies as $E_D = \gamma_S$ and $E_W = (\gamma_{SL} + \gamma)$, spreading parameter S can be represented as

$$S = \gamma_S - (\gamma_{SL} + \gamma), \tag{2.10}$$

where γ_S, γ_{SL} and γ are the interfacial tensions of the solid-air, solid-liquid and liquid-air interfaces, respectively.

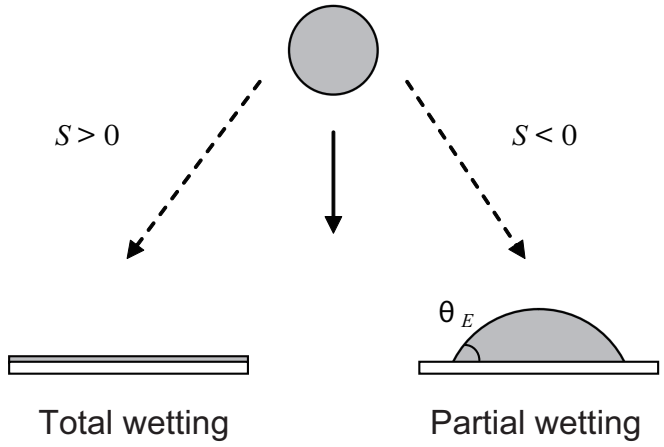

Fig. 2.4. Two wetting regimes for sessile drops: total (complete) wetting (left; spreading parameter $S > 0$) and partial wetting (right; $S < 0$).

When spreading parameter $S < 0$, the drop does not spread and forms at equilibrium a spherical cap resting on the substrate with an angle (Fig.2.4). This angle is called "(equilibrium) contact angle" θ_E. (In this thesis, we do not treat

"dynamical contact angle", and hence the contact angle θ always means the static or equilibrium contact angle θ_E. In addition, we do not consider "contact angle hysteresis" in this thesis. Details are found in Appendix A.) Furthermore, the surface is said to be a hydrophilic (or oleophilic) surface when $\theta_E < \pi/2$, and hydrophobic (or oleophobic) when $\theta_E > \pi/2$. On the other hand, when $S > 0$, the liquid spreads completely on the substrate in order to lessen its surface energy, and thus $\theta_E \simeq 0$.

The contact angle is determined by balancing the forces per unit length at the contact line (Fig.2.5), namely

$$\gamma \cos\theta_E = \gamma_S - \gamma_{SL}. \tag{2.11}$$

This formula is called "Young's law". By virtue of Young's law, the spreading parameter eq.(2.10) is written as

$$S = \gamma\left(\cos\theta_E - 1\right). \tag{2.12}$$

From this, it is clear that the contact angle θ_E can be defined only for the case of spreading parameter is non-positive; $S \leq 0$.

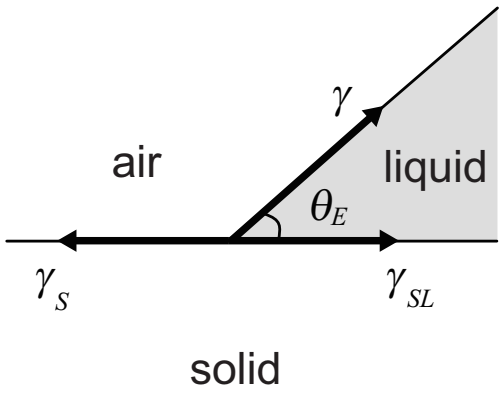

Fig. 2.5. Force balance at the contact line. γ_S, γ_{SL} and γ are the interfacial tensions of the solid-air, solid-liquid and liquid-air interfaces, respectively.

2.4 Capillary length κ^{-1}

When one of the ends of a thin tube is touched with a surface of a liquid bath, the liquid rises up inside the tube if the liquid wets well the tube, and stops rising at a certain height because of gravity. This phenomenon is called "capillary rise" (details are in chapter 4). As shown here, gravitational force becomes important only when the characteristic length of the phenomenon becomes larger than a particular length called "capillary length" κ^{-1}. Capillary length κ^{-1} is estimated by comparing Laplace pressure γ/κ^{-1} and hydrostatic pressure $\rho g \kappa^{-1}$ at a depth κ^{-1} in a liquid;

$$\kappa^{-1} = \sqrt{\frac{\gamma}{\rho g}}, \tag{2.13}$$

where ρ and g are the liquid density and the gravitational acceleration (*i.e.*, $g = 9.8$ m/s^2), respectively.

Values of capillary length κ^{-1} are about 2 mm: 2.7 mm for water and 1.5 mm for PDMS (polydimethylsiloxane). For characteristic length $r < \kappa^{-1}$, the effect of gravity is negligible, thus the liquid behaves as if it is in a non-gravitational environment. On the other hand, when $r > \kappa^{-1}$, the effect of gravity is important for the phenomenon, so that the regime is called "gravitational regime".

Chapter 3

Fluid Dynamics

In this chapter, we shall review the equations of motion of an incompressible viscous fluid and their solutions for some typical cases related to the present works. Contents of this chapter are based on textbooks [43, 44, 45].

3.1 Equation of motion of fluid

The equation of motion of a viscous fluid with unit volume are so-called "Navier-Stokes equations". In the case of an incompressible viscous fluid ($D\rho/Dt = 0$), Navier-Stokes equations are written as

$$\frac{D\boldsymbol{u}}{Dt} = -\frac{1}{\rho}\nabla p + \nu\nabla^2\boldsymbol{u} + \frac{1}{\rho}\boldsymbol{K}. \tag{3.1}$$

Here, we take into account the continuity equation, *i.e.*,

$$\frac{D\rho}{Dt} + \rho(\nabla\cdot\boldsymbol{u}) = 0 \tag{3.2}$$

or that for an incompressible fluid, *i.e.*,

$$\nabla\cdot\boldsymbol{u} = 0. \tag{3.3}$$

Here, $\boldsymbol{u}$, ρ, p and $\nu = \eta/\rho$ are the velocity, density, pressure and kinetic viscosity, respectively, of the fluid. $\boldsymbol{K}$ is the external force per unit volume. D/Dt is time derivative in the Lagrange description, *i.e.*, the sum of the partial differentiation in time and convective terms;

$$\frac{D\boldsymbol{u}}{Dt} = \frac{\partial\boldsymbol{u}}{\partial t} + (\boldsymbol{u}\cdot\nabla)\boldsymbol{u}, \tag{3.4}$$

or

$$\frac{D}{Dt} = \frac{\partial}{\partial t} + (\boldsymbol{u} \cdot \nabla). \tag{3.5}$$

We can describe the motion of an incompressible viscous fluid with initial and boundary conditions in principle since the numbers of unknown functions (three components of $\boldsymbol{u}$ and p) and equations (three components of eq.(3.1) and eq.(3.3)) are equal.

3.2 Typical examples

Now, we shall analytically solve the incompressible Navier-Stokes equations for a few fundamental and typical examples.

At first, we shall consider a uni-directional flow of velocity $\boldsymbol{u} = (u, 0, 0)$ without external force, *i.e.*, $\boldsymbol{K} = 0$. Here, we take a rectangular coordinate system $\boldsymbol{x} = (x, y, z)$. In this case, the continuity equation eq.(3.3) becomes $\partial u/\partial x = 0$, namely u does not depend on x. In addition, y and z components of eq.(3.1) become $\partial p/\partial y = 0$ and $\partial p/\partial z = 0$, respectively, namely p depends only on x. Thus, x component of eq.(3.1) is written as

$$\frac{\partial u}{\partial t} = -\frac{1}{\rho}\frac{\mathrm{d}p}{\mathrm{d}x} + \nu\left(\frac{\partial^2 u}{\partial y^2} + \frac{\partial^2 u}{\partial z^2}\right). \tag{3.6}$$

Since u is independent of x and p is independent of y and z, each term should spatially be constant and should be written as a function only of time;

$$\frac{\partial u}{\partial t} - \nu\left(\frac{\partial^2 u}{\partial y^2} + \frac{\partial^2 u}{\partial z^2}\right) = -\frac{1}{\rho}\frac{\mathrm{d}p}{\mathrm{d}x} = \alpha(t). \tag{3.7}$$

Here, $\alpha(t)$ is an arbitrary function of t. In the case of a steady flow ($\partial u/\partial t = 0$), eq.(3.7) becomes

$$\left(\frac{\partial^2 u}{\partial y^2} + \frac{\partial^2 u}{\partial z^2}\right) = \frac{1}{\eta}\frac{\mathrm{d}p}{\mathrm{d}x} = -\frac{\alpha}{\nu}, \tag{3.8}$$

where α is constant.

As a result, the velocity of a uni-directional flow, *i.e.*, $\boldsymbol{u} = (u(y, z, t), 0, 0)$, is analytically determined as the solution of eq.(3.7) or eq.(3.8) with some initial and boundary conditions.

3.2.1 2D Couette flow

Let us consider a two dimensional steady flow. If we take z-axis such that the flow velocity is constant in the z direction, eq.(3.8) becomes

$$\frac{\mathrm{d}^2 u}{\mathrm{d}y^2} = \frac{1}{\eta}\frac{\mathrm{d}p}{\mathrm{d}x} = -\frac{\alpha}{\nu}. \tag{3.9}$$

Its general solution is instantly obtained as

$$u(y) = C_1 + C_2 y - \frac{\alpha}{2\nu} y^2, \text{ and } p(x) = p_0 - \alpha\rho x, \tag{3.10}$$

where C_1, C_2 and p_0 are constants of integration determined from the boundary conditions. If the flow is enclosed between two smooth parallel planes at $y = y_1, y_2$ ($y_2 > y_1$) and the planes move in the x direction with constant velocities U_1 and U_2, respectively, we can determine C_1 and C_2 as follows:

$$C_1 = \frac{U_1 y_2 - U_2 y_1}{y_2 - y_1} - \frac{\alpha}{2\nu} y_1 y_2, \text{ and } C_2 = \frac{U_2 - U_1}{y_2 - y_1} + \frac{\alpha}{2\nu}(y_1 + y_2). \tag{3.11}$$

Here, we imposed a non-slip boundary condition, namely the liquid moves together with the planes, on the boundary.

In the case of no pressure gradient ($\alpha = 0$), and planes $y_1 = -d$ and $y_2 = d$ ($d > 0$) move with velocities $U_1 = -U_0$ and $U_2 = U_0$ ($U_0 > 0$) as depicted in Fig.3.1, eq.(3.10) with eq.(3.11) becomes

$$u(y) = U_0 \frac{y}{d}, \text{ and } p = p_0. \tag{3.12}$$

In this case, the velocity profile is linear as shown in Fig.3.1. The flow is called two dimensional "Couette flow".

3.2.2 2D Poiseuille flow

In the case of non-zero pressure gradient ($\alpha > 0$), and both planes $y_1 = -d$ and $y_2 = d$ do not move ($U_1 = U_2 = 0$) as shown in Fig.3.2, eq.(3.10) with eq.(3.11) becomes

$$u(y) = U_0 \left\{ 1 - \left(\frac{y}{d} \right)^2 \right\}, \quad U_0 = \frac{\alpha d^2}{2\nu}, \text{ and } p(x) = p_0 - \frac{2\eta U_0}{d^2} x. \tag{3.13}$$

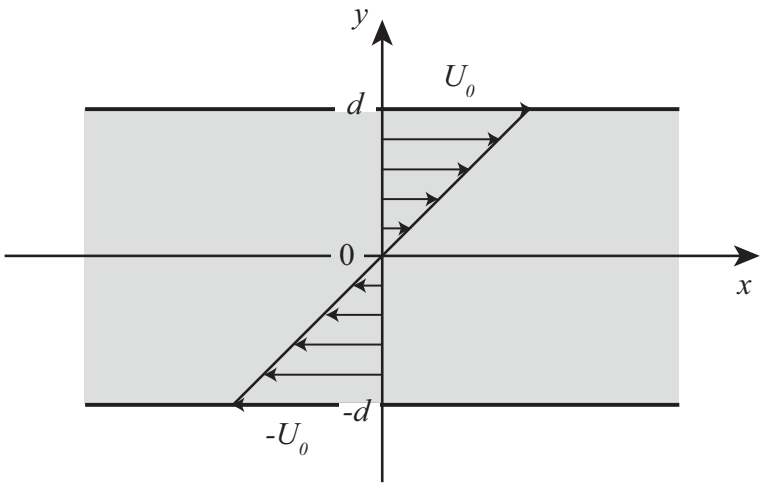

Fig. 3.1. Two-dimensional Couette flow

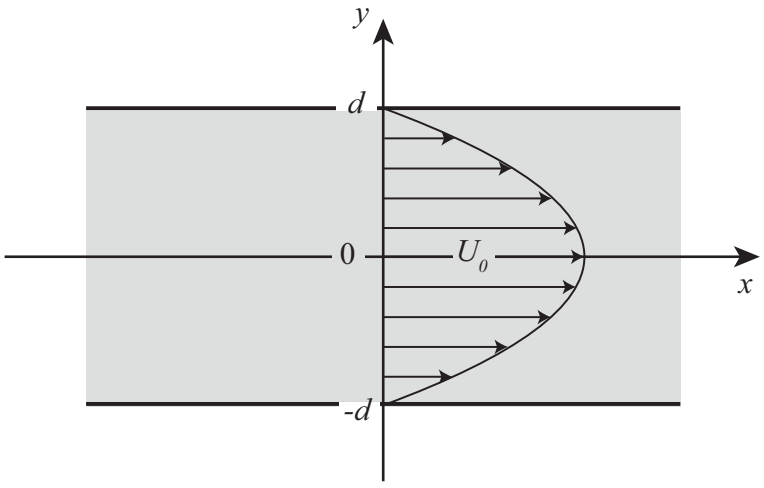

Fig. 3.2. Two-dimensional Poiseuille flow

In this case, the velocity profile is parabolic as shown in Fig.3.2. This flow is called two dimensional "Poiseuille flow".

In general, two-dimensional uni-directional steady flows are described as superpositions of two-dimensional Couette flows and two-dimensional Poiseuille flows.

3.2.3 (3D) Hagen-Poiseuille flow

Let us consider a three-dimensional steady flow in a pipe of an arbitrary cross-section (the same along the axis of the pipe, however). We use a cylindrical coordinate (x, r, θ) instead of a rectangular coordinate (x, y, z). Let the x-axis be the direction of the axis of the pipe. With cylindrical symmetry ($\partial u/\partial\theta = 0$), eq.(3.8) becomes

$$\frac{\mathrm{d}^2 u}{\mathrm{d}r^2} + \frac{1}{r}\frac{\mathrm{d}u}{\mathrm{d}r} = \frac{1}{\eta}\frac{\mathrm{d}p}{\mathrm{d}x} = -\frac{\alpha}{\nu}, \tag{3.14}$$

where α is constant. Its general solution is

$$u(r) = C_1 + C_2 \log r - \frac{\alpha}{4\nu} r^2, \text{ and } p(x) = p_0 - \alpha\rho x, \tag{3.15}$$

where C_1, C_2 and p_0 are constants of integration determined from the boundary conditions. The continuity of the velocity yields $C_2 = 0$. We take the non-slip boundary condition on the wall of the pipe, namely $u = 0$ at $r = a$ with the radius a of the pipe. In the case of non-zero pressure gradient ($\alpha > 0$), eq.(3.15) becomes

$$u(r) = U_0 \left\{ 1 - \left(\frac{r}{a} \right)^2 \right\}, \quad U_0 = \frac{\alpha a^2}{4\nu}, \text{ and } p = p_0 - \frac{4\eta U_0}{a^2}\, x. \tag{3.16}$$

The velocity profile is paraboloid as shown in Fig.3.3. This three-dimensional flow is called "Hagen-Poiseuille flow" or "Poiseuille flow".

3.3 Viscous friction

In this section, we shall estimate the mean velocity and viscous frictional force of 2D and 3D Poiseuille flows.

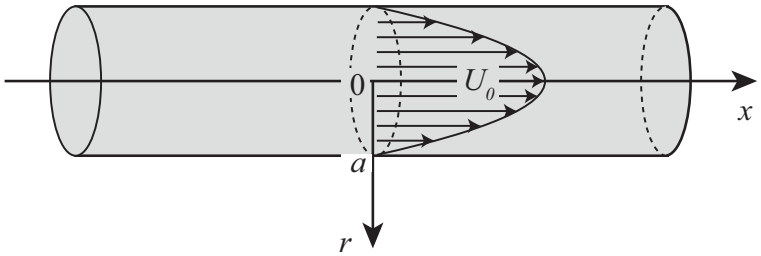

Fig. 3.3. (Three-dimensional) Poiseuille flow or Hagen-Poiseuille flow

3.3.1 2D Poiseuille flow

The mean velocity (the velocity averaged in the yz-plane in Fig.3.2, *i.e.*, averaged in the cross-section of the flow) is obtained as

$$\langle u \rangle = \frac{1}{2d}\int_{-d}^{d} u(y)\mathrm{d}y = \frac{2}{3}U_0 = \frac{\alpha d^2}{3\nu}. \tag{3.17}$$

Here, $u(y)$ and U_0 in eq.(3.13) were used. Thus, the pressure gradient α is written as

$$\alpha = \frac{3\nu\langle u \rangle}{d^2}. \tag{3.18}$$

From the definition of α (eq.(3.8)), the viscous frictional force working on the volume $2dxz$ is estimated as follows:

$$\begin{aligned} F_\eta &= -\iiint \left(\frac{\mathrm{d}p}{\mathrm{d}x}\right)\mathrm{d}x\mathrm{d}y\mathrm{d}z \\ &= \iiint \rho\alpha\mathrm{d}x\mathrm{d}y\mathrm{d}z \\ &= \rho\frac{3\nu\langle u \rangle}{d^2}2dxz \\ &= 6\eta\frac{\langle u \rangle}{d}xz. \end{aligned} \tag{3.19}$$

Therefore the viscous frictional force per unit volume is

$$f_\eta = 3\eta\frac{\langle u \rangle}{d^2}. \tag{3.20}$$

3.3.2 (3D) Poiseuille flow

In the case of (3D) Poiseuille flow (Hagen-Poiseuille flow), the mean velocity $\langle u \rangle$ is obtained as

$$\langle u \rangle = \frac{1}{\pi a^2} \int_0^a u(r)\ 2\pi r \mathrm{d}r = \frac{1}{2} U_0 = \frac{\alpha a^2}{8\nu}. \tag{3.21}$$

Here, $u(r)$ and U_0 in eq.(3.16) were used. Thus, the pressure gradient α is written as

$$\alpha = \frac{8\nu \langle u \rangle}{a^2}. \tag{3.22}$$

From the definition of α (eq.(3.14)), the viscous frictional force working on the volume $\pi a^2 x$ is estimated as follows:

$$\begin{aligned} F_\eta &= -\iiint \left(\frac{\mathrm{d}p}{\mathrm{d}x} \right) r \mathrm{d}r \mathrm{d}\theta \mathrm{d}x \\ &= \rho \frac{8\nu \langle u \rangle}{a^2} \pi a^2 x \\ &= 8\pi\eta \langle u \rangle x, \end{aligned} \tag{3.23}$$

or

$$F_\eta = 4\eta \frac{\langle u \rangle}{a} 2\pi a x. \tag{3.24}$$

The latter expression means that the viscous friction is proportional to the viscosity η, the velocity gradient $\langle u \rangle / a$ and the lateral surface $2\pi a x$ of the pipe. Hence the viscous frictional force per unit volume is

$$f_\eta = 8\eta \frac{\langle u \rangle}{a^2}. \tag{3.25}$$

Furthermore, the flow rate is written as

$$Q = \langle u \rangle\ \pi a^2 \ = \ \frac{\pi \alpha a^4}{8\nu} \ = \ -\frac{\pi a^4}{8\eta} \frac{\mathrm{d}p}{\mathrm{d}x}. \tag{3.26}$$

This implies that the flow rate is proportional to the pressure gradient $\mathrm{d}p/\mathrm{d}x$, a^4 with the pipe radius a, and η^{-1} with viscosity η. This formula was independently founded by Hagen (1839) and Poiseuille (1840, 1841) from experiments. Thus, the formula is called "Hagen-Poiseuille law".

3.4 Lubrication approximation

In this section, we shall approximately solve Navier-Stokes equations with "lubrication approximation".

Let us consider a thin and incompressible film as depicted in Fig.3.4. The film thickness e is quite small compared with the variations in other directions. Here, we assume that the velocity of the flow depends only on z, and thus

$$\nabla^2 \boldsymbol{u} = \frac{\partial^2 \boldsymbol{u}}{\partial z^2}. \tag{3.27}$$

This assumption is reasonable since the velocity of thin flim is limited to a small value with a non-slip condition at the liquid-solid interface. Furthermore, the inertia term in Navier-Stokes equations is negligible compared with the viscous term in most cases when the velocity is small. Thus, Navier-Stokes equations (eq.(3.1)) become

$$\begin{cases} \dfrac{\partial^2 u_x}{\partial z^2} = \dfrac{1}{\eta}\dfrac{\partial p}{\partial x} = -\dfrac{\alpha(t)}{\nu}, \\ \dfrac{\partial^2 u_y}{\partial z^2} = \dfrac{1}{\eta}\dfrac{\partial p}{\partial y} = -\dfrac{\beta(t)}{\nu}, \end{cases} \tag{3.28}$$

where α and β are functions only of time t. Here, we considered the case of non-external force; $\boldsymbol{K} = \boldsymbol{0}$. Such an approximation used here is called "lubrication approximation".

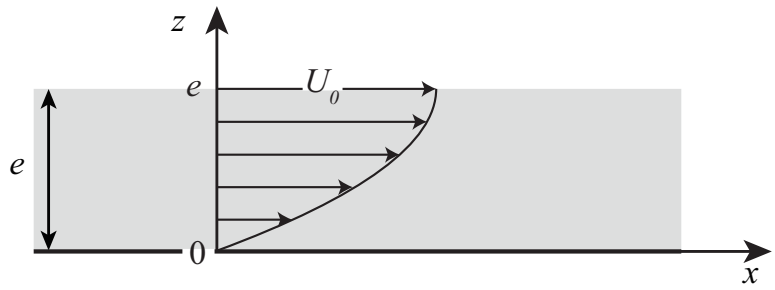

Fig. 3.4. Poiseuille flow in a thin liquid film whose thickness is e.

If we take the x-axis in the direction of the flow, *i.e.*, we write the flow velocity

as $\boldsymbol{u} = (u(z), 0, 0)$, eq.(3.28) becomes

$$\frac{\partial^2 u}{\partial z^2} = \frac{1}{\eta}\frac{\partial p}{\partial x} = -\frac{\alpha(t)}{\nu}. \tag{3.29}$$

Now, we can analytically solve this equation with the boundary conditions: $u = 0$ at $z = 0$ and $\partial u/\partial z = 0$ at $z = e$. As a result, we obtain as follows:

$$u(z,t) = U_0 \left\{ 1 - \left(\frac{e-z}{e} \right)^2 \right\}, \quad U_0 = \frac{\alpha(t) e^2}{2\nu}, \text{ and } p(x,t) = p_0 - \frac{2\eta U_0}{e^2} x. \tag{3.30}$$

Thus, the mean velocity (the velocity averaged in the yz-plane in Fig.3.4) is obtained as

$$\langle u(t) \rangle \;=\; \frac{1}{e}\int_0^e u(z,t)\mathrm{d}z \;=\; \frac{2}{3}U_0 \;=\; \frac{\alpha(t)}{3\nu}e^2 = -\frac{e^2}{3\eta}\frac{\partial p}{\partial x}. \tag{3.31}$$

Then, the viscous frictional force working for the volume xye is estimated as

$$F_\eta \;= -\iiint \left(\frac{\partial p(t)}{\partial x} \right) \mathrm{d}x\mathrm{d}y\mathrm{d}z \;=\; \frac{3\eta\langle u(t)\rangle}{e^2} xye \;=\; 3\eta\frac{\langle u(t)\rangle}{e} xy, \tag{3.32}$$

and the viscous frictional force per unit volume is written as

$$f_\eta = 3\eta\frac{\langle u(t)\rangle}{e^2}. \tag{3.33}$$

Furthermore, the flow rate Q is written as

$$Q(t) = \langle u(t)\rangle exy \;=\; -\frac{e^3 xy}{3\eta}\,\frac{\partial p}{\partial x}. \tag{3.34}$$

Finally, it is to be noted that Stokes equations are written as

$$\frac{\partial \boldsymbol{u}}{\partial t} = -\frac{1}{\rho}\nabla p + \nu\nabla^2 \boldsymbol{u}. \tag{3.35}$$

Here, only the convective term ($\sim u^2$) of Navier-Stokes equations is ignored in the case of small velocity u (Stokes approximation). When the flow is steady, the equation becomes the same as eq.(3.8).

Part II

Previous Study

Chapter 4

Capillary Rise

"Capillary rise" might be one of the most well-known phenomena. When one makes an end of a narrow tube touched with mostly wetting liquid, the liquid rises up inside the tube, and then the liquid stops rising at a certain height. The statics and dynamics of this phenomenon have experimentally and theoretically been understood. In this chapter, we theoretically discuss the statics of the above phenomenon, *i.e.*, the final height of the liquid rising, and the dynamics of the phenomenon in the viscous regime by three ways: force balance, energy minimization and Navier-Stokes equations.

4.1 Force balance

In this section, we describe the statics and dynamics of capillary rise by discussing force balance.

The driving force of the phenomenon is capillary force, which is written as

$$F_\gamma = 2\pi\gamma R\cos\theta, \tag{4.1}$$

where γ is the surface tension, R is the radius of the capillary, and θ is the contact angle between the liquid and the tube at the top of the proceeding liquid column. The liquid stops rising when gravitational force F_g of the liquid inside the tube equals to the capillary force F_γ. F_g is written as

$$F_g = \rho g\pi R^2 h. \tag{4.2}$$

Here, we assumed that the volume of the meniscus is negligible, thus the liquid inside the tube was regarded as a liquid column of the radius R and the height

h. This is a reasonable assumption when the final height h is sufficiently larger than the capillary radius R, *i.e.*, $h \gg R$. ρ is the density of the liquid and g is the gravitational acceleration. By balancing F_γ and F_g, the final height h is given by

$$h = \frac{2\gamma \cos\theta}{\rho g R}. \tag{4.3}$$

This is called "Jurin's law". From this law, it follows that the final height h is inversely proportional to the capillary radius R. In the case of complete wetting, namely when the contact angle θ is zero, the final height becomes

$$h = \frac{2\gamma}{\rho g R}. \tag{4.4}$$

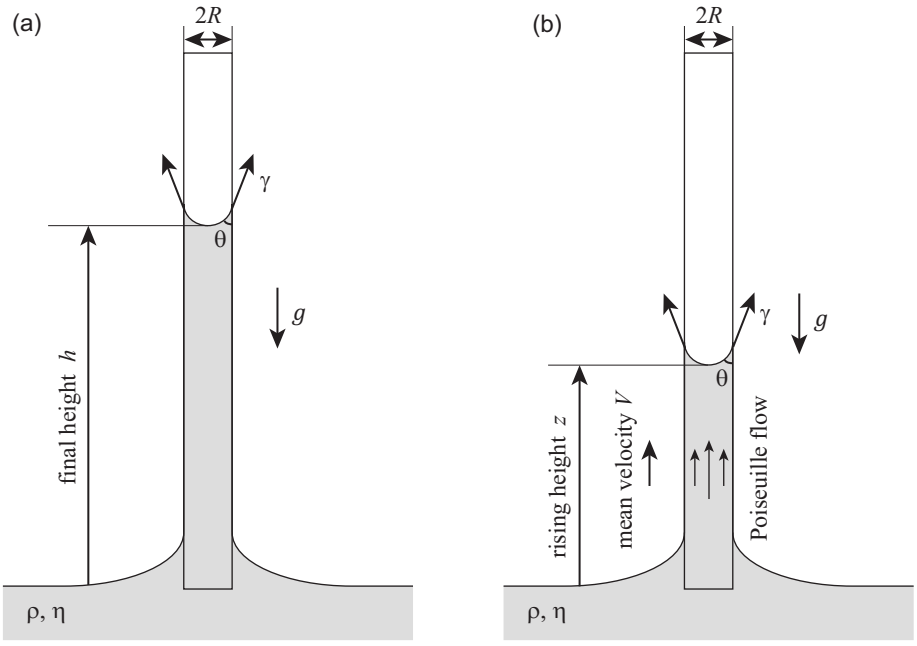

Fig. 4.1. Capillary rise. **(a)** The statical state and **(b)** dynamical state of capillary rise.

For the dynamics, we shall focus on the viscous regime here. In this regime, the effect of viscous friction is important compared with the effect of inertia and

gravity. Thus, the dynamics is determined by the competition of the capillary force F_γ working as the driving force and the viscous friction F_η. The former is $F_\gamma = 2\pi\gamma R\cos\theta$ as discussed above. The latter, the viscous friction is obtained as

$$F_\eta = 8\pi\eta V(t)z(t). \tag{4.5}$$

where $z(t)$ is the rising height, $V(t)$ is the mean velocity, and η is the viscosity of the liquid.

Because the inertia is negligible in this regime, the liquid moves uniformly with the mean velocity $V(t)$. Hence the rising height $z(t)$ increases with the mean velocity $V(t)$, *i.e.*, $V(t) = \mathrm{d}z(t)/\mathrm{d}t$. As a result, the rising height $z(t)$ is obtained as

$$z^2 = Dt, \tag{4.6}$$

where D is the imbibition coefficient (diffusion coefficient) defined by

$$D = \frac{\gamma R\cos\theta}{2\eta}. \tag{4.7}$$

This scaling law has been known as "Washburn's law" or "BCLW imbibition law" (details in chapter 1). In the case of complete wetting, namely when the contact angle θ is zero, D is written as $D = \gamma R/2\eta$.

4.2 Energy minimization

In this section, we discuss the statics and dynamics of the capillary rise by energy minimization.

To consider the final state of capillary rise, let the same assumption as in the previous section hold, namely the volume of the meniscus of the liquid inside the tube is negligible because the final height h is sufficiently larger than the capillary radius R. As the rising height increases from z to $z+\Delta z$ (from (a) State 1 to (b) State 2 in Fig.4.2), the energy of the liquid column increases by

$$\Delta E = \Delta E_\gamma + \Delta E_g. \tag{4.8}$$

Here, the first and the second terms on the right-hand side are differences of the

surface energy and the gravitational potential energy, namely,

$$\begin{aligned} \Delta E_\gamma &= (\gamma_{SL} - \gamma_S) 2\pi R \Delta z \\ &= -\gamma \cos\theta_E 2\pi R \Delta z \qquad (4.9) \\ \Delta E_g &= \int_z^{z+\Delta z} \rho g z' \pi R^2 \, \mathrm{d}z'. \qquad (4.10) \end{aligned}$$

Here, Young's law ($\gamma_{SL} + \gamma \cos\theta_E = \gamma_S$) was used in order to obtain the second equality of the ΔE_γ; R is the radius of the capillary tube, γ_{SL}, γ_S and γ are the surface energies of the solid-liquid, solid-air and liquid-air interfaces, respectively, and ρ is the density of the liquid. By integrating ΔE from $z = 0$ to $z = h'$, the total energy for the liquid column of height h' is obtained as

$$E(h') = -\gamma \cos\theta_E 2\pi R h' + \frac{1}{2} \rho g \pi R^2 h'^2. \qquad (4.11)$$

By minimizing this energy, the final height h is obtained as follows:

$$\left. \frac{\partial E}{\partial h'} \right|_{h'=h} = -2\pi R \gamma \cos\theta_E + \rho g \pi R^2 h = 0,$$

and hence,

$$h = \frac{2\gamma \cos\theta_E}{\rho g R}. \qquad (4.12)$$

In the case of complete wetting, the final height is written as

$$h = \frac{2\gamma}{\rho g R}. \qquad (4.13)$$

For the dynamics in the viscous regime, both the variation of kinetic energy and the gravitational potential energy are negligible because those are sufficiently smaller than the viscous dissipation. In this case, the total surface energy $\Delta\epsilon_\gamma$ due to the increase of the wetting area is lost as the viscous dissipation $\Delta\epsilon_\eta$. Thus, the sum of these energies is always zero, *i.e.*,

$$\Delta\epsilon_\gamma(z) + \Delta\epsilon_\eta(z) = 0,$$

or equivalently

$$-\gamma \cos\theta_E 2\pi R \; V(t) + k\eta \left(\frac{V(t)}{R} \right)^2 \pi R^2 \; z(t) = 0,$$

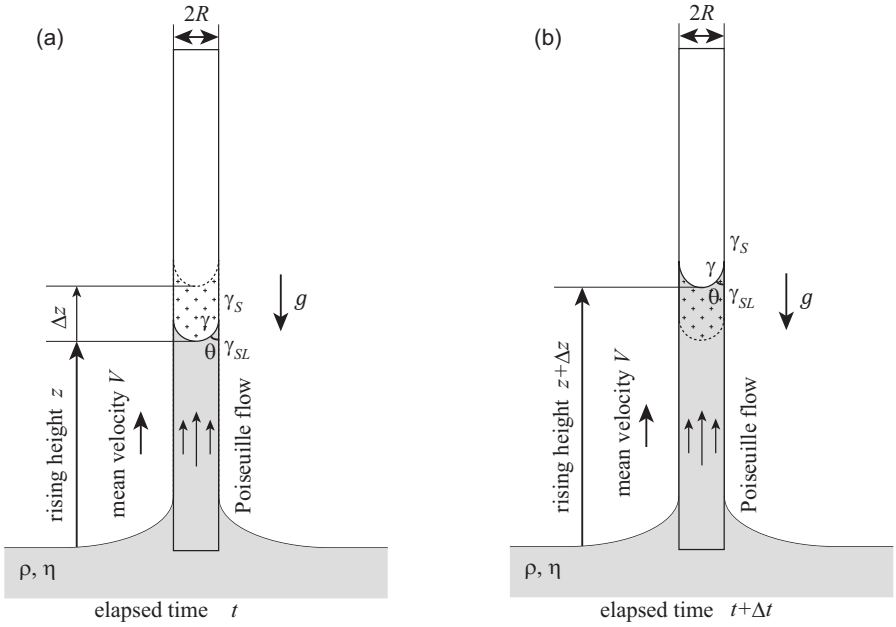

Fig. 4.2. Two states of the capillary rise. **(a)** State 1 (the rising height is z at the elapse time t) and **(b)** State 2 (the rising height is $z + \Delta z$ at the elapsed time $t + \Delta t$).

and hence,

$$V(t)\ z(t) = \frac{2\gamma \cos\theta_E R}{k\eta},$$

where η is the viscosity of the liquid, $z(t)$ is the rising height, $V(t)$ is the mean velocity, and k is a numerical constant whose order is unit. Here we assumed that entire liquid inside the capillary tube moves uniformly in the z-axis direction with the mean velocity $V(t)$. Thus, the rising height $z(t)$ increases with the mean velocity $V(t)$, *i.e.*, $V(t) = \mathrm{d}z(t)/\mathrm{d}t$. In this case, the rising height $z(t)$ is obtained as

$$z^2 = Dt \quad \text{where} \quad D \sim \frac{\gamma R \cos\theta_E}{\eta}. \tag{4.14}$$

In the case of complete wetting, the imbibition coefficient D is written as $D \sim \gamma R/\eta$.

4.3 Navier-Stokes equations

In this section, we shall investigate the statics and dynamics of the capillary rise with the incompressible Navier-Stokes equations with lubrication approximation, where the inertia term is ignored. If we take a cylindrical coordinate (r, ϕ, z) and write the flow velocity as $\boldsymbol{v}(t) = (0, 0, v(r, t))$, the incompressible Navier-Stokes equations with lubrication approximation are written as

$$0 = -\frac{\partial p}{\partial z} + \eta \left(\frac{\partial^2 v}{\partial r^2} + \frac{1}{r}\frac{\partial v}{\partial r} \right) - \rho g. \tag{4.15}$$

Here, p, η and ρ are the pressure, viscosity and density of the liquid, respectively. Since the pressure at the top of the liquid column is written as

$$p_{top} = p_0 + \Delta p, \tag{4.16}$$

where p_0 is the atmospheric pressure and Δp is Laplace pressure, namely the pressure jump across the liquid-air interface at the top of the elongating liquid column;

$$\Delta p = -\frac{2\gamma \cos\theta}{R}. \tag{4.17}$$

Here, θ is the contact angle between the liquid and the capillary tube at the top front and R is the radius of the capillary tube.

The statics of this phenomenon is described by taking $v = 0$ in eq.(4.15) and then integrating it with respect to z from $z = 0$ to $z = h$

$$\int_0^h \frac{\partial p}{\partial z}\, \mathrm{d}z = \int_0^h -\rho g \, \mathrm{d}z,$$

or equivalently,

$$p_{top} - p_0 = -\rho g h,$$

and hence,

$$\frac{2\gamma \cos\theta}{R} = \rho g h. \tag{4.18}$$

Consequently, the final height h is written as

$$h = \frac{2\gamma \cos\theta}{\rho g R}, \tag{4.19}$$

or

$$h = \frac{2\gamma}{\rho g R} \tag{4.20}$$

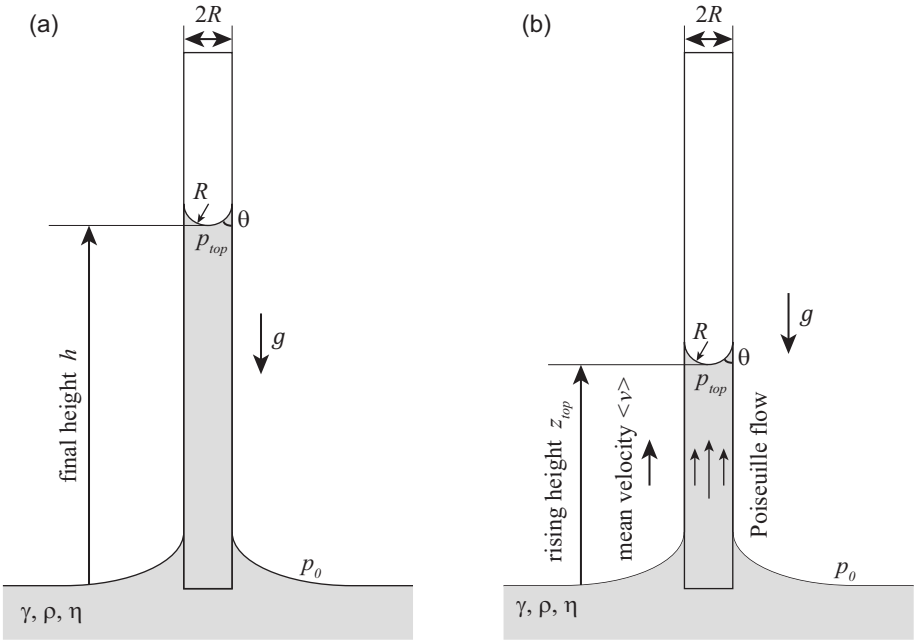

Fig. 4.3. Capillary rise. **(a)** The statical state and **(b)** dynamical state of the capillary rise

in the case of complete wetting.

In order to describe the dynamics in the viscous regime, we ignore the gravitational force because it is sufficiently small compared with the other terms in eq.(4.15). In this case, eq.(4.15) becomes

$$\frac{\partial^2 v}{\partial r^2} + \frac{1}{r}\frac{\partial v}{\partial r} = \frac{1}{\eta}\frac{\partial p}{\partial z} = -\frac{\alpha(t)}{\nu}, \tag{4.21}$$

which is similar to eq.(3.14) except the time dependence of p and v. Hence, we obtain solutions $v(r,\, t)$ and $p(z,\, t)$ from $u(r)$ and $p(z)$ in eq.(3.16). Furthermore, the relation between the pressure gradient $\alpha(t)$ and the mean velocity $\langle v(t)\rangle$ is obtained as

$$\alpha(t) = \frac{8\nu\langle v(t)\rangle}{R^2}, \tag{4.22}$$

which is similar to eq.(3.22). Thus,

$$-\left(p_{top}(t) - p_0(t)\right) = \frac{8\eta\langle v(t)\rangle}{R^2}\, z_{top}(t), \tag{4.23}$$

where $z_{top}(t)$ is the height of the front of the elongating liquid column, namely $z_{top}(t)$ is the same as the rising height in the two former sections (sec.4.1 and sec.4.2). Here, the liquid column elongates homogeneously because we ignored the inertia. Thus, the mean velocity $\langle v(t) \rangle$ is regarded as the elongating velocity of the liquid column, *i.e.*, $\langle v(t) \rangle = \mathrm{d}z_{top}/\mathrm{d}t$. Moreover, we can write the pressure at $z = z_{top}$ as $p_{top} = p_0 + \Delta p$ with $\Delta p = -2\gamma \cos\theta / R$ as mentioned above. As a result, we can obtain the following relation between the rising height z_{top} and the elapsed time t:

$$\frac{2\gamma \cos\theta}{R} = \frac{8\eta}{R^2} \frac{\mathrm{d}z_{top}}{\mathrm{d}t} z_{top}(t),$$

or

$$z_{top} \frac{\mathrm{d}z_{top}}{\mathrm{d}t} = \frac{\gamma R \cos\theta}{4\eta},$$

and thus,

$$z_{top}^2 = Dt \quad \text{with} \quad D = \frac{\gamma R \cos\theta}{2\eta}, \tag{4.24}$$

or

$$D = \frac{\gamma R}{2\eta} \tag{4.25}$$

in the case of complete wetting.

Chapter 5

Imbibition of Micro-Patterned Surfaces

By virtue of a recent technological development, the imbibition of micro-patterned surfaces has actively been studied. In this chapter, we overview previous studies, and note open problems and capabilities in this field. Then we shall detail two previous studies especially relating to the present works.

5.1 Overview of previous studies on imbibition of micro-patterned surfaces

A water drop put on a hydrophilic micro-patterned surface, on which an array of micro pillars is placed, penetrates between the micro pillars on the surface sometimes with a non-spreading macroscopic reservoir as seen in Fig.5.1 (isopropanol and ethanol are used instead of water in Fig.5.1). The dynamics of the above phenomenon in the viscous regime is described by Washburn's law or BCLW imbibition law; the imbibition length L scales with the square root of elapsed time t (details are in chapter 4). Thus, the macroscopic shape of the imbibition area is isotropic and homogeneous, while it changes a transient octagon and then a square in the final regime where the elongating length becomes comparable to the scales of the pattern (Fig.5.1). Here, the free liquid-air surface indicated by a blue arrow in Fig.5.1 becomes larger with spreading of the drop differently from the case of capillary rise in tubes, but the thickness of the imbibed liquid film remains comparable to the pillar height H.

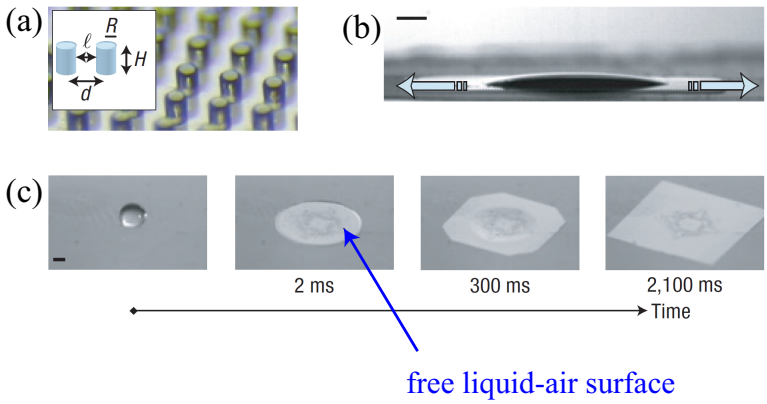

Fig. 5.1. Spreading of a drop put on a micro-patterned surface. **(a)** A schematic diagram and a photograph of a micro-patterned surface. Cylindrical pillars of the radius R and the height h are placed by the lattice distance d and the inter-post spacing l on the surface. **(b)** A side view of the spreading of an isopropanol droplet on a micro-patterned surface. The blue thick arrows indicate that the liquid penetrates to the textured surface with a non-spreading macroscopic reservoir. The parameters of the surface are $d = 100\mu$m, $R = 25\mu$m and $H = 30\mu$m, respectively. The scale bar is 1mm. **(c)** A series of pictures of the spreading of a millimeter radius liquid droplet after released on the surface ($t = 0$). The drop rapidly adopts an initial circular shape ($t \sim 2$ms), then adopts inhomogeneous shapes; a transient octagon (~ 300ms) and a final square shape ($\sim 2,100$ms). A blue arrow indicates the free liquid-air surface increasing with the spreading of the drop. These pictures were taken from obliquely at an angle of approximately 45°. The liquid is ethanol and parameters of the textured surface are $d = 100\mu$m, $R = 25\mu$m and $H = 60\mu$m. The scale bar is 1mm. Whole of the figures are reprinted from [14].

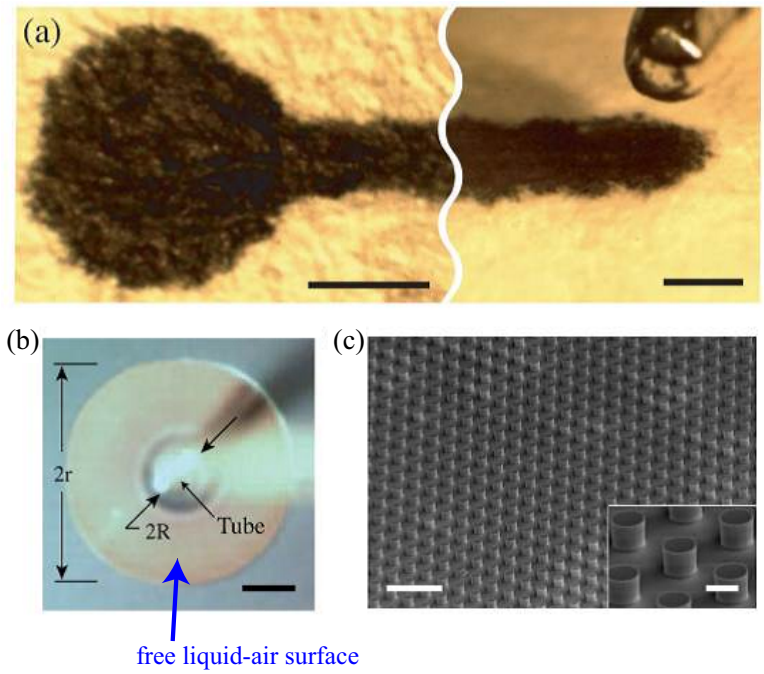

Fig. 5.2. Writing with ink on a paper and the system mimicking that. **(a)** Images of an ink tail on the paper: A blot generated by holding the pen at a fixed position for about 2 seconds (top view), and an end of the line drawn with the pen (tilted view). Here, a modern fountain pen and a rice paper are used. The scale bars indicate 1mm. **(b, c)** Blot formation on a super-hydrophilic surface which is an artificial surface mimicking a paper. (b) Top view of a liquid film emerging from a tube (which is out of focus) on a super-hydrophilic surface. The blue arrow indicates the free liquid-air surface increasing with the spreading of the drop. The scale bar is 1mm. (c) Scanning electron microscope (SEM) images of the artificial surface, on which an array of micro pillars is placed. The individual pillars are cylinders whose height h, diameter d, and arranged pitch s are 10-20μm, respectively. The scale bar in the main panel and the inset is 80μm and 15μm, respectively. Whole of the figures are reprinted from [33].

When one spills ink on a paper, it penetrates into the paper and a spot of the ink becomes bigger. Or, when one is thinking what he should write with a pen, the ink makes a spot on the paper. After he starts writing, the width of the line depends on how fast he moves the pen. Both of these typical geometries, *i.e.*, spots and lines, are results of the penetration of the ink into the paper. To understand details of this situation, Kim *et al.* modeled this situation as the system with a capillary (as a pen), a micro-patterned surface (as a paper) and liquid (as ink) (Fig.5.2) [33]. Authors of this article reported that the extension of the radius r of the spot is obeyed by a scaling law which is similar to BCLW imbibition law; $r \sim \sqrt{t}$ with the elapsed time t. Here, the area of the free liquid-air surface indicated by the blue arrow in Fig.5.2 becomes larger with spreading the liquid, however the thickness of the imbibed liquid film does not change; the thickness is comparable to the pillar height h.

When we make a hydrophilic micro-patterned surface perpendicularly touched with the horizontal surface of a liquid bath as shown in Fig.5.3(b), the liquid rises up between pillars. Further in this case, the dynamics of the imbibition in the viscous regime is described by an extension of that of the capillary rise in a tube; the rising height z scales with the square root of elapsed time t. In this case, the curvature of the elongating free liquid-air interface indicated by blue arrows in Fig.5.3 hardly changes with proceeding of imbibition (Fig.5.3(c)), although the surface is concaved by $d \sim b$ as shown in Fig.5.3(d) (Details are in sec.5.2).

In all of the three previous works reviewed above, the dynamics of the imbibition in the viscous regime is described by scaling laws which are similar to BCLW imbibition law; imbibition length z is proportional to the square root of elapsed time t. However, another scaling law, $z \sim t^{1/3}$, has also been found for imbibition dynamics of different type of textured surfaces.

The scaling law $z \sim t^{1/3}$ was reported by Obara and Okumura in 2012 [36]. They observed the capillary rise on textured surfaces on which an array of short and round submillimeter pillars is placed. Differently from the case of textured surfaces decorated with long and sharp-edged pillars as shown in Fig.5.3, the thickness of the imbibed liquid film decreases with rising height as shown in Fig.5.4(c,d). As a result, imbibition height z scales as $t^{1/3}$ (Details are in sec.5.3).

The scaling law $z \sim t^{1/3}$ has also been found for capillary rise into a sharp corner: a wedge formed by two vertical smooth plates (Fig.5.5(a,b)) [35], a corner obtained by two contacted cylindrical rods (Fig.5.5(c,d)) [34], and a corner

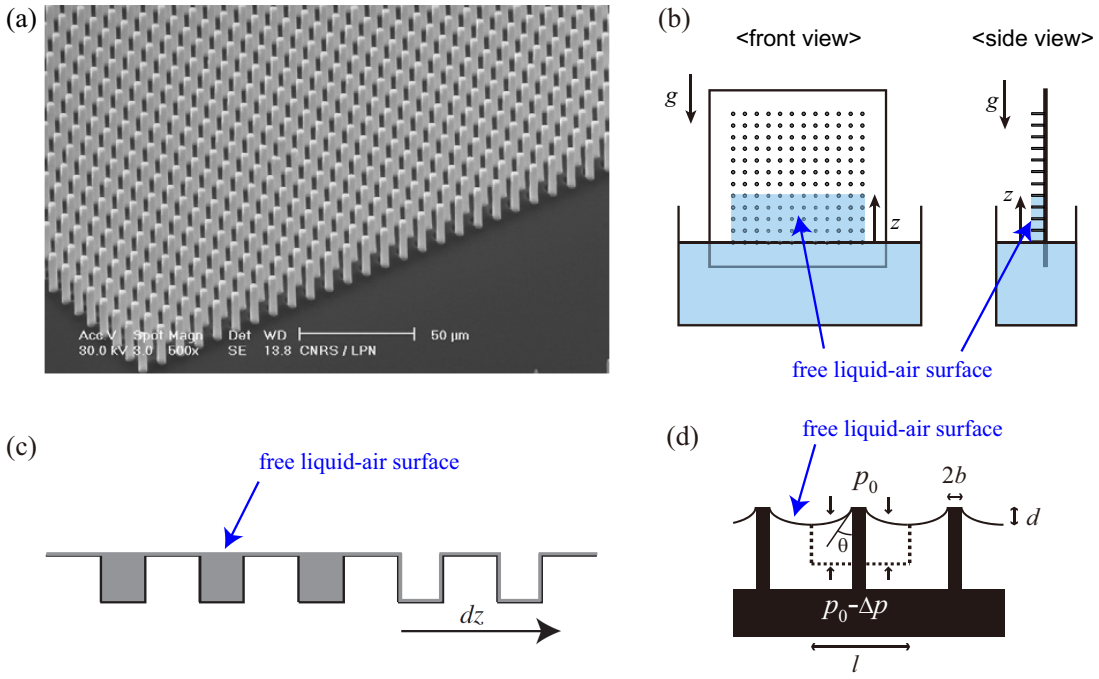

Fig. 5.3. Capillary rise on the micro-patterned surface. **(a)** A SEM image of a silicone surface decorated with an array of micro pillars whose radii, heights, and pitches are $b = 1.3\mu$m, $h = 26\mu$m and $p = 10\mu$m, respectively. The scale bar indicates 50μm. **(b)** A schematic image of the experiment. When an end of the micro-patterned surface is perpendicularly touched with the horizontal surface of a liquid bath, the liquid rises up between pillars. **(c, d)** Schematic images of the progression of the liquid into the forest of pillars. The thickness of the liquid film is comparable to the pillar height, although the surface is concaved for $d \sim b$ as shown in (d). The blue arrows in (b-d) indicate the free liquid-air surface. (a) and (c) are reprinted from [32], and (d) is reprinted from [46] (©2009 EPJ; with kind permission of EPJ).

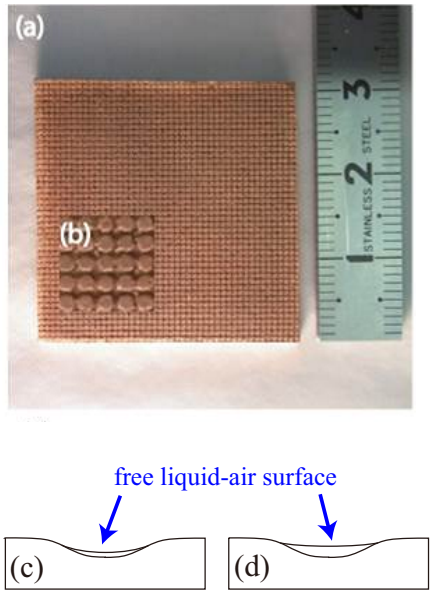

Fig. 5.4. **(a)** and **(b)** Overview and magnified view of a textured surface on which an array of short and round submillimeter pillars is placed. **(c, d)** Schematic images of the horizontal cross-section during imbibition. Imbibed liquid film is thinner at the top (c), and thicker at the bottom (d). The blue arrows in (c, d) indicate the free liquid-air surface. All of these figures are reprinted from [36].

obtained between flexible walls [49]. In these cases, the free liquid-air surfaces indicated by blue arrows form shapes like tongues as shown in Fig.5.5, *i.e.*, the area of the horizontal cross-section of the rising liquid decreases with the increasing of the height. This means that the smallest viscous scale identified as the wall distance along the liquid surface decreases with the height. As a result, the rising height z scales as $t^{1/3}$.

As discussed above with several previous works, the exponents appearing in the scaling laws of the imbibition dynamics seem to depend strongly on the shapes of the increasing free liquid-air surfaces (In the case of capillary rise in tubes, the liquid-air surface remains constant). However, the cross-over between these exponents has yet to be found. Furthermore, the fact that the imbibition dynamics generally slows down with time as ever seen might be a problem for a long-distance transportation or a viscous liquid transportation[1].

[1]Quite recently, non-slowing dynamics has been found for imbibition of textured surfaces

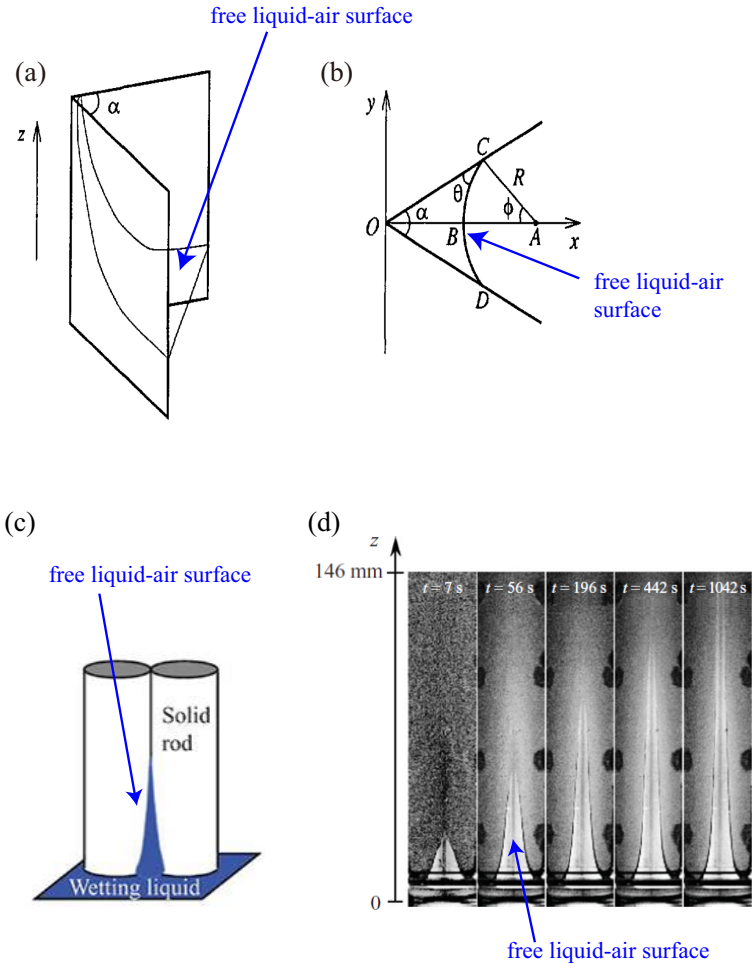

Fig. 5.5. **(a, b)** Capillary rise into a wedge. (a) A wedge of angle α formed by two vertical plates. Thin lines illustrate equilibrium capillary rise. (b) Horizontal cross-section of (a). Liquid is confined in the region OCBDO. **(c, d)** Capillary rise into a corner formed by two cylindrical rods. (c) A schematic image of the experiment. (d) A typical sequence obtained with Plexiglas rods of the diameter 30mm and a silicone oil V20 of the viscosity 20mPa s and the surface tension 20mN/m. The blue arrow in each figure indicates the free liquid-air surface. Figures (a, b) and (c, d) are reprinted from [35] and [34], respectively.

In the next two sections, we shall review details of the third work (by Ishino *et al.*) [32] and the forth work (by Obara *et al.*) [36], which are especially related to the present works.

5.2 Imbibition of micro-patterned surfaces with "long and sharp pillars"

Here, let us review a study by Ishino *et al.* [32]: imbibition of micro-patterned surfaces with "long and sharp pillars".

5.2.1 Experiment

An end of the sample is gently touched with the horizontal surface of a liquid bath as depicted in Fig.5.6.

The sample, a micro-patterned surface, is fabricated from silicone wafer by using techniques from microelectronics (photolithography and deep reactive ion etching). Because this technique allows one-directional selective etching of silicone wafer, we can obtain textured surfaces on which slender and sharp edged micro pillars are placed as shown in Fig.5.7. In addition, we can independently choose the values of the geometries, namely the radius b, height h and pitch p of the pillar. In this experiment, they fixed the pillar radius $b \sim 1\mu$m and the pitch $p \sim 10\mu$m, but changed the pillar height $h = 1 - 26\mu$m. Furthermore, with their surfaces, gravity is negligible during centimeter-sized imbibition experiment even if the sample whose size is order of centimeters is placed vertically.

As liquids, silicone oils with various viscosities η were used. Because silicone oil wets the sample well, the liquid rises up in the forest of micro pillars. They found that the rising height z scales with the square root of elapsed time t; $z^2 = Dt$ where D is the imbibition or penetration coefficient. The values of the coefficient D obtained from experiments with various pillar heights h and viscosities η are plotted in Fig.5.8.

on which long and sharp edged pillars are placed with linear gradient of pillar density [50].

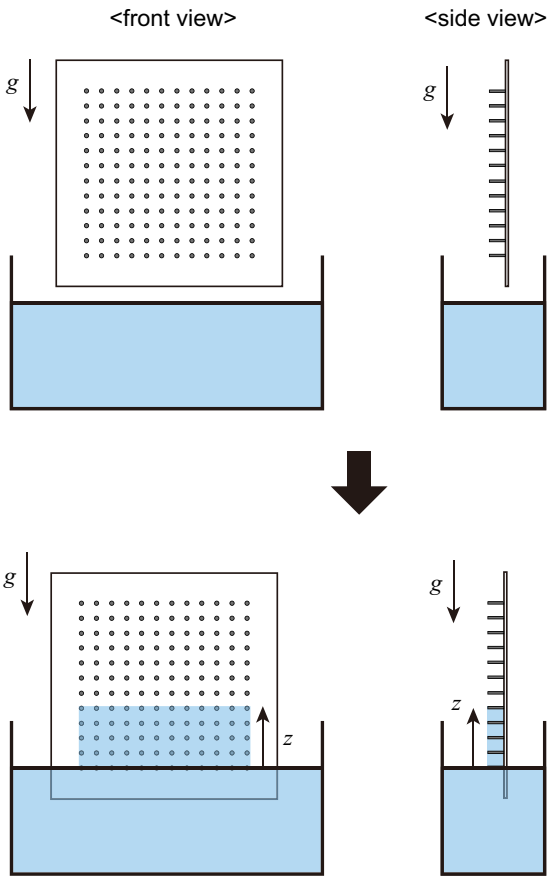

Fig. 5.6. Schematic images of the experimental setup. When an end of the sample is touched with the horizontal surface of a liquid bath, the liquid rises up in the forest of the pillars against gravity.

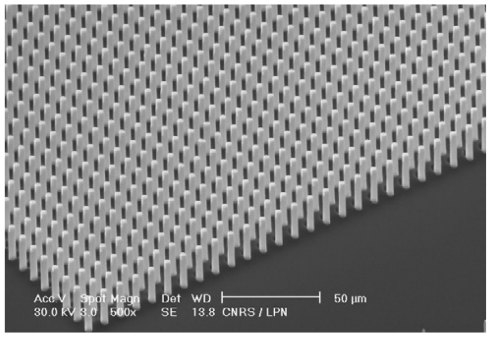

Fig. 5.7. A typical sample: a silicone surface decorated with an array of micro pillars whose radii, heights and pitches are $b = 1.3\mu$m, $h = 26\mu$m and $p = 10\mu$m, respectively. The bar indicates 50μm. This figure is reprinted from [32].

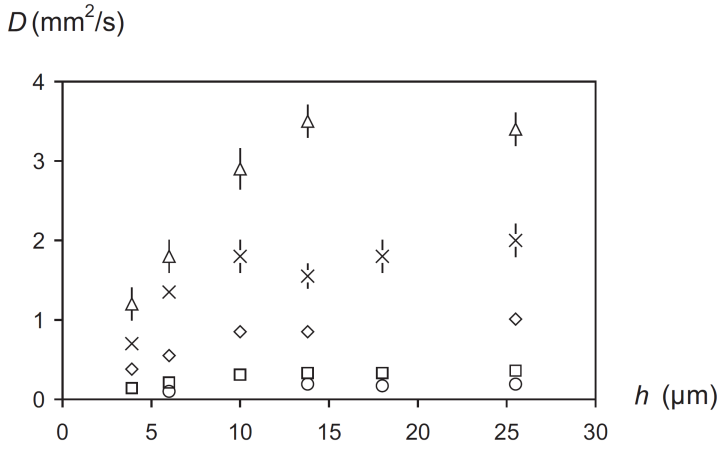

Fig. 5.8. Imbibition coefficient D is plotted as a function of the pillar height h for various viscosities of silicone oils (viscosities η are 4.6mPa s (triangles), 9.5mPa s (crosses), 19mPa s (diamonds), 48mPa s (squares) and 97mPa s (circles), respectively). D increases with the pillar height h before saturating at large heights. This figure is reprinted from [32].

5.2.2 Theory

The imbibition coefficient D is theoretically obtained in the following. Here, they assumed that the thickness of the liquid film is comparable to the pillar height h. This assumption is reasonable when the pillar radius b is sufficiently smaller than the pillar height h ($b \ll h$) as reported in [46]; the liquid is pinned at sharp edges of pillars so that the difference δ between the film thickness and the pillar height is estimated to be comparable to the pillar radius b, *i.e.*, $\delta \sim b$. In the case of $b \ll h$ so that $\delta \ll h$, we can assume a liquid film of the thickness h propagates during imbibition. With this assumption, the difference of the surface energy per unit width while the liquid film propagates by a distance dz is written as

$$dE = \{(\gamma_{SL} - \gamma_S)r + \gamma\}dz. \tag{5.1}$$

Here, γ_{SL}, γ_S and γ are the surface tensions of the solid-liquid, solid-air and liquid-air interfaces, respectively, and r is the roughness of textured surfaces, *i.e.*, the fraction of the actual surface area to the projected surface area; $r = 1 + 2\pi bh/p^2$. With Young's law ($\gamma \cos\theta_E + \gamma_{SL} = \gamma_S$) and the assumption that the equilibrium contact angle θ_E between the liquid and the substrate is zero, eq.(5.1) is written as $dE = (1-r)\gamma dz$. Since the roughness always satisfies $r > 1$, $dE < 0$ is obtained in the case of complete wetting. Thus, the driving force per unit length is written as

$$F_\gamma = -\frac{dE}{dz} = 2\pi\gamma\frac{bh}{p^2}. \tag{5.2}$$

Now we shall estimate the viscous friction. Differently from the case of capillary rise in a tube, two main origins are possible here. One is the friction between the liquid and the bottom solid surfaces. In this case, the viscous friction force per unit width is written as

$$F_1 \sim \eta\frac{V}{h}z, \tag{5.3}$$

where z is imbibition length and V is the mean flow velocity $V = \mathrm{d}z/\mathrm{d}t$. The other is the friction between the liquid and the lateral surfaces of pillars. In this case, the viscous friction per a pillar is written as $f \sim \eta(V/b)2\pi bh$. Thus, the viscous force per unit width is written as

$$F_2 \sim \frac{f}{p^2}z \sim \eta\frac{V}{b}\frac{bh}{p^2}z. \tag{5.4}$$

Although both frictions F_1 and F_2 should be present and oppose the motion, let us assume that one of them is negligible when $F_1/F_2 \sim p^2/h^2$ is sufficiently larger or smaller than 1. Hence, we can distinguish two different cases:

i) For short pillar ($h < p$), the dominant friction arises from the bottom solid surface, *i.e.*, the friction is written as F_1 (eq.(5.3)). From the competition of it and the driving force F_γ (eq.(5.2)), the rising height z is written as

$$z^2 = D_1 t, \tag{5.5}$$

where

$$D_1 = \frac{4\pi}{3}\frac{\gamma}{\eta}\frac{h^2 b}{p^2}. \tag{5.6}$$

ii) For long pillar ($h > p$), the dominant friction arises from the lateral surface of the pillars, *i.e.*, the friction is written as F_2 (eq.(5.4)). In this case, the rising height z is written as

$$z^2 = D_2 t, \tag{5.7}$$

where

$$D_2 = \frac{\gamma b}{\eta}(\ln(p/b) - 1.31). \tag{5.8}$$

Here, a numerical coefficient for the friction of a liquid progressing in a collection of cylindrical pillars was used [47].

In both regimes, the rising height z is proportional to the square root of elapsed time t; $z \sim t^{1/2}$.

5.2.3 Experiment and theory

Then, they compared experimental results with theories. The dynamical coefficients $D = z^2/t$ obtained from each experiment, are plotted as dimensionless quantities D/D_2 as a function of D_1/D_2 (Fig.5.9). Here, D_1 and D_2 are theoretical values calculated from the formulas discussed above (eq.(5.6) and eq.(5.8)) with parameters of textured surfaces. Fig.5.9 shows a good agreement between experimental results and theoretical prediction. First, all the data are collapsed onto a single curve. In short pillar region ($h < p$), namely $D_1/D_2 \sim h^2/p^2 \ll 1$, D/D_2 increases as D_1/D_2 increases until $D_1/D_2 = 1$, thus $D \sim D_1$, which is expected by theory. Then, in tall pillar region ($h > p$ namely $D_1/D_2 \gg 1$), D/D_2 saturates at a value around 1 as D_1/D_2 increases, namely $D \sim D_2$, which is also expected by theory.

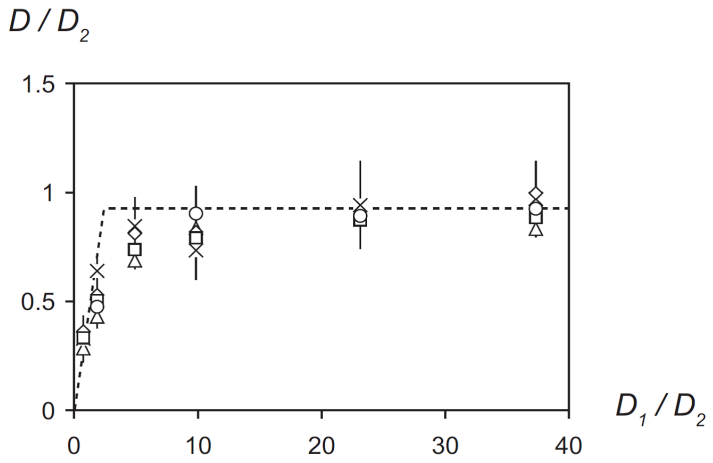

Fig. 5.9. Experimental dynamical coefficients D as a function of a dimensionless quantity. The different symbols are for different silicone oils (different viscosities) as indicated in Fig.5.8, and the dotted line expresses the theoretical prediction. This figure is reprinted from [32].

5.3 Imbibition of micro-patterned surfaces with "short and round pillar"

Here, we shall review a study by Obara *et al.* [36]: imbibition of micro-patterned surfaces with "short and round pillars".

5.3.1 Experiment

Similarly to the experiment performed by Ishino *et al.*, the sample is fixed perpendicularly to the horizontal surface of a liquid bath, then gently touched with the surface. In addition, they carried out experiments with the sample fixed with some tilt angle θ measured from the horizontal surface. Namely, the former case corresponds to the case of $\theta = 90°$. By tilting the sample, we can change an effective gravity G as

$$G = g \sin\theta, \tag{5.9}$$

where g is the gravitational acceleration, *i.e.*, g=9.8 m/s^2.

The samples are fabricated from copper substrates by a recently proposed

method reported in [48]. With this method, the surfaces on which an array of short pillars with round edges are placed are obtained as shown in Fig.5.10. The resulting surfaces are analyzed by using a microscope VHX-1000 (Keyence) and obtained an averaged profile as shown in Fig.5.10(d). As liquids, silicone oils with various viscosities η were used.

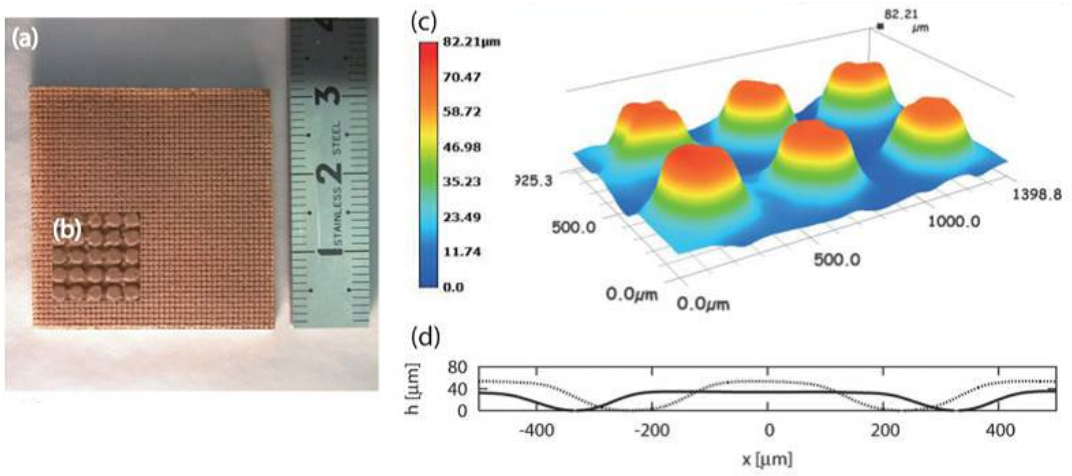

Fig. 5.10. **(a)** and **(b)** Overview and magnified view of a textured surface A. **(c)** Magnified overview of textured surface B. **(d)** Average section of the textured surface A (solid line) and B (dashed line). All figures are reprinted from [36].

5.3.2 Theory

The imbibition length x is theoretically described in the following: The incompressible Navier-Stokes equations with lubrication assumption are written as

$$0 = -\frac{\partial p}{\partial x} + \eta \nabla^2 v - \rho G. \tag{5.10}$$

Here, p is the pressure written as $p = p_0 - \gamma C$ with the atmospheric pressure p_0, the surface tension γ of the liquid, and the curvature C ($C > 0$) of the liquid-air interface. Thus, the scale of the first term of the right-hand side of eq.(5.10) is written as $\gamma C/x$ with the imbibition length x. v is the velocity of the flow.

Since viscosity and gravity are equally important in this experiment, the three terms in the right-hand side of eq.(5.10) are assumed to be of the same order. Thus, by comparing ρG and $\gamma C/x$, the local curvature at the imbibition front is estimated as

$$C \simeq \frac{\rho G x}{\gamma}. \tag{5.11}$$

Furthermore,

$$\rho G \simeq \eta \nabla^2 v \quad \text{or} \quad \frac{\gamma C}{x} \simeq \eta \nabla^2 v, \tag{5.12}$$

is also derived from comparing two of the three terms in eq.(5.10). With the mean velocity $V = \mathrm{d}x/\mathrm{d}t$, eq.(5.11) and another assumption that the Laplacian in eq.(5.12) scales as C^2, *i.e.*,

$$|\nabla^2| \simeq C^2, \tag{5.13}$$

both the first and the second equations of eq.(5.12) result in the same equation

$$x = \alpha t^{1/3}, \tag{5.14}$$

where

$$\alpha \simeq \left(\frac{\gamma^2}{\rho G \eta}\right)^{1/3}. \tag{5.15}$$

It is convinced that eq.(5.13) is a reasonable assumption in the following way. From eq.(5.11), it is easy to see the local curvature C of the imbibing front increases as the imbibition length x increases. In other words, the characteristic length, *i.e.*, the film thickness at the imbibing front, is estimated as C^{-1}, which scales as $1/x$. On the other hand, $|\nabla|^{-1}$ has a physical meaning of the thickness of the liquid film where Poiseuille flow develops. Thus, the film thickness at height x is written as $|\nabla|^{-1} \sim C^{-1} \propto 1/x$, which is different from the case of sec.5.2 where the thickness of the imbibed liquid film is comparable to the pillar height.

By introducing the capillary length $a = \sqrt{\gamma/(\rho G)}$, eq.(5.14) is renormalized as

$$\frac{x}{a} \simeq \left(\frac{t}{\tau}\right)^{1/3}, \tag{5.16}$$

where τ is the characteristic time scale defined as $\tau = \eta a/\gamma$, whose order is a few ms or less.

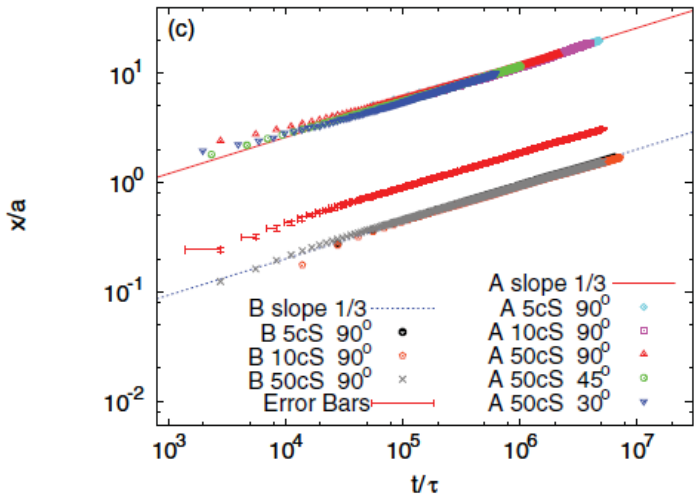

Fig. 5.11. Collapse of the data obtained from surfaces A and B (shifted downward by a factor of 10 to avoid overlap with the data from surface A) with yet another data set "B 10cS 90°" for demonstrating error bars (also shifted to avoid overlap). The errors in the vertical axis are always smaller than symbol size and those in the horizontal time axis are visible only at very early time ($t/\tau \leq 10^{-4}$). This figure is reprinted from [36].

5.3.3 Experiment and theory

They compared experimental results with theories in Fig.5.11, where eq.(5.16) is tested. As predicted by the model, all of the data from both surfaces A and B collapse well onto a line whose slope is one-third. Here, the collapsed data from surface B are shifted downward by a factor of 10 to avoid overlap with the data from surface A.

The good agreement between the experimental data and the theory supports the assumptions, *i.e.*, eq.(5.11) and eq.(5.13). In addition to this, the authors justified these assumptions by visualizing the film thickness although details are not described here.

The scaling law (eq.(5.14) with eq.(5.15), or eq.(5.16)) is independent of the pillar radius b, height h and pitch p. In other words, the imbibition dynamics is independent of the details of the geometry of the textured surfaces when pillars on the surface are short and round. Furthermore, the radius of curvature C^{-1} is determined by eq.(5.11) because this is the only natural local length scale available in the present case (the flim thickness is no longer comparable to pillar height).

Part III

Present Study

Chapter 6

Capillary Rise on the Surface of a Leg of a Small Animal and Artificial Surface Mimicking It

Recently, it has been known that some plants [1, 2], insects [3, 4] or animals [5, 6] have micro structures on their skin. Imbibition of those surfaces and of artificial surfaces mimicking them has actively been studied not only from biological interests but also from physical or fundamental interests. Furthermore, physical understanding of the dynamics of such phenomena probably gives us useful guiding principles for applications in various fields. Here, we shall describe imbibition of the surface of a leg of a small animal, wharf roach (*Ligia exotica*), and artificial surfaces partially mimicking it on the basis of the result in [6].

6.1 Capillary rise on the surface of a leg of a small animal

6.1.1 A small animal wharf roach

Wharf roach (*Ligia exotica*) is a small animal living by the sea (Fig.6.1). It has seven pairs of legs called "pereiopods". It is an ancient animal; its biological structure is quite old. In particular, it breathes through gills at its stomach. Thus, water is essential for it to survive. On the other hand, water can become a reason of its death because it can not swim for a long time. Namely, wharf

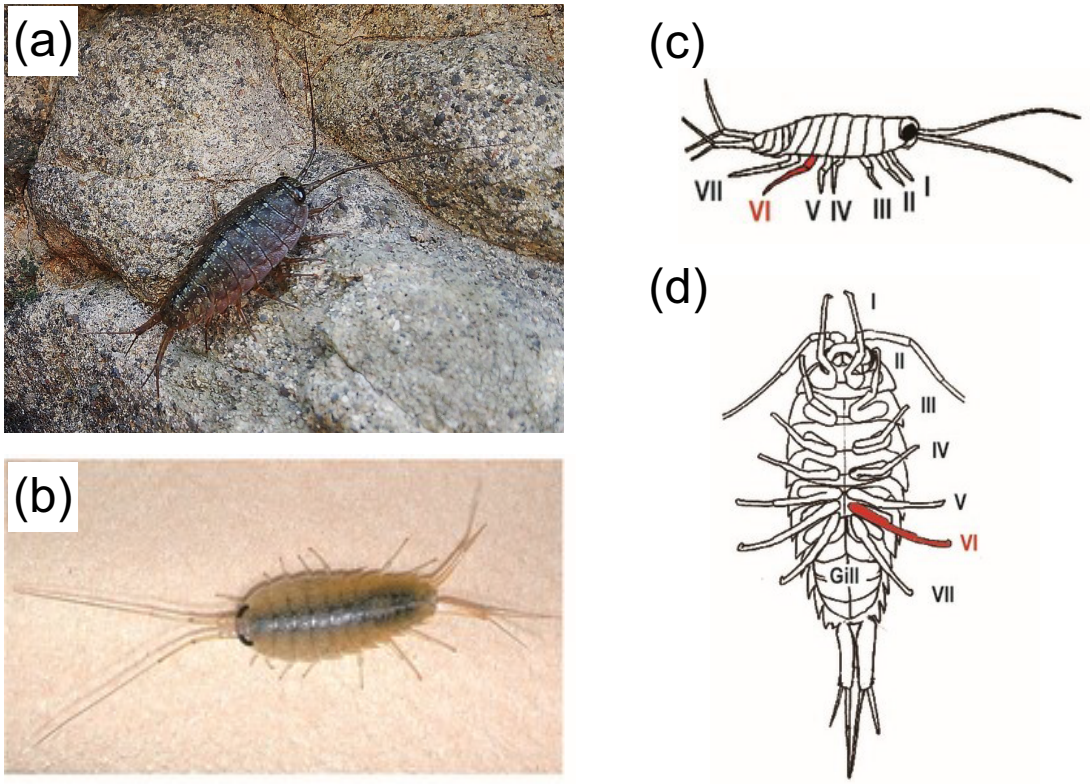

Fig. 6.1. A small animal wharf roach, *Ligia exotica*. **(a, b)** Pictures of wharf roach (a) taken by M.T. at Enoshima, JAPAN and (b) used in the study [52]. **(c, d)** Illustrations of wharf roach: (c) side and (d) ventral views. (b-d) are reprinted from [52].

roach needs appropriate amount of water to survive. To achieve this, it uses its VIth and VIIth legs. When it brings these two legs together, and put the tip of the unit in a water pool, water rises up between these legs. This phenomenon is similar to what we can see during eating noodles with chopsticks; if one brings his chopsticks together and put their tip in the soup, the soup rises up between chopsticks, although capillary rise between the legs seems to have an advantage for water transport compared with that between chopsticks because the outer surfaces of the legs have special paths for water transportation differently from rather smooth surfaces of chopsticks.

The outer surfaces of the VIth and the VIIth legs are the followings (also see Fig.6.2): both the VIth and the VIIth legs have an unguis and six podites. There are hollow structures called "gutter" (indicated by the black arrow in Fig.6.2(D)) on the 1st and the 2nd podites of the VIth leg and the 1st and 80% of the 2nd podites of the VIIth leg. There is a path connecting the 1st podite (including the region with gutter) to the 5th podite on the outer surface of the VIth leg, while there is no gutter on the 3rd, 4th, and 5th podites. The path is covered with many micro structures (cuticular protrusions). In particular, regular arrays of micro protrusions are observed from the proximal half of the 2nd podite to the proximal end of the 5th podite of the VIth leg, as indicated by white arrows in Fig.6.2. On the VIIth leg, however, the regular array of micro protrusions is only observed on the 6th podite (indicated by the white arrow in Fig.6.2(C)). There are small areas covered with thin and relatively long cuticular protrusions at the distal ends of the 3rd, 4th and 5th podites of the VIIth leg (indicated by white arrowheads in Fig.6.2).

Detailed observations of the protrusions on the surface of the VIth leg are shown in Fig.6.3. The surface is covered with two types of protrusions: hair-like protrusion (HLP) and paddle-like protrusion (PLP). The gutter on the 2nd podite and the path area on the surface of the 3rd podite are covered entirely with hair-like protrusions (HLPs). On the other hand, on the 4th and the 5th podites, the central region of the path is covered with paddle-like protrusions (PLPs), while the edge region of the path and the joints of the legs are covered with hair-like protrusions (HLPs). Here, the HLPs and PLPs on the 4th podite of the VIth leg (Fig.6.3(b-d)) seems to be two types of blades whose geometries are the same while the sizes are different. Thus, let us use "narrow blades" instead of hair-like protrusions (HLPs) and "wide blades" instead of paddle-like

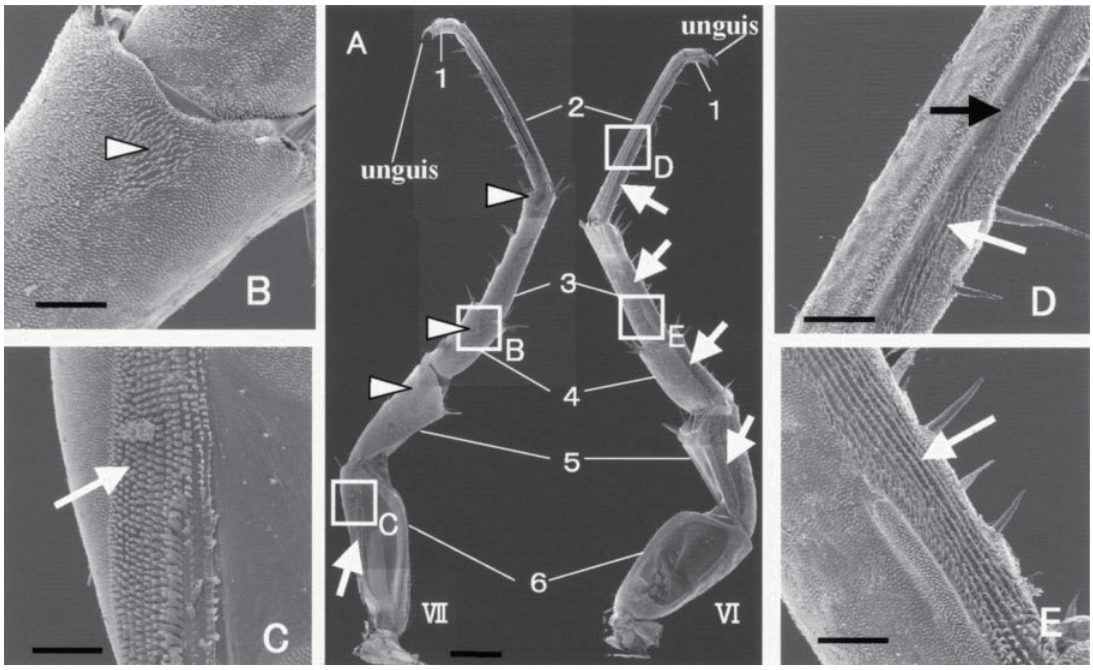

Fig. 6.2. Scanning electron microscope (SEM) images of the VIth and VIIth legs. White arrows indicate regular lines of protrusions, and white arrowheads indicate long protrusions of the VIIth leg. **(A)** the VIth and VIIth legs. White Arabic numbers indicate the numbers of podites of each leg. There are hollow structures called "gutter" on the 1st and 2nd podites of the VIth leg and the 1st and 80% of the 2nd podites of the VIIth leg. These gutters are located at the center of each leg, oriented longitudinally along the podites. The gutter on the 2nd podite of the VIth leg continues to the area covered with micro structures on the 3rd, 4th and 5th podites. It makes a path for water transport from the 1st to the 5th podites. On the VIIth leg, only the 6th podite has micro structures on the surface. Rectangles B-E indicate positions of higher magnifications in (B-E). The scale bar is 1.5mm. **(B)** The 4th podite and **(C)** 6th podite of the VIIth leg. **(D)** The 2nd podite of the VIth leg. A black arrow indicates the gutter, which is covered with micro protrusions. **(E)** The 3rd podite of the VIth leg. Scale bars in (B-E) are $300\mu m$. All figures are reprinted from Horiguchi *et al.* 2007. *Biol. Bull.* **213**: 196-203 [51] with permission from the Marine Biological Laboratory, Woods Hole, MA.

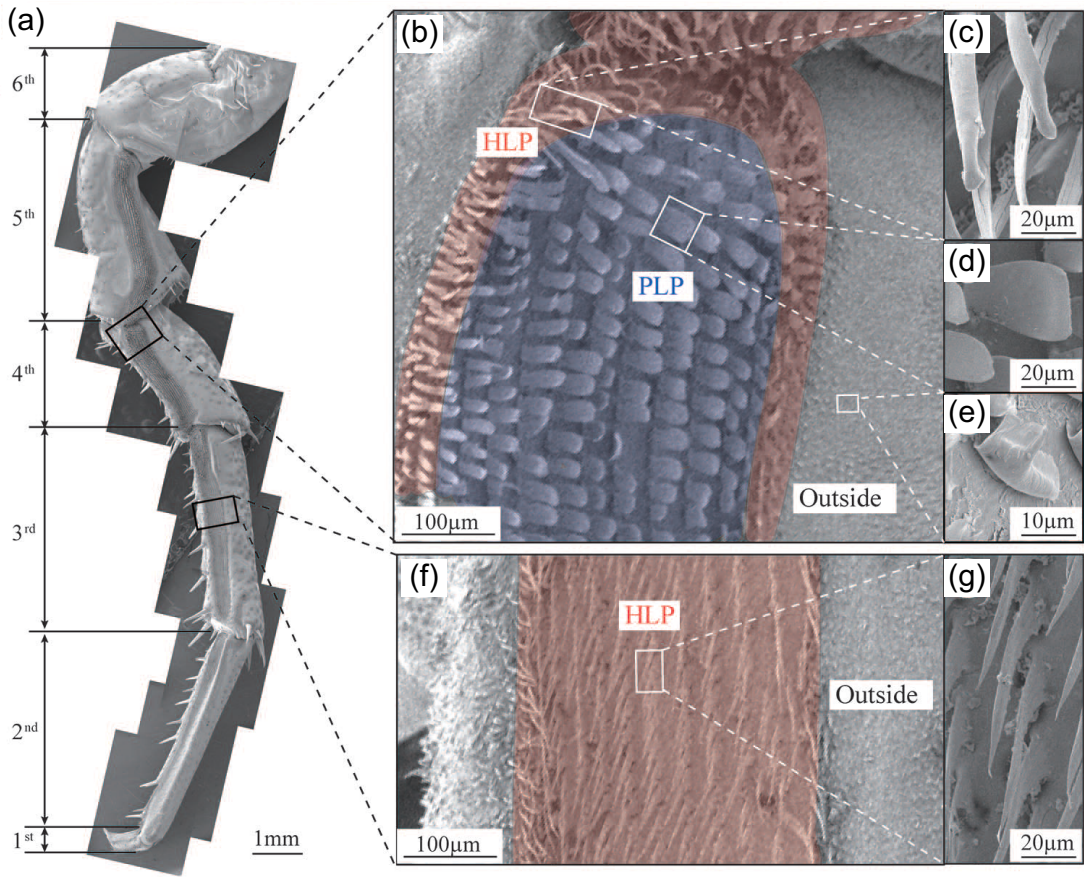

Fig. 6.3. Scanning electron microscope (SEM) images of the VIth leg. **(a)** Combined SEM image of the entire VIth leg comprising six podites. A path on the outer surface from the 1st to the 5th podites is clearly observed. **(b)** The surface near the proximal end of the 4th podite. Two different protrusions are observed: Hair-like protrusions (HLPs, or narrow blades) placed at the edge region of the path and the joints, and paddle-like protrusions (PLPs, or wide blades) placed at the central region of the path. The outside of the path is covered with small curved plates. **(c-e)** Magnified SEM images of (c) the hair-like protrusions (HLPs, or narrow blades), (d) the paddle-like protrusions (PLPs, or wide balades), and (e) small curved plates placed at the outside of the path. **(f)** The surface of the 3rd podite. The entire area of the surface of the path is covered with HLPs. The outside of the path is covered with small curved plates similarly to the 4th podite. **(g)** The magnified SEM image of HLPs. All figures are reprinted from [52].

protrusions (PLPs); narrow blades cover the edge region of the 4th and the 5th podites and the joints, and wide blades cover the central region of the 4th and the 5th podites.

To test the roles of these micro structures, imbibition experiments were carried out for isolated VIth and VIIth legs in [51] (also see Fig.6.4). When the middle part of the 2nd podite of the VIth leg is dipped into the colored water, we can see that the water rises up along the path against gravity, then stops rising at the joint between the 2nd and the 3rd podites (Fig.6.4(B)). When the entire 2nd podite is dipped into the water, *i.e.*, the distal end of the 3rd podite is touched with the surface of the water, the water rises up through the 3rd, 4th and 5th podites, then stops rising at the joint between the 5th and the 6th podites (Fig.6.4(C)). Even if the distal end of the 6th podite is dipped into the water, the water does not rise up to the 6th podite (Fig.6.4(E)). Concerning the VIIth leg, water rises up only when the distal end of the 6th podite is touched with the surface of the water, and stops rising at the proximal end of the podite (Fig.6.4(F-J)). Therefore it is noteworthy that the capillary rise is a result of not activities of wharf roach but the isolated legs themselves. These capillary rises are rather natural phenomena caused by their surfaces with micro structures similarly to the capillary rise on textured surfaces (cf. Part II Previous Study), and the capillary rise with its legs helps wharf roach to transport water from water pools to its gills.

6.1.2 Dynamics of capillary rise on the surface of a leg of wharf roach

Here, we shall discuss the dynamics of capillary rise on the surface of a leg of wharf roach. As indicated above, wharf roach has a characteristic path with micro structures on the surface of the VIth leg. While it uses both the VIth and the VIIth legs to transport water, here only the isolated VIth leg is used for imbibition experiment as shown in Fig.6.4. Here, let us focus on capillary rise from the 3rd to the 5th podites of the VIth leg, which is observed when the distal end of the 3rd podite is touched with the water surface (Fig.6.4(C)).

When the distal end of the 3rd podite of the VIth leg is touched with the horizontal surface of the colored water bath, the water rises up as shown in Fig.6.5. Here, water is colored red in order to see easily. Differently from capillary rise on textured surfaces, the front of the rising liquid is not a horizontal line.

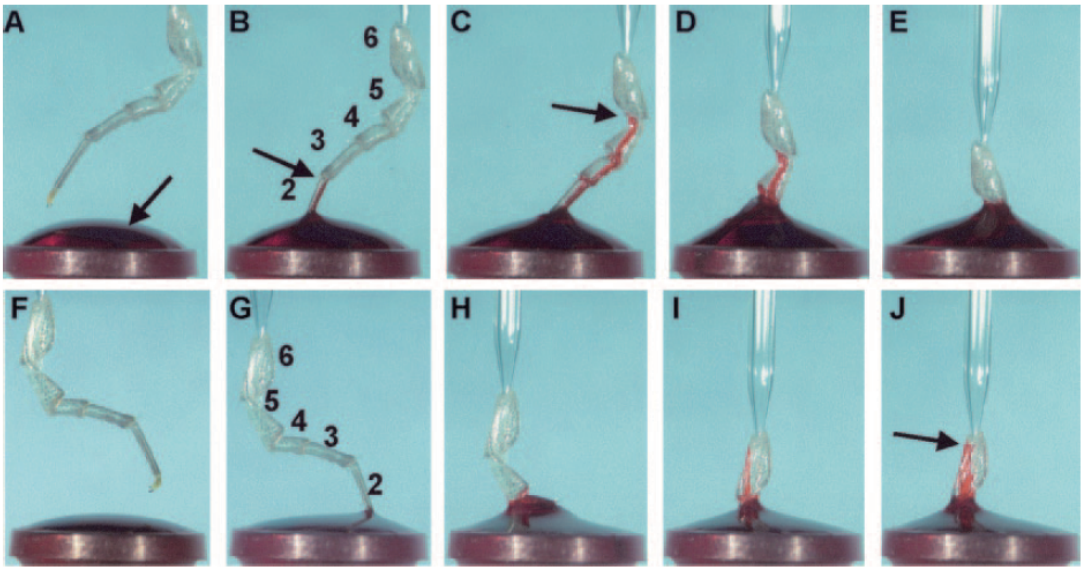

Fig. 6.4. Illustrations of colored water flow along the caudal side of the VIth leg (A-E) and the frontal side of the VIIth leg (F-J). **(A)** The VIth leg before touched with the water surface. A black arrow indicates the meniscus of red-colored water at the top of a tube. **(B)** When the middle of the 2nd podite is dipped into the water, the water rises until the proximal end of the podite. A black arrow indicates the place where water stops rising up. **(C)** When the entire of the 2nd podite is dipped into the water, *i.e.*, the distal end of the 3rd podite is touched with the surface of water, water rises up through the 3rd, 4th and 5th podites, then stops rising at the joint between the 5th and the 6th podites. A black arrow indicates the place where water stops rising. **(D, E)** Even if the distal end of the 6th podite is dipped into the water, the water does not rise up to the 6th podite. **(F-J)** Similar imbibition experiment with the VIIth legs. The water rises up only when the distal end of the 6th podite is touched with the surface of the water, and stops rising at the proximal end of the podite (I, J). A black arrow indicates the place where water stops rising. All figures are reprinted from Horiguchi *et al.* 2007. *Biol. Bull.* **213**: 196-203 [51] with permission from the Marine Biological Laboratory, Woods Hole, MA.

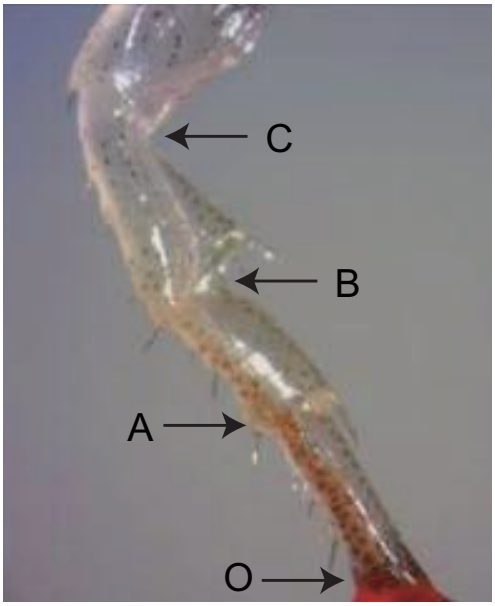

Fig. 6.5. A picture of the capillary rise on the surface of the VIth leg. When the distal end of the 3rd podite (the lowest podite in the picture) is touched with the surface of the colored water bath, the water rises up on the surface of the 3rd, 4th and 5th podites of the leg. O, A, B and C indicate the positions of joints between the 2nd and 3rd, 3rd and 4th, 4th and 5th, and 5th and 6th podites, respectively. This figure is reprinted from [6].

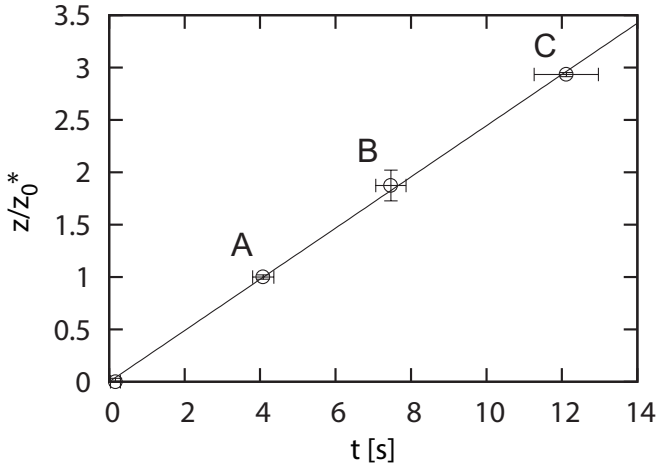

Fig. 6.6. Normalized rising height plotted as a function of the elapsed time with a macroscopic view; the heights of the joints and times when water arrives at each joint are plotted. O(origin), A, B and C correspond to those in Fig.6.5. Non-slowing down dynamics is found on this macroscopic scale; rising height scales with the elapsed time on this scale. This figure is reprinted from [6].

Sometimes liquid flows with branching; some flows upward and some downward. This is caused by inhomogeneity of the natural textured surface differently from artificial ones. As a result, tracking the propagating front on a microscopic scale is difficult. On the other hand, on a macroscopic scale, we can discuss the motion of liquid rising; on a coarse-grained level, the front seems to start proceeding to the next podite only after the lower podite is almost completely filled. Even if the filling dynamics within a podite is complex, the moment when the bulk water front arrives at each joint (to proceed to the next podite) and the height of the joint can be defined well. This result is illustrated in Fig.6.6, where the height z of each joint renormalized by the length z_0^* of the lowest podite in Fig.6.5 (the 3rd podite) are plotted as a function of the time t when water front arrives at each joint. As shown in this figure, the imbibition height z is proportional to the elapsed time t, namely $z \sim t$, on this macroscopic scale. This non-slowing down dynamics of imbibition is quite unusual, because imbibition dynamics is generally slowing down such as $z \sim \sqrt{t}$ or $z \sim t^{1/3}$.

6.2 Capillary rise on artificial surfaces

6.2.1 Artifical surfaces mimicking the surface of the leg of a wharf roach

Motivated by the unusual feature of the capillary rise on the surface of the leg discussed above, we fabricated the textured surfaces mimicking the texture on the leg (Fig.6.7) with which we carried out imbibition experiments. To fabricate the artificial textured surfaces, silicone wafers and the photolithographic and ion etching techniques are used similarly to those in the previous study described in sec.5.2. The hybrid texture "HT" (the central path in Fig.6.7) is the textured surface mimicking the surface of the 4th and the 5th podites of the VIth leg; wide blades are placed at the central region of the hybrid texture (the blue region in the HT in Fig.6.7. We call this region "CHT") and narrow blades are placed at the edge region and joints of the hybrid texture (the red region in the HT in Fig.6.7. We call this region "EHT"), which is surrounding the central region CHT. For reference, we also fabricated the central texture "CT" (the right blue path in Fig.6.7) where only wide blades are placed, and the edge texture "ET" (the left red path in Fig.6.7) where only narrow blades are placed. Both of the central and edge texture (CT and ET) are specified by the set of length (l_c, W_c, L_c) and (l_e, W_e, L_e) of micron scales, respectively (see Fig.6.7). Here, subscripts "c" and "e" indicate "central" and "edge", respectively. l and L are blade length and blade pitch in longitudinal direction of paths, and w and W are those in lateral direction of paths, while w is constant ($w_c = w_e = w$) in our experiments. The blade height h is also constant in all of our experiments.

While faithful mimicking of the real leg is technically difficult, we decided typical values sets of (l_c, W_c, L_c), (l_e, W_e, L_e) and (w, h) from pictures of the leg (Fig.6.3) as follows: (l_c, W_c, L_c) = (20, 52, 40), (l_e, W_e, L_e) = (10, 27, 20) and (w, h) = (2, 30) in the unit μm. We regarded the substrate with this parameter set as a reference substrate, then other substrates with different parameters were also fabricated. Here, we note that our reference patterned surface is different from the surface of the real leg in the following points: First, the blade width w and height h of the real one seems to be less than 1 μm and about 50 μm, respectively, while we decided (w, h) = (2, 30) μm for all surfaces, because of fabricating limit from technical difficulties. Second, real blades may be bendable with capillary force, and some may be placed on the base with some tilt angles.

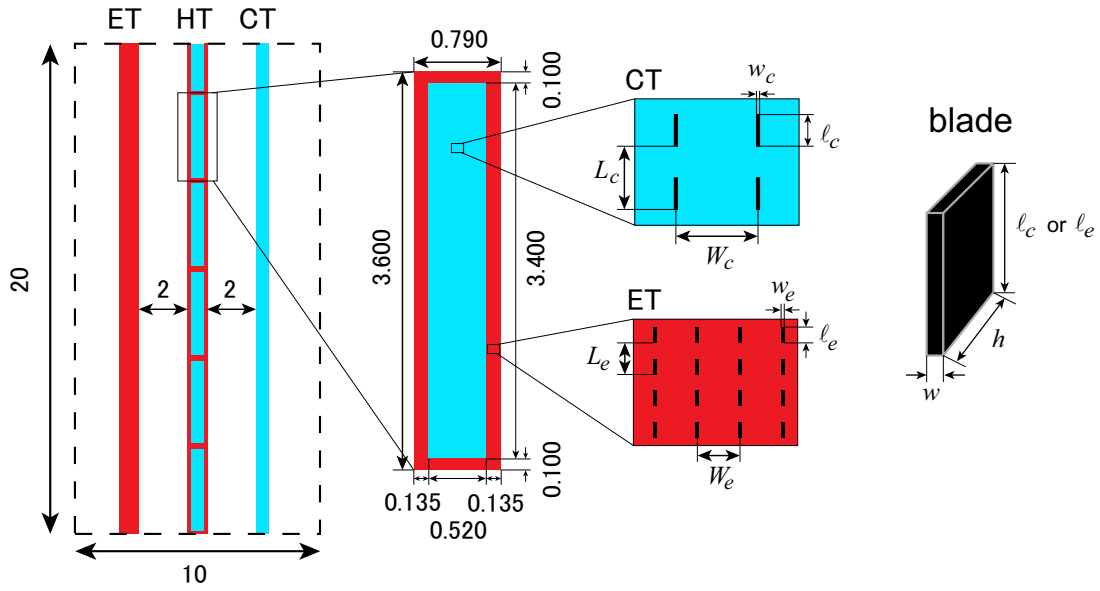

Fig. 6.7. Illustration of the artificial surfaces. The "Hybrid Texture (HT)", which is the surface mimicking the surface of the 4th and the 5th podites of the VIth leg of wharf roach, consists of two types of blades: wide blades placed at the central regions of the path (we call this "Central region of the Hybrid Texture (CHT)"), and narrow blades placed at the edge regions and joints of the path (we call this "Edge region of the Hybrid Texture (EHT)"). The length of "podite" is designed to be $z_0 = 3.6$mm (or 3.4mm), which is comparable to the typical length of a podite in the real leg. For reference, we also fabricate "Central Texture (CT)" which consists of only wide blades and "Edge Texture (ET)" which consists of only narrow blades. The values in the figure are lengths of each part whose unit are mm.

Finally, the real structure is not so regular as the structure of the imitation, and irregularity of patterns probably causes complex imbibing dynamics on the microscopic scale as seen in the capillary rise on the surface of the real leg (see sec.6.1.2).

6.2.2 Experiment

We carried out imbibition experiments with artificial textured surfaces. A snapshot of the imbibition of the reference substrate is shown in Fig.6.8(a). As seen in it, the imbibition fronts on the artificial surfaces are practically horizontal lines because of the regularity of the patterns as discussed above, which is different from the case of the imbibition of the surface on the real leg.

In addition, we could not reproduce "waiting motion" at each joint, namely the imbibed liquid fronts of the edge and central regions of the HT path seem to proceed independently through "joints" instead of to stop at joints until the liquid fills the lower podites as seen in capillary rise on the surface of the real leg. As a result, the front of each path can be tracked from series of snapshots such as Fig.6.8(a). Thus, we can plot rising height z normalized by the length of the podite z_0 or the square of that, *i.e.*, $(z/z_0)^2$, as a function of the elapsed time t (Fig.6.8(b) or (c)). The symbols in the plots are as follows: the imbibition front on the edge texture "ET" (α : $\square$) and the central texture "CT" (β : $\circ$), and in the edge and central regions of the hybrid texture "EHT" (γ : $\blacksquare$) and "CHT" (δ : $\bullet$) as indicated by horizontal arrows in Fig.6.8(a).

The imbibition of the HT path of the reference substrate in Fig.6.8 shows some remarkable features: imbibition of the edge and central regions of the HT path (EHT and CHT) are both faster than the original non-hybrid counterparts of ET and CT, respectively. These are also indicated by vertical solid arrows (for CT or CHT) and dashed ones (for ET or EHT) in Fig.6.8(a), whose lengths reflect relative magnitude of imbibing velocity. (1) Imbibition on the ET path (α : $\square$) is faster than that on the CT path (β : $\circ$) because a typical size of blades of ET path is smaller than that of CT path; capillary force driving imbibition is larger for textures with smaller blades (difference of viscous friction is less dominant than that of driving force although viscous friction is also larger for textures with smaller scale). This feature is also recognized in EHT and CHT paths, namely imbibition of the edge region of the HT path (γ : $\blacksquare$) is faster than that of the central region of the HT path (δ : $\bullet$). (2) The propagating front on

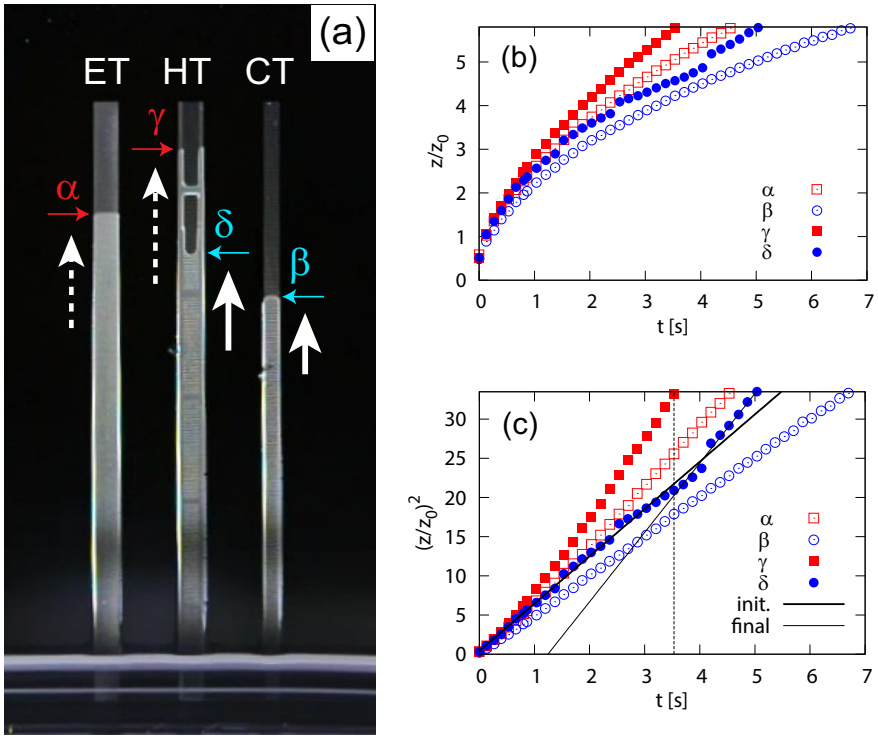

Fig. 6.8. Capillary rise on the reference substrate of artificial surfaces; the values of the parameters are $(l_c,\, W_c,\, L_c) = (20,\, 52,\, 40)$, $(l_e,\, W_e,\, L_e) = (10,\, 27,\, 20)$ and $(w,\, h) = (2,\, 30)$ in the unit μm. **(a)** A snapshot of capillary rise. The imbibition fronts are indicated by the horizontal arrows with symbols: the imbibition front on the edge texture "ET" (α), and the central texture "CT" (β), and in the edge and central region of the hybrid texture "EHT" (γ) and "CHT" (δ), respectively. The vertical arrows indicate relative magnitudes of imbibing velocities. **(b)** The rising height z normalized by the podite length z_0 as a function of the elapsed time t obtained from the capillary rise on the reference substrate. In order to clarify the dynamics in the unit of z_0, the origin is shifted by a small amount corresponding to an initial dip length to start the imbibition (similarly for (c)). The labels, $\alpha - \delta$, correspond to the labels in (a) (similarly for (c)). **(c)** The square of the normalized rising height $(z/z_0)^2$ as a function of t, obtained from the reference substrate. The solid and thin lines with labels "init." and "final" are obtained by fitting the data in the initial and final regimes of the imbibition of the central region of the HT path (δ). The vertical dashed line is the line separating both regimes.

the edge region of the HT (EHT) path (γ : ■) is even faster than that on the ET path (α : □), although the values of parameters (l, W, L, w, h) are the same for both. The reason of this is that the moving water front in the CHT path works as a liquid bath for imbibition of the EHT path. (3)The front on the central region of the HT (CHT) path (δ : •) is also faster than that on the CT path (β : ○), although the values of parameters are the same for both again. The reason is that the preceding water in the EHT path gives an extra pull for the front in the CHT path.

Figs.6.8(b) and (c) suggest that the imbibition length scales as $z \sim t^{1/2}$ at least for the ET and CT paths (α : □ and β : ○). Though rather technical, here, the origin is shifted by a small amount which corresponds to the initial dip length to cause the imbibition in order to clarify the dynamics in the unit z_0. This shift is much smaller than the overall imbibition lengths and does not affect practically the linear relation between z^2 and t.

In Fig.6.8(c), another interesting feature of the imbibition of the artificial hybrid textured surface is seen; the imbibition of the central region of the HT path (δ : •) is divided in two dynamic regimes: the initial and final regimes, which are separated by the vertical dashed line. The initial dynamics proceeds roughly as $t^{1/2}$, which is indicated by the solid line in Fig.6.8(c), and is slightly faster than the dynamics on the CT path (β : ○) although that is intermittent at "joints". The final regime starts when the front of the edge region of the HT path (γ : ■) reaches the top of the path, as indicated by the vertical dashed line. The final dynamics, which is indicated by the thin line, also proceeds roughly as $t^{1/2}$ and is faster than the initial one.

Several dynamic features observed in Fig.6.8(a-c) on the reference substrate qualitatively remain the same as those on other substrates with different parameter values: (l_c, W_c, L_c) = (10, 52, 30) and (l_c, W_c, L_c) = (20, 52, 60) in Figs.6.9 (a) and (b), respectively. Here, (l_e, W_e, L_e) = (10, 27, 20) and (w, h) = (2, 30) remain the same as those on the reference substrate. In particular, the imbibition dynamics in the central region of the HT paths is always divided in two regimes, and both the initial and final dynamics scale roughly as $t^{1/2}$. Then, the initial intermittent dynamics is slightly faster than that on the CT path, and the final dynamics, which starts when the edge front reaches the top, is faster than the initial one. These suggest the following: the initial imbibition dynamics on the CHT path may be described by the same theory as that developed for simpler

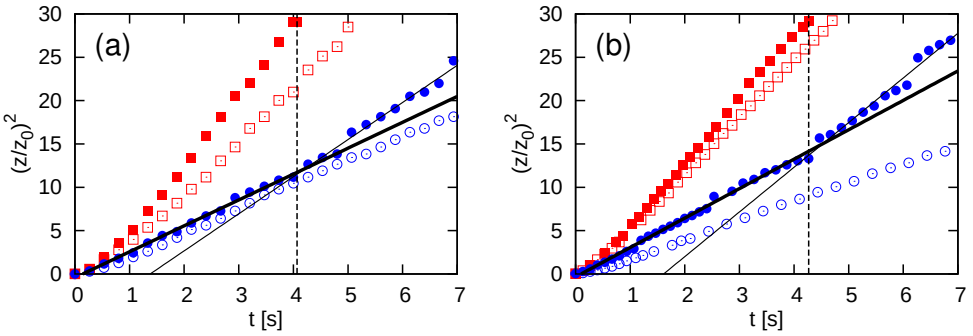

Fig. 6.9. Capillary rise on the artificial surfaces. The same plot as the plot in Fig.6.8(c) but for other substrates with different parameters: (l_c, W_c, L_c) = (10, 52, 30) for **(a)** and (l_c, W_c, L_c) = (20, 52, 60) for **(b)**, while (l_e, W_e, L_e) and (w, h) remain the same values as that for the reference substrate.

CT path, which will be discussed below. Furthermore, we could speed up the imbibition dynamics if we could stop the water front at each joint as seen that on the real leg, because such a temporal stop may cause a speed-up as seen in our demonstrations (Fig.6.8(c) and Fig.6.9); the imbibition dynamics on CHT path speeds up from the initial regime to the final regime, when the edge liquid reaches the top. Similarly to the case of the reference substrate (Fig.6.8(b, c)), the origins are shifted by small amounts which are much smaller than the overall imbibition lengths and do not affect practically the linear relation between z^2 and t.

6.2.3 Theory

To quantify our observation, we develop a theory describing the imbibition of the CT and ET paths, which have the same geometry while sizes are different. We shall construct of the theory by extending the scaling argument discussed in Sec.5.2, namely in [32]. Here, we assume the thickness of the imbibed film is comparable to the blade height h, which is reasonable when $h \gg w$ as discussed in [46] and indirectly proved in [32], and $h \gg w$ is well satisfied in the present case.

The capillary driving force F_γ per unit width of the imbibed liquid film is estimated as follows. As imbibed liquid front proceeds by the distance dz, the

surface energy increases by

$$dE = (1 - r)\gamma dz \tag{6.1}$$

per unit width in the case of complete wetting. Here, r is the roughness of the textured surface, namely,

$$r = 1 + \frac{2(l + w)h}{LW}, \tag{6.2}$$

where the set (l, W, L) corresponds to (l_c, W_c, L_c) and (l_e, W_e, L_e) on the CT and ET paths, respectively. Thus, the driving force is written as

$$F_\gamma = -\frac{dE}{dz} = \frac{2\gamma(l + w)h}{LW}. \tag{6.3}$$

On the other hand, the viscous friction acting on the liquid film is estimated in the following way. First, the CT or ET paths, on which an array of wide or narrow blades are placed respectively, can be regarded as a stripe of two regions: one with blades and the other without blades (Fig.6.10). In the region without blades, the friction on the film comes from the bottom surface of the substrate, *i.e.*, $f_{\eta B} = \alpha_0 \eta V/h$ per unit area, with the viscosity η of the liquid and the velocity V of the front of the liquid film. In the region with blades, in addition to the bottom friction, the friction with side walls of the blades, *i.e.*, $f_{\eta S} = 2\beta_0 \eta (V/w)h/W$ per unit area of the film, comes into play. Here, α_0 and β_0 are numerical coefficients roughly of order unity. While two types of friction come into play in the region with blades as discussed above, only side wall friction is dominant to the dynamics when $f_{\eta S} \gg f_{\eta B}$, *i.e.*, $2h^2 \gg wW$. In such a case, the total friction F_η can be estimated as a composite of the two types of friction on each region, namely, $f_{\eta B}$ in the region without blades and $f_{\eta S}$ in the region with blades. Thus, we obtain

$$F_\eta = f_{\eta B} z(1 - \phi) + f_{\eta S} z\phi, \tag{6.4}$$

where ϕ is the fraction of the region with blades, *i.e.*, $\phi = l/L$.

From competition of two forces, F_γ and F_η, we derive

$$z^2 = Dt, \tag{6.5}$$

where

$$1/D = \alpha_1(1 - \phi)/D_B + \beta_1 \phi/D_S. \tag{6.6}$$

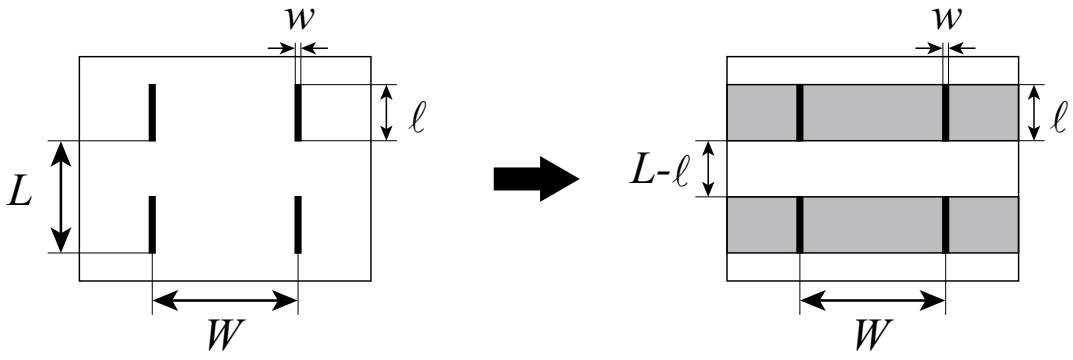

Fig. 6.10. Schematic front view of the CT or ET surface which can be regarded as "stripe" of two regions: one with blades (gray region) and the other without blades (white region).

Here, D_B and D_S are given as

$$D_B = \frac{\gamma}{\eta}\frac{(l+w)h^2}{LW}, \text{ and } D_S = \frac{\gamma}{\eta}\frac{(l+w)w}{L}, \tag{6.7}$$

where $\alpha_1 = \alpha_0/4$ and $\beta_1 = \beta_0/2$ are numerical coefficients roughly of order unity.

For later convenience, we note here two relations derived from the above equations:

$$D = \frac{F_\gamma}{F_\eta/(Vz)} \tag{6.8}$$

and

$$\frac{D_B}{(1-\phi)D} = \alpha_1 + \beta_1 \frac{\phi}{1-\phi}\frac{D_B}{D_S}. \tag{6.9}$$

Finally, the results of the theoretical argument (eq.(6.9)) can give some practical guiding principles for designing patterns, which have an advantage in water transportation. For the speed-up of imbibition, it is necessary to increase D with satisfying the assumption of the theory:

$$h \gg w \quad \text{and} \quad 2h^2 \gg wW. \tag{6.10}$$

One efficient way is to make h larger as realized on the real leg, while it is difficult to fabricate and thereby we decided a bit smaller value for our pattern. On the other hand, for efficient water transport, we may have to consider other factors, for example, flux. To keep enough flux, the condition $W \gg w$ should be important, also as realized on the real leg.

6.2.4 Comparison of experimental results and theory

To test the theory discussed above, we plot the coefficient D derived from the $t^{1/2}$ dynamics observed on the ET and CT paths for various (l, L, W) in Fig.6.11(a-c). Here, the assumptions of the theory, *i.e.*, eq.(6.10), are well satisfied in the data. We should note that, although rather technical, small shifts of origin introduced for Fig.6.8 and Fig.6.9 are not invoked to obtain the coefficient D here, because the shifts are due to clarify the dynamics in the unit of the podite length z_0.

The systematic trends in Fig.6.11(a-c), where dependences of the coefficient D on l, L and W are tested, are consistent with the above theory. In principle, the dependences are determined by a complex balance of changes in the driving force F_γ and the friction force F_η; the increase of F_γ tends to increase the speed, *i.e.*, increase D, while the increase of F_η tends to decrease D. However, the dependences are almost governed simply by the change in the driving force F_γ. For example, as W increases, the driving force F_γ decreases and the friction force F_η decreases, which results in the decreasing of D as shown in Fig.6.11(c) because of decreasing of driving force F_γ. This dominance of the driving force is consistent with the structure of eq.(6.8); differently from $F_\gamma = 2\gamma(l+w)h/(LW)$ in the numerator, $F_\eta = f_{\eta B}z(1-\phi) + f_{\eta S}z\phi$ in the denominator is composed of two terms $f_{\eta B}/V \simeq \eta/h$ and $f_{\eta S}/V \simeq \eta h/(wW)$ that are differently dependent on the lengths.

A more quantitative conformation of the validity of the theory is shown in Fig.6.12, where eq.(6.9) is tested. As predicted, all the data in Fig.6.11 and other three data are well on a straight line with $\alpha_1 = 13.1$ and $\beta_1 = 1.54$ (roughly of order unity as expected). With these values of α_1 and β_1, the composite theory well describes the systematic trends in Fig.6.11(a-c), as indicated by the theoretical curves.

Here, we note how we estimated the error bars in Fig.6.11 and Fig.6.12. We adopt two different ways: (1) For the data obtained from more than ten experiments (we always carried out each experiment with new substrate, thus, ten experiments mean experiments with ten different substrates with the same parameter set, here.), the standard deviation is used to estimate the error bars. With this way, error bars become symmetric with the mean. (2) For the data obtained from less than ten experiments, the maximum and minimum are indicated with the mean. With this way, error bars become asymmetric. The principal origin of the error bars is not in the difficulty of determining the co-

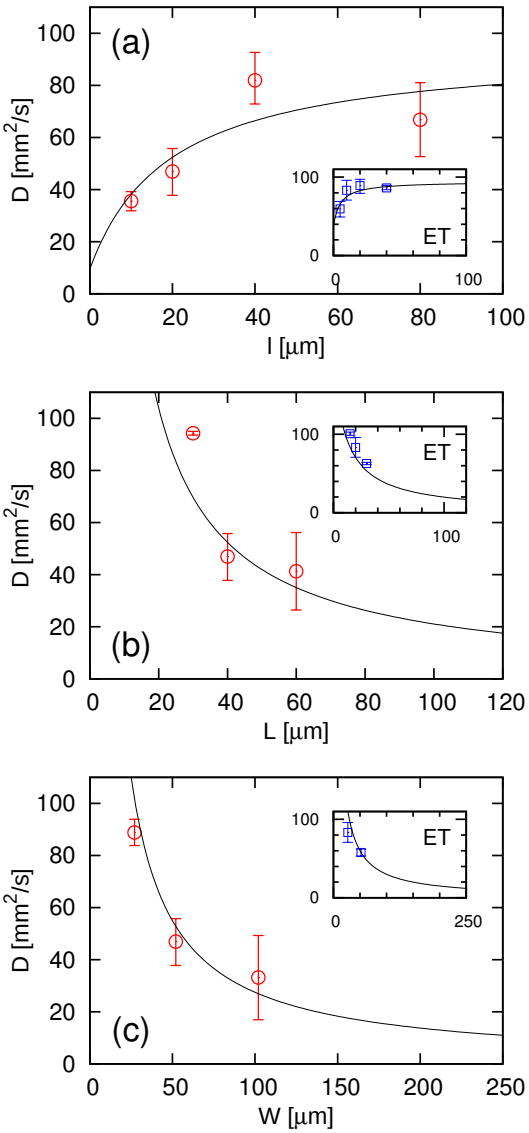

Fig. 6.11. Textured parameter dependences of the imbibition dynamics on the CT paths (○) and ET paths (□). **(a)** The coefficient $D = z^2/t$ vs the blade length l in the imbibed direction. (L, W) = (20+l, 52) for CT and (L, W) = (10+l, 27) for ET. **(b)** D vs the blade pitch L in the imbibed direction. (l, W) = (20, 52) for CT and (l, W) = (10, 27) for ET. **(c)** D vs the blade pitch W in the direction perpendicular to imbibition. (l, L) = (20, 40) for CT and (l, L) = (10, 20) for ET. The curved lines in both main and inset plots are based on eq.(6.9) with α_1 and β_1 determined by the straight line in Fig.6.12.

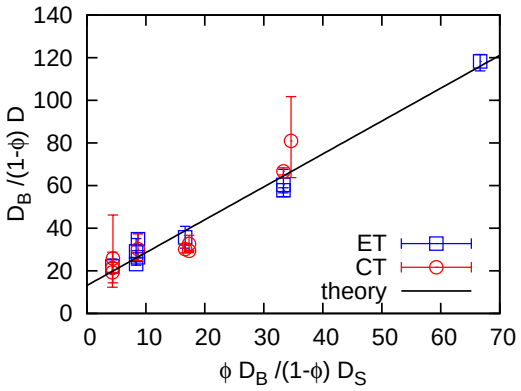

Fig. 6.12. Comparison of the data with the theory. All the data in Fig.6.11 and other three data are well on a straight line as predicted in eq.(6.9). The straight line is obtained by numerical fitting with α_1 and β_1. These values are used to obtain curved lines in both the main and the inset plots of Fig.6.11(a-c).

efficient D from $z^2 - t$ plot, but in the difficulty of attaining a homogeneously complete wetting state for water. This is caused by the fact that the effect of the irradiation of deep ultraviolet light is not robust, although the light treatment and the imbibition experiment were performed in different labs.

As mentioned in Sec.6.2.2, it is natural to expect that the initial "intermittent" $t^{1/2}$ imbibition dynamics observed in the central region of the HT paths (CHT) is described by the theory, if the effect of the edges and "joints" of the path is negligible. This is confirmed in Fig.6.13(a-c) and Fig.6.14. The systematic trends for each lengths in Fig.6.13(a-c) are quite similar to those in Fig.6.11(a-c). More quantitatively, the data are well on the straight line (solid one) with $\alpha_1 = 8.20$ and $\beta_1 = 1.68$ as shown in Fig.6.14, which is similar to that shown in Fig.6.12. Then, theoretical curves with these values (solid ones) give well explanation of the systematic trends in Fig.6.13(a-c). While the present composite theory does not include the effect of the joints, the theory still describes well the initial imbibition dynamics of the CHT path because the fraction of the joint regions is quite low.

Furthermore, the experimental result that imbibed motion of CHT paths is faster than that of CT paths is confirmed in Fig.6.13(a-c) and Fig.6.14; both of the facts that the solid curves are above than the dashed ones almost every region

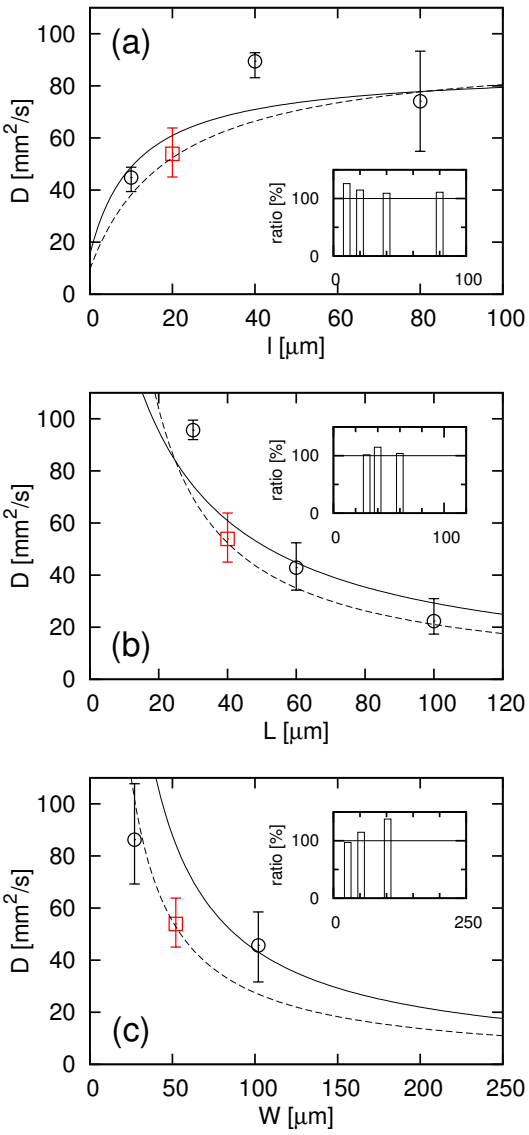

Fig. 6.13. Texture parameter dependences on the initial imbibition dynamics in the central region of the HT paths with the edge region specified by (l, L, W) = (10, 27, 20). **(a)** D vs l at (L, W) = (20+l, 52). **(b)** D vs L at (l, W) = (20, 52). **(c)** D vs W at (l, L) = (20, 40). The curved solid lines in (a-c) are based on eq.(6.9) with α_1 and β_1 determined by the straight line in Fig.6.14. The curved dashed lines are the solid lines in Fig.6.11, and the insets are the ratios of the mean values of D in the main plot of (a-c) to those in Fig.6.11(a-c). These show the effect of the edge region to the imbibition dynamics of the central region of the HT paths; the dynamics on the CHT paths is faster than that on the counterparts of the CT paths, except for two exceptional cases. The red symbol in each plot is the result with reference substrate, *i.e.*, (l, W, L) = (20, 52, 40).

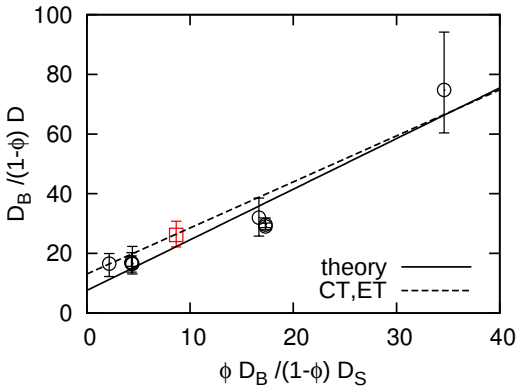

Fig. 6.14. Comparison of the data with the theory. All the data in Fig.6.13(a-c) are well on a straight solid line which is obtained by numerical fitting with α_1 and β_1. These values are used to obtain curved solid lines in the main plot of Fig.6.13(a-c). The dashed line is the solid lines in Fig.6.12, which shows the effect of the edge region to the imbibition dynamics of the central region of the HT paths; the dynamics on the CHT paths is faster than that on the counterpart of the CT paths. The red symbol is the result with the reference substrate, *i.e.*, (l, W, L) = (20, 52, 40).

in Fig.6.13(a-c) and the solid line is below than the dashed one in Fig.6.14 mean that D is larger for the CHT paths than that for the CT paths. Here, in each figure, the solid and dashed curves are theoretical curves obtained from fitting the data in Fig.6.14 and Fig.6.12, respectively; dashed curves in Fig.6.13(a-c) and Fig.6.14 are theoretical curves obtained from the results of CT and ET paths, namely solid curves in Fig.6.11(a-c) and Fig.6.12. In addition, the insets of Fig.6.13(a-c) indicate the fraction of the mean values of D in the main plot of Fig.6.13(a-c) to those in Fig.6.11(a-c), respectively. The faster imbibition in the CHT paths is clearly visible in the figures except for two exceptional cases, in which L or W is small; it seems that the edge effect tends to play an efficient role when the length scales in the edge region are small enough compared with those in the central region, which is similar to the real leg. Here, we note that the imbibition dynamics of the reference substrate is red data points in Fig. 6.13 and Fig.6.14.

6.3 Conclusion

Wharf roach (*Ligia exotica*) transports water from a water pool to its gills by using its VIth and VIIth legs. On some part of the outer surface of both legs, there is a path for water transport, which is covered with micro structures; for example, the 4th and the 5th podites of the VIth leg are covered with an array of two types of micro blades: wide blades at the central region of the path, and narrow blades at the edge regions and joints of the path. The path on the 3rd podite is covered with only narrow blades. Then, we found that capillary rise on the outer surface of the ranges from the 3rd to the 5th podites of the VIth leg is unusual non-slowing down dynamics on a coarse-grained level; imbibition length linearly scales with the elapsed time. Motivated by this unusual feature, we fabricated the artificial surfaces partially mimicking the surface of the 4th and the 5th podites of the VIth leg, *i.e.*, Hybrid Textured surfaces (HT). We furthermore fabricated Edge Texture (ET) covered with only narrow blades, and Central Texture (CT) covered with only wide blades. We found a usual slowing down dynamics for imbibition of ET, CT, and the initial regime of the imbibition of the central region of the HT, unlike the case with the VIth leg. This dynamics is well described by the scaling law developed in [6] for "stripe" textures. Although we could not obtain non-slowing down dynamics for imbibition of the

artificial surfaces, we found that the imbibition of the hybrid textured surfaces have advantages for transportation; the imbibition of the central regions of the HT paths is faster than that of the CT paths.

It is noteworthy that our artificial textured surfaces do not completely mimic the surface of the real leg. At first, we mimicked only its 4th and 5th podites. Then, the real structure in each podite is rather inhomogeneous, possibly with gradients of the texture and wettability. The real blades are higher and thinner and probably bendable compared with that of mimicking ones. In addition, blades are sometimes tilted on the surface. These features may cause the complex imbibition front on the microscopic scale instead of the horizontal line of imbibition front as shown in the imbibition of artificial surfaces, then may lead to the "waiting" behavior, *i.e.*, the imbibition front seems to start proceeding to the next podite only after the lower podite is almost filled. The "waiting" motion might lead to the linear dynamics on a macroscopic scale. Faithful mimicking of the real structure and clarifying the reason why the linear dynamics results in the case of natural wharf roach will be future problems.

Chapter 7

Imbibition of Open Capillary

As discussed in Part II Previous Study, imbibition dynamics with different exponents of scaling laws ($z \sim t^{1/2}$ and $z \sim t^{1/3}$) has been found. The difference seems to be caused by geometries and sizes of the pillars on textured surfaces. To understand the cross-over of the exponents and to understand its physical details, we study capillary rise with much simpler samples: open capillaries with cross-sections being rectagular shape. Open capillaries or channels are also useful for application. Here, we shall describe imbibition of open capillary based on the paper [41], which includes fundamental discussion and applications.

7.1 Open capillary

To study the capillary rise into an open capillary, we fabricated open channels whose cross-sections are rectangular shapes and lengths are around several centimeters. Here, hard transparent PMMA (poly(methyl methacrylate)) plates are used. On the plate, we fabricated open channels by a computer numerical controlled (CNC) micro-milling system (MM100, Modia Systems) with a rigid drill (NS Tool). The length of the channel, which is about several centimeters, depends on the size of the PMMA plate we used. The width w and depth d of the channel are around sub-millimeters, which depend on the milling conditions, such as drill tip diameter, length, velocity, process numbers, and so on. Here, we designed channel width $w = 0.2$ mm and depth $d = 0.2 - 1.0$ mm, respectively, in order to satisfy $2d > w$ to make theoretical prediction easier. Then, we fabricated it with drill tip whose diameter is 0.2 mm. Values of w and d of fabricated open channels are slightly different from the designed values and slightly

inhomogeneous along the channels because of the dependence on the milling conditions. For example, the values of w obtained by "point-measurements" by a digital microscope (Keyence VHX-100) were in the range 0.201 - 0.206 mm, not exactly equal to the tip diameter 0.2 mm. For these reasons, we adopted the averaged values of w instead of "point'-measured" w in this study. As be written in sec.7.3, capillary rise into the open channel stops at a certain height, which depends on the width of the channels w (eq.(7.1)). Thus, the average value w can be estimated by calculating from the final height z_f obtained from experiment.

To test repeatability at the same time, we fabricated six open channels with the same geometrical parameters, which are parallel to each other on the same PMMA plate.

7.2 Overview of the experiment

Similarly to other imbibition experiments which we have already seen in this thesis, we carried out imbibition experiments with open channels. Let an end of the channels perpendicularly touch with the horizontal surface of a liquid bath. Then, liquid rises up against gravity. We took snapshots of the phenomenon by a USB camera (CMOS130-USB2, Fortissimo) with a lens (VS-LD20, Fortissimo) as shown in Fig.7.1(a), then analysed them with Image J. Here, we used viscous liquids, poly-dimethylsiloxane (PDMS) solutions (commonly known as silicone oils) with different viscosities, $\nu = 50, 100, 500$cS. PDMS completely wets PMMA substrate, namely contact angle between them is zero.

A typical time evolution of the rising dynamics is demonstrated in a series of snapshots in Fig.7.1(a). At later stage, two different fronts of the liquid become distinguishable as indicated by two arrows: yellow and blue. This seems to be followed from that a thin precursor film (PF; indicated by blue arrows) develops gradually ahead of the front of the bulk liquid column (LC; indicated by yellow arrows), below which the rectangular channel is almost completely filled. The positions of two fronts, one for the precursor film (PF) and the other for the liquid column (LC), are plotted as functions of the elapsed time t, together with the difference between PF and LC, *i.e.*, the length of precursor film (LPF), in Fig.7.1(b). Here, the origin of the vertical axis is the position of the meniscus of the liquid bath, and that of the horizontal one is the time when meniscus becomes stable because the surface of liquid bath moves a little after touched by

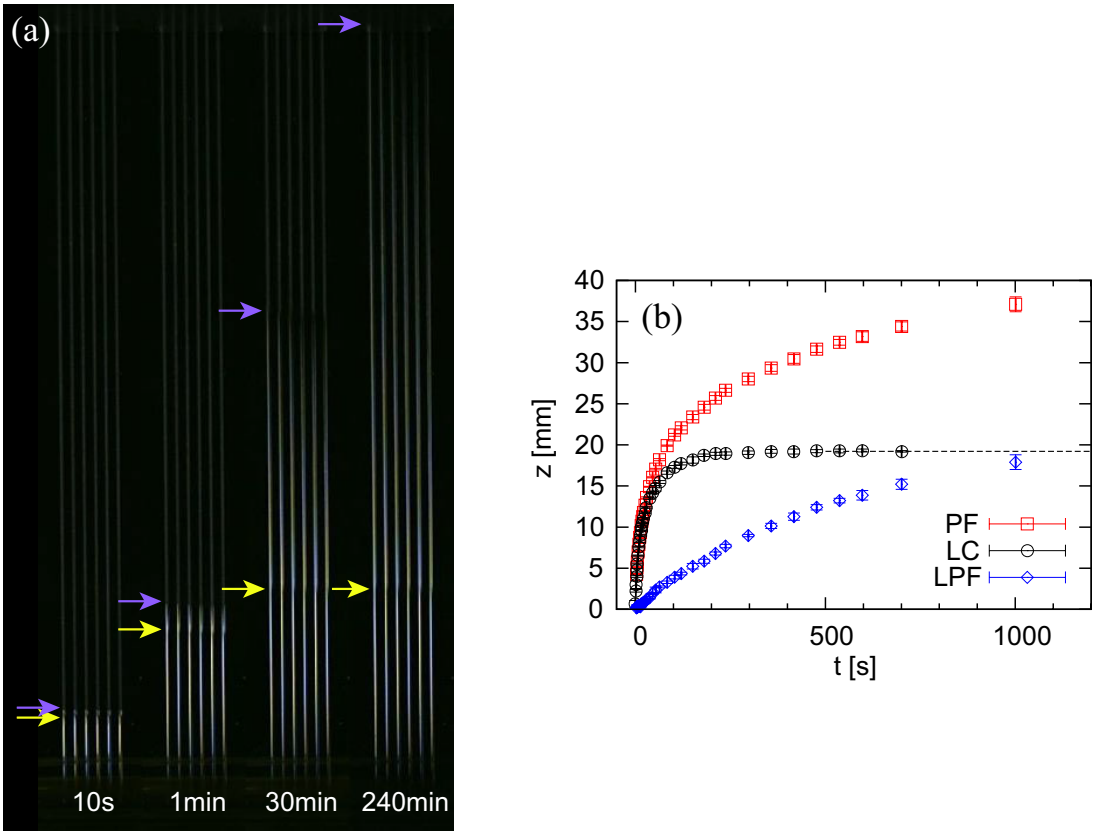

Fig. 7.1. Global dynamics of capillary rise into open channels whose depth d and width w is $(d, w) \simeq (0.4, 0.2)$ mm. **(a)** A typical time evolution of the rising dynamics. Liquid (PDMS; viscosity $\nu = 100$cS) rises up into six channels with same geometrical parameters ($d \simeq 0.4$mm and $w \simeq 0.2$mm) micro-milled parallel to each other, when an end of the channels is touched with the horizontal surface of the liquid bath. The precursor film (PF) develops with time ahead of the top of the bulk liquid column (LC), below which the rectangular channel is almost completely filled with liquid. Front positions of PF and LC are indicated by the blue and yellow arrows, respectively. The snapshot shows good repeatability. **(b)** Front positions of the PF and LC, and the difference of two, *i.e.*, the length of precursor film (LPF), are plotted as functions of the elapsed time t. Here, the origin of the vertical axis is the position of the meniscus of the liquid bath, and that of the horizontal one is the time when meniscus becomes stable because the surface of liquid bath moves a little after touched by the sample. The values are the averaged ones of those in six channels, and error bars indicate their standard deviations. It shows good repeatability. The dotted horizontal line indicates the final height of LC; z_f. Both figures are reprinted from [41].

the sample. Each position or length is the averaged value of that in six channels, and error bars indicate its standard deviation. As shown in the snapshots and the plot, the rising front of the liquid column (LC) saturates to a certain height similarly to capillary rise in tubes, while the precursor film (PF) continues to proceed to the top of the plate (as shown in snapshot on 240min. in Fig.7.1(a)).

7.3 Statics and dynamics of bulk liquid column

Here, we shall discuss the statics and dynamics of the bulk liquid column (LC). As shown in Fig.7.1, the front of the bulk liquid column proceeds with decreasing the rising velocity, then stops at a certain height. The time evolution of the front height of LC for different experimental parameters is shown in Fig.7.2(a), where rising height z_{LC} of LC is plotted as a function of the elapsed time t. Experimental parameters are channel depth d and the kinetic viscosity of the liquid ν ($= \eta/\rho$, with the viscosity η and the density ρ). The channel width w is kept about 0.2 mm, which may be slightly different because it depends on milling conditions. As shown in the plot, the final saturated height of the liquid column seems to be independent of viscosity ν, and dependent weakly on the channel depth d. To predict the final height z_f of LC, we assume that the cross-section of the liquid column is rectangular whose area is denoted by wd. In this case, similarly to the case of capillary rise in tubes in sec.4.2, the total energy $U(z)$ is given as follows:

$$\begin{aligned} U(z) &= \{2d(\gamma_{SL}-\gamma_S)+w(\gamma+\gamma_{SL}-\gamma_S)\}z+\int_0^z \rho g z' w d \, \mathrm{d}z' \\ &= -2d\gamma\cos\theta_E + w\gamma(1-\cos\theta_E)z + \frac{\rho g w d z^2}{2} \\ &= -2d\gamma\left\{\cos\theta_E + \frac{(\cos\theta_E-1)w}{2d}\right\}z + \frac{\rho g w d z^2}{2} \\ &= -2d\tilde{\gamma}z + \frac{\rho g w d z^2}{2}, \end{aligned}$$

where, Young's law ($\gamma_{SL}+\gamma\cos\theta_E=\gamma_S$, θ_E is the equilibrium contact angle between the liquid and the substrate), and $\tilde{\gamma}=\gamma\{\cos\theta_E+(\cos\theta_E-1)w/(2d)\}$ are used. Here, g is the gravitational acceleration and γ is surface tension of the liquid, respectively. Minimizing $U(z)$ in terms of z, we obtain the final height

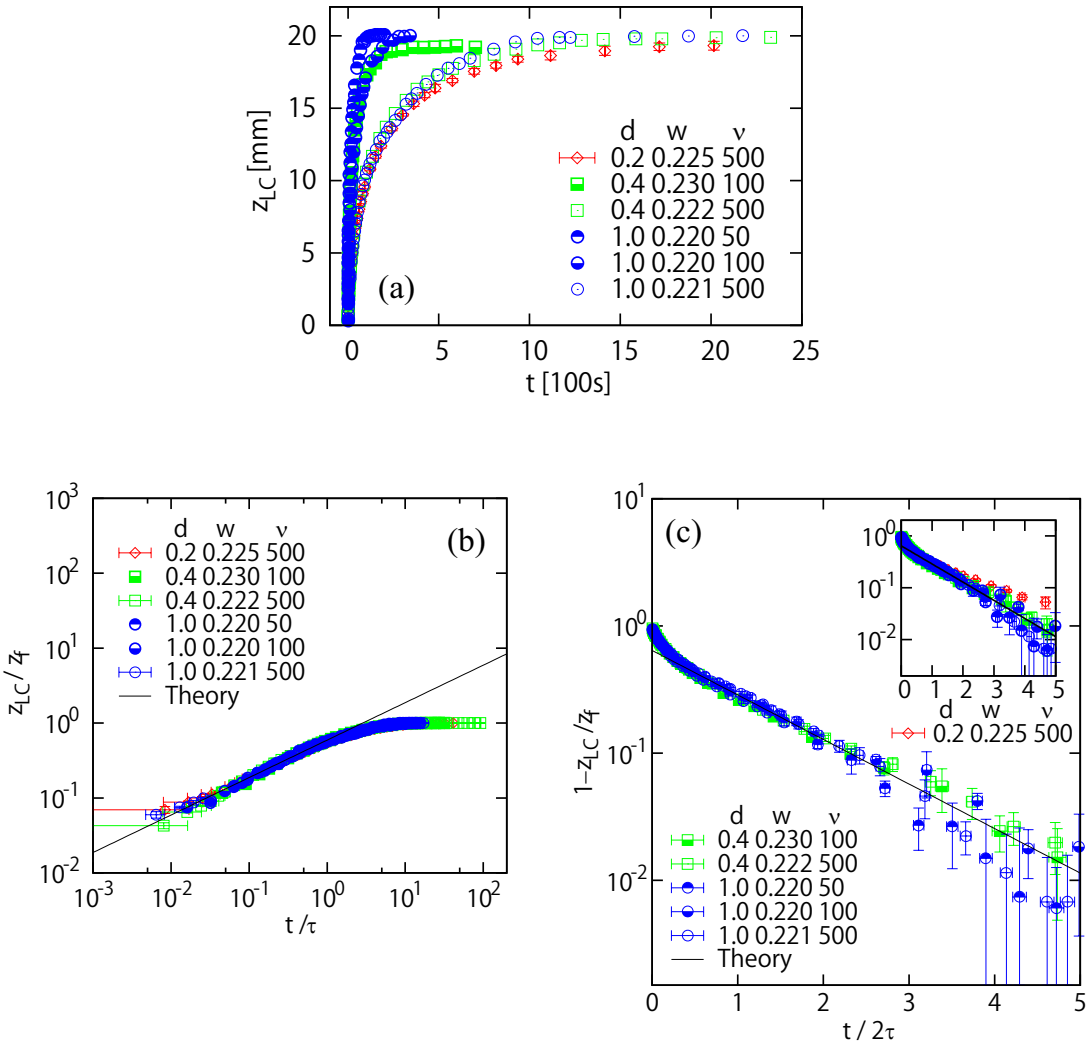

Fig. 7.2. Dynamics of liquid column (LC). **(a)** Imbibition height of liquid column z_{LC} is plotted as a function of the elapsed time t for different experimental parameter sets (d, w, ν), where d is the channel depth, w is the channel width calculated from final height z_f, and ν is the liquid viscosity, respectively. Error bars are generally small as represented by those of the data for $(d, w, \nu) = (0.2, 0.225, 500)$. Error bars are sometimes suppressed for simplicity. **(b)** Collapse of all the data in the initial regime by the predicted theory, showing that the scaling laws eq.(7.3) or eq.(7.4) obtained in the deep-channel limit are robust and hold well even for rather shallow channels. Error bars are sometimes suppressed for simplicity. **(c)** Collapse of the data in the final regime by the predicted theory (eq.(7.6) or eq.(7.7)). The data for $d = 0.2$ mm are removed here because they do not well satisfy the assumption of the approximate theory, $2d \gg w$. The inset shows the same plot but added the data for $d = 0.2$mm. All figures are reprinted from [41].

$z = z_f$ as

$$z_f = \frac{2\tilde{\gamma}}{\rho g w}. \tag{7.1}$$

In the present complete wetting case, contact angle $\theta_E = 0$, so that $\tilde{\gamma} = \gamma$. As a result, in the present case eq.(7.1) is written as

$$z_f = \frac{2\gamma}{\rho g w}. \tag{7.2}$$

This formula reproduces the experimental results quite well in the range of parameters used in the present study; the assumption that the cross-section of the liquid column is rectangular is well satisfied in the present case. According to this, we can estimate the average value of channel width w from the final height z_f obtained from the experiment as mentioned in sec.7.1. For example, we experimentally obtained $z_f = 20.1 \pm 0.1$ mm for depth $d = 1.0$ mm ("point-measured" value of d is $d = 0.98 \pm 0.02$ mm) and viscosities $\nu = 50$ and 100cS. This value of z_f with eq.(7.2) gives $w = 0.220 \pm 0.001$ mm ($\gamma = 20.8$ and 21.0 mN/m, $\rho = 0.960$ and 0.965 g/cm^3 for $\nu = 50$ and 100 cS, respectively). This calculated value of w is slightly different from the average of the limited number of "point-measured" values of w, 0.20±0.00 mm. In addition, the width is slightly inhomogeneous along the channels. For these reasons, we adopt the calculated average value as the channel width $w = 0.220 \pm 0.001$ mm, here. In the same spirit, in Fig.7.2 we use z_f as the obtained value from the experiment, not the calculated value from the "point-measured" w on the basis of eq.(7.2). It is to be noted that the weak dependence on d of z_f in Fig.7.2 comes from the slight differences in w. Here, the values of d in the plot are designed values, not the exact ones obtained from the "point-measurement", although this differences give no effect; indeed, the statics and the dynamics are independent of the channel depth d with $2d \gg w$.

The dynamics in the initial (viscous) regime can be described by the competition of the two forces: capillary force driving the phenomenon and viscous drag friction. To estimate the capillary force, we begin with discussing the shapes of the free surface of the liquid column like in sec.5.1. Although the rectangular assumption works well, the surface of the liquid column filling open channels becomes concave with height to guarantee the pressure drop. Thus, the equation determining the final height of the LC can be understood as the balance between

the gradients of the hydrostatic (gravitational) pressure and of Laplace pressure;

$$\rho g = \left.\frac{\partial(\Delta p)}{\partial z}\right|_{z=z_f}.$$

Here, $\Delta p = \gamma C(z)$ is Laplace pressure drop, *i.e.*, $\Delta p = p_0 - p(z) > 0$ with atmospheric pressure p_0, and $C(z) > 0$ is the curvature of the liquid-air interface of the LC at the height z. On the other hand, eq.(7.2) is written in the form $\rho g = 2\gamma/(wz_f)$. These equations imply the curvature $C(z) \simeq (2/w)\log(z/z_0)$ $(z > z_0)$. As a result, the curvature at the top of the liquid column $(z = z_{LC})$ is described as $C_{LC} = C(z_{LC}) \simeq 2/w$. The curvature of the free surface of the LC increases from zero (flat surface) at the bottom to $2/w$ at the top. Thus, we can estimate the capillary force per unit volume as

$$f_\gamma = \frac{1}{z_{LC}}\,\gamma\,\frac{2}{w} = \frac{2\gamma}{wz_{LC}}.$$

Now, let us estimate the viscous drag friction. We consider the case where the viscous dissipation associated with the side wall of the channel is dominant over that associated with the bottom surfaces of the channel, *i.e.*, $\eta(V/(w/2))^2 \gg \eta(V/d)^2$, or equivalently, $w^2 \ll 4d^2$, which is fairly well satisfied in the present study. In this case, the viscous friction per unit volume is written as

$$f_\eta = 3\eta\frac{V}{(w/2)^2} = 12\eta\frac{V}{w^2}$$

by virtue of the argument in sec.3.3.1 and eq.(3.20).

From competition of the capillary force f_γ and the viscous drag friction f_η with an approximation $V \simeq \mathrm{d}z_{LC}/\mathrm{d}t$, the dynamics of LC in the viscous regime is derived as follows:

$$\frac{2\gamma}{wz_{LC}} = 12\eta\frac{V}{w^2},$$

or

$$z_{LC}\frac{\mathrm{d}z_{LC}}{\mathrm{d}t} \simeq \frac{\gamma w}{6\eta}.$$

Integrate this with respect to t, so that we have

$$\frac{z_{LC}^2}{t} \simeq \frac{\gamma w}{3\eta},$$

or

$$z_{LC} \simeq \left(\frac{\gamma w}{3\eta}\, t\right)^{1/2}. \tag{7.3}$$

By using z_f given in eq.(7.2), the normalized imbibition dynamics is obtained as

$$\frac{z_{LC}}{z_f} = k_1 \left(\frac{t}{\tau}\right)^{1/2} \quad \text{with} \quad \tau = \frac{12\gamma\eta}{\rho^2 g^2 w^3}, \tag{7.4}$$

where k_1 is a numerical constant. This constant is close to one when the infinite-plate approximation is good, *i.e.*, $w \ll d$.

In the final (visco-gravitational) regime, the dynamics can be described by the competition of three forces: capillary force, gravitational force, and viscous friction. The same approximation and assumption for the initial dynamics are used here: the flow in the channel is Poiseuille flow, the viscous dissipation associated with the side walls of the channel is dominant when the infinite-plate approximation is valid ($w^2 \gg 4d^2$), and the curvature of the free surface of the liquid column at the top is written as $C_{LC} = 2/w$. Then, the force balance per unit volume is expressed as $2\gamma/wz_{LC} = 12\eta V/w^2 + \rho g$. Multiplying both side of this formula by $z_{LC}/\rho g$ leads to $2\gamma/(\rho g w) = 12\eta V z_{LC}/(\rho g w^2) + z_{LC}$, or equivalently

$$z_f = \frac{12\eta V z_{LC}}{\rho g w^2} + z_{LC}. \tag{7.5}$$

At the final stage, the front of the LC reaches to the final height z_f. Thus, it is reasonable to define the difference $\Delta z_{LC} = z_f - z_{LC}$ and assume that Δz_{LC} is small. Under this assumption, we can express mean rising velocity $V = \mathrm{d}z_{LC}/\mathrm{d}t = -\Delta\dot{z_{LC}}$ as follows.

$$\Delta z_{LC} = z_f - z_{LC} = \frac{12\eta V z_{LC}}{\rho g w^2} = \frac{12\eta}{\rho g w^2}(-\Delta\dot{z_{LC}})(z_f - \Delta z_{LC}).$$

From this, it follows

$$\Delta z_{LC} \simeq -\frac{12\eta}{\rho g w^2} z_f \Delta\dot{z_{LC}}$$

or

$$\Delta\dot{z_{LC}} \simeq -\left(\frac{\rho g w^2}{12\eta z_f}\right)\Delta z_{LC}.$$

Then, finally we obtain

$$z_f - z_{LC} = k_2 z_f e^{-k_3 t/(2\tau)}, \tag{7.6}$$

where τ is given in eq.(7.4), k_2 is a constant of integration, and k_3 is a constant close to one for $w \ll d$ (as far as the infinite-plate approximation is valid). To test this formula, we write it in a normalized form,

$$\log\left(1 - \frac{z_{LC}}{z_f}\right) = -k_3\left(\frac{t}{2\tau}\right) + \log k_2. \tag{7.7}$$

These formulas well describe the experimental results for both the initial and final imbibition dynamics. In Fig.7.2(b), where eq.(7.3) or (7.4) is tested, all the data collected from Fig.7.2(a) collapse remarkably well onto the predicted master curve with $k_1 = 0.592 \pm 0.003$. Here, the condition for the approximation is $2d/w \gg 1$, while the values of $2d/w$ are 10, 4 and 2 for $d = 1.0$, 0.4 and 0.2 mm, respectively; the scaling law obtained in the deep-channel case is valid even for rather shallow channels. The initial regime is practically valid when $z_{LC} < z_f/2$ (half of the final height) as seen in Fig.7.2(b). In Fig.7.2(c), the dynamics in the final regime, eq.(7.6) or (7.7) is tested. All the data collapsed onto a single straight line with $k_2 = 0.642 \pm 0.007$ and $k_3 = 0.806 \pm 0.013$ in the main plot, where the data for $d = 0.2$ mm are removed because the data for $d = 0.2$ mm do not satisfy the deep-channel approximation ($2d/w = 2$). In fact, the inset where the data are added shows a slight deviation of the data for $d = 0.2$ mm.

7.4 Dynamics of length of precursor film

As indicated above, the precursor film (PF) does not seem to stop (as long as the evaporation of the film is negligible), which reminds us of the capillary rise into corners [34] and [35], and on textured surfaces decorated with short and round pillars [36] (cf. sec.5.3). It should be emphasized that "precursor film (PF)" in the present study is different from the precursor film observed in Tanner's experiment which is discussed in Appendix B. Our "precursor film (PF)" means rather the capillary rise into corners. In this section, we shall discuss the dynamics of the length of precursor film, which is denoted by "LPF" in the Fig.7.1(b).

Similarly to previous studies, a universal scaling form for the imbibition length h is derived as follows: the capillary driving force per unit volume is written as $\gamma C/h$. Here, we assumed the case of complete wetting, *i.e.*, $\tilde{\gamma} = \gamma$; h is the length of precursor film (LPF), and C is the curvature of the free surface of PF

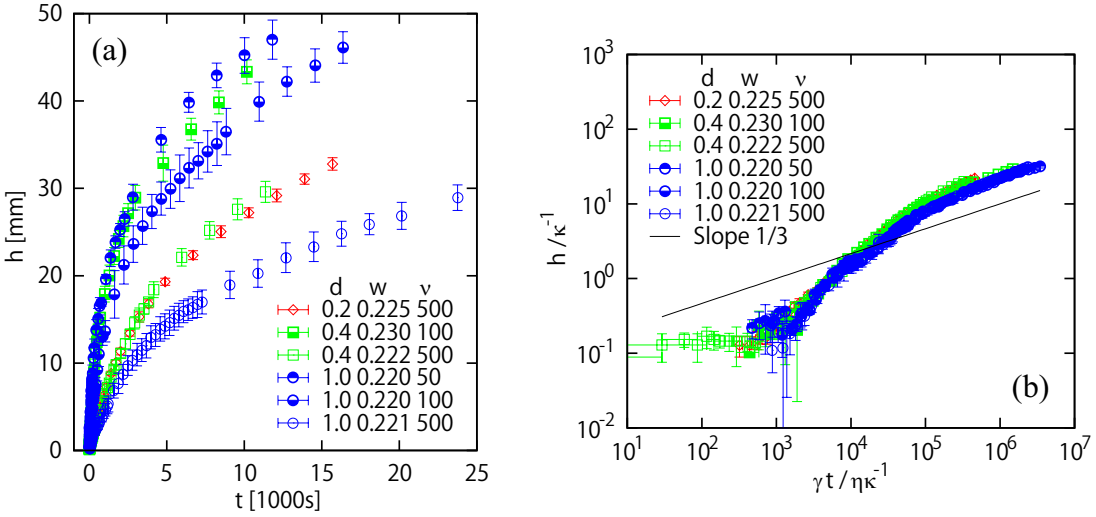

Fig. 7.3. Dynamics of the length of the precursor film (LPF). **(a)** The length of the precursor film h is plotted as a function of the elapsed time t for different experimental parameter sets (d, w, ν), where d is the channel depth, w is the channel width calculated from final height z_f and ν is the liquid viscosity, respectively. **(b)** Collapse of all the data by predicted theory. Their slopes correspond to the straight line indicating 1/3 power law in the final regime ($h/\kappa^{-1} \gg 10$). This shows that the universal scaling form eq.(7.8) or eq.(7.9) obtained in the deep-channel limit well describes experimental result in the final regime of the increasing of the length of precursor film. Both figures are reprinted from [41].

at the height h. This capillary force is balanced with the viscous friction $\eta\nabla^2 V$ and the gravitational force ρg. Here, these three forces affect the phenomenon, namely, the scales of these forces seem to be comparable. First, by balancing the capillary force with the gravitational force, the curvature C is estimated as $C^{-1} \approx \gamma/(\rho g h)$. This length scale C^{-1} becomes smaller with height, which means that C^{-1} is an appropriate length for the viscous length, *i.e.*, $\eta\nabla^2 V \approx \eta C^2 V$. By balancing this viscous term with ρg (or equivalently with $\gamma C/h$), we get

$$\eta C^2 V \approx \eta \left(\frac{\rho g h}{\gamma}\right)^2 V \approx \rho g,$$

and hence,

$$h^2 V \approx \frac{\gamma^2}{\rho g \eta}.$$

Using an approximation $V \approx \mathrm{d}h/\mathrm{d}t$, we obtain the scaling law

$$h \approx \left(\frac{\gamma^2 t}{\rho g \eta}\right)^{1/3}. \tag{7.8}$$

Since the film thickness cannot exceed w, this treatment is valid only for $C^{-1} < w$, which implies that the existence of the precursor film tends to be suppressed for small height and small effective gravity. Namely, we could not observe precursor films in experiments carried out horizontally. This scaling law eq.(7.8) does not include any geometrical parameters of the channel such as d or w, so that we can say a universal scaling law in this sense. The dimensionless form of eq.(7.8) is

$$\frac{h}{\kappa^{-1}} \approx \left(\frac{\gamma t}{\eta \kappa^{-1}}\right)^{1/3}, \tag{7.9}$$

where $\kappa^{-1} = (\gamma/\rho g)^{1/2}$ is the capillary length.

This universal scaling form well describes experimental results as shown in Fig.7.3. Fig.7.3(a), where the length of precursor film h is plotted as a function of the elapsed time t for different channel depth d and liquid viscosity η, implies that the dynamics of proceeding of the LPF depends on viscosity, and possibly on channel depth. However, in Fig.7.3(b), which is the same plot but whose axes are renormalized according to eq.(7.9), all of the data collapse and their slope correspond to the theoretical line indicated as "slope 1/3" in the final regime ($h/\kappa^{-1} \gg 10$). The fact that the dynamics seems to depend on channel depth

d was the misunderstanding caused by the difference in the initial regime of the dynamics. The dynamics of the LPF in the later time does not depend on any geometrical parameters of the channel as shown in eq.(7.9), namely the scaling form of the dynamics is universal in this regime. This limited agreement is fully consistent with the prediction, which holds only in the limit when $h \gg z_f$, *i.e.*, $h/\kappa^{-1} \gg z_f/\kappa^{-1}$ with $z_f/\kappa^{-1} = 2\kappa^{-1}/w$ being in the range from 12.9 to 13.5. Note that if channel were too long, the problem of the evaporation would come into play.

7.5 Applications

To show capabilities of open channels for micro mixing devices, we designed and fabricated devices with open channels, and then demonstrated two different types of experiments: one is the multiple color changes of the BTB solution, and the other the expression of the Green Florescence Protein. In this section, we shall describe these two experiments, and then discuss the capability of our devices as new devices. Here, it should be emphasized that we could not observe any effect of the precursor film in the two demonstrations, where the devices were placed in horizontal; the precursor film tends to disappear in the small gravity limit, and thus the curvature C of the free liquid-air interface defined as $C^{-1} \approx \gamma/(\rho g h)$ equals zero.

7.5.1 Color changes of the BTB solution

We designed a simple device for mixing one solution with four different solutions and carried out experiments with that (Fig.7.4). The device consists of one circular spot, four square spots, and open channels connect the circular spot and each square one as shown in Fig.7.4(a). The width of open channels is about 0.2 mm, which is similar to that of open capillary used in the previous sections. The depth is chosen as $\simeq$ 0.6 mm, which seems still to satisfy deep channel limit according to the results that the scaling law eq.(7.3) or eq.(7.4) describes experimental results well even for d = 0.2 mm, at least for d = 0.4 mm as shown in Fig.7.2(b). It is practically good because the deeper channel needs the larger volume of liquids, while liquids are generally quite expensive in the case of DNA solutions or proteins. Then, we determined the depth and diameter of the circular spot as 0.3 mm and 4 mm, and the depth and width of the square

spots as 1.7 mm and 2 mm, respectively, by taking into account the volume of the mixing liquid, and the depth and size of the square spots in order to obtain visible color changes.

In addition, we performed a surface treatment to make the surfaces more wettable for the aqueous solutions. We performed the oxygen plasma etching to the entirety of the sample, namely the side and bottom surfaces of channels and the circular and square spots, by an apparatus (FA-1, Samco) under the following condition: RF power 25 W, O_2 flow flux 10 ml/min., treating time 10 s. Furthermore, the path surface is made further more hydrophilic by applying hydrophilic coating liquid (WG-R1, Marusyo Sangyo), while spots are not added this treatment to avoid leak of the solutions from the spots.

We first deposit four solutions at the square spots, which are pinned by the edges of the spots, and then inject another solution in the circular spot. Soon after injection, the solution flows in the channels, and reaches the four square spots at the same moment.

We demonstrated with the BTB solution and 4.8 mm^3 of four solutions with different pH (1.2, 6.9, 10.4, and 12.8, respectively). As shown in the snapshots (Fig.7.4(b)), soon after the injection of the BTB solution at the left circular spot ($t = 0.00$ s), the BTB solution flows and arrived at the four square spots. Then it starts mixing with each solution in each spot, and thus color of the solution in each spot starts changing at the same time ($t \simeq 1.5$ s). The proceedings of the color changes are shown in Fig.7.4(c), where normalized mean brightness of spots (from S1 to S4) are plotted as a function of the elapsed time. Also from this plot, we can confirm that the mixing at each square spot starts almost at the same time ($t \simeq 1.5$ s).

The pictures (Fig.7.4(b)) were obtained from a movie taken by a digital camera (D800E, Nikon) with a macro lens (AF-S Micro NIKKOR 60mm f/2.8G ED, Nikon). The brightnesses plotted in Fig.7.4(c) are calculated on the basis of an equal weight average of 256-step brightnesses for RGB colors obtained from a central part of the spot (80 % of the spot area) by using Image J.

7.5.2 Expression of GFP

We further fabricated a simpler device for mixing two solutions and demonstrated a biochemical reaction, the expression of green florescence protein (GFP), with this device.

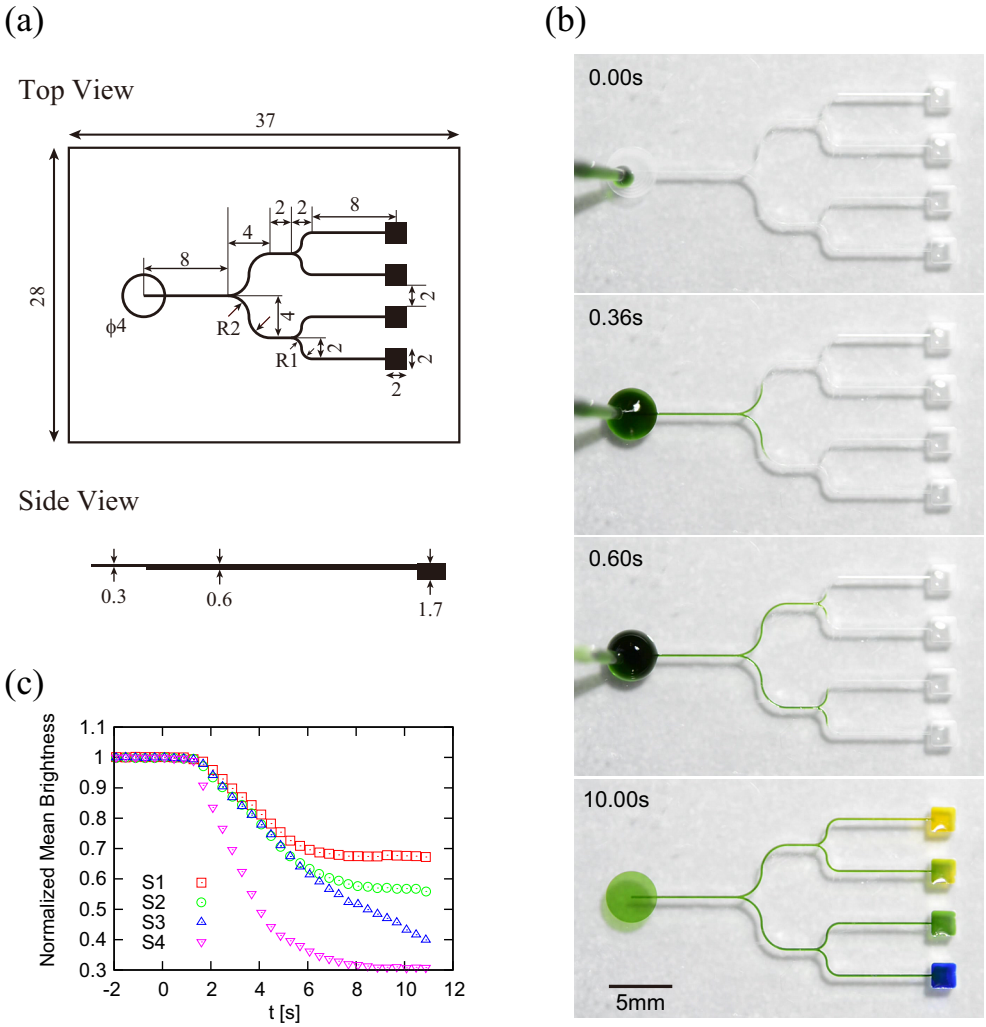

Fig. 7.4. Multiple color changes of the BTB solution. **(a)** Top and side view of a micro devices for mixing one solution with four different solutions. All the numbers are lengths whose units are mm. **(b)** A demonstration of the device. First, 4.8 mm^3 of four solutions with different pH are deposited in the right square spots (pH=1.2, 6.9, 10.4, and 12.8, in order from the top to the bottom spots), which are pinned by the edges of the spots. When the BTB solution, which is injected in the left circular spot, arrives at each square spot and starts mixing with the solution in each spot ($t = 0.00$ s), the colors change almost at the same time. **(c)** Normalized mean brightness vs time. The brightness of all the four spots (from S1 to S4, in order from the top to the bottom) starts to decrease from the initial value (all normalized to one) almost simultaneous ($t \simeq 1.5$ s). (a) and (b) are reprinted from [41], supplemental information and Fig.3(a).

The device consists of two circular spots S1 and S2 whose diameters are 3 mm, one square-shaped mixing spot M (1 mm $\times$ 1 mm) and open channels C1 and C2 connect the circular spots and the mixing spot as shown in Fig.7.5(a). The width and depth of the channels are designed 0.2 mm and 0.6 mm, respectively, similarly to that in the case of the previous one. The depth of the mixing spot is same, and that of circular spots are 2.0 mm. Then, we performed a surface treatment to the entirety of the device to make the surface more wettable for the aqueous solutions. The oxygen plasma etching was performed under the same condition as that for devices for the previous one except the treatment time 30s instead of 10s for the previous case. Soon after two different solutions are injected in each circular spot at the same time ($t = 0$ min.), the solutions flow and arrive at the mixing spot almost at the same time (a bit different because the flow velocity depends on viscosity of the liquid, but the time difference is sufficiently smaller than reaction time), and the synthesis of the protein starts in the mixing spot as shown in Fig.7.5(b).

The details of the protein expression are given below. We used a commercial kit to express GFP (S30 T7 High-Yield Protein Expression System, Promega). The cell-free protein synthesis was performed by mixing two solutions: 20 mm^3 of Liquid 1 containing DNA, and 20 mm^3 of Liquid 2 containing mimicking cytoplasm or protein expression system in bacteria (E.coli). More specifically, the Liquid 1 is obtained by mixing S30 Premix Plus (15.0 mm^3) and T7-S30 Extract for Circular DNA (13.5 mm^3), and the Liquid 2 is obtained by plasmid DNA encoding GFP (1.5 mm^3) and Nuclease-Free water (27.0 mm^3).

The expression of GFP was observed under a fluorescence microscope (IX71, Olympus) equipped with an objective lens (10$\times$) and a color CCD camera (DP80, Olympus) after the injection of the solutions (Fig.7.5(b)). The exposure time and ISO are fixed to 200 ms and 800, respectively. The brightnesses of the mixing spot (80 % of the spot area) in the pictures are multiplied by 256/140 times for RGB colors by using Image J (0-139 grade is scaled up to 0-255 grade). We plotted the mean brightness as a function of the time for three independent experiments for quantitative discussion. The data labeled 3 in the plot correspond to the experiment shown in Fig.7.5(b). The filled symbols indicate that the liquid in the mixing spot M is almost completely evaporated as seen in the bottom snapshot in Fig.7.5(b), which suggests that the evaporation is not significant for the duration approximately 40 min. after the reaction starts. Furthermore, the reaction time

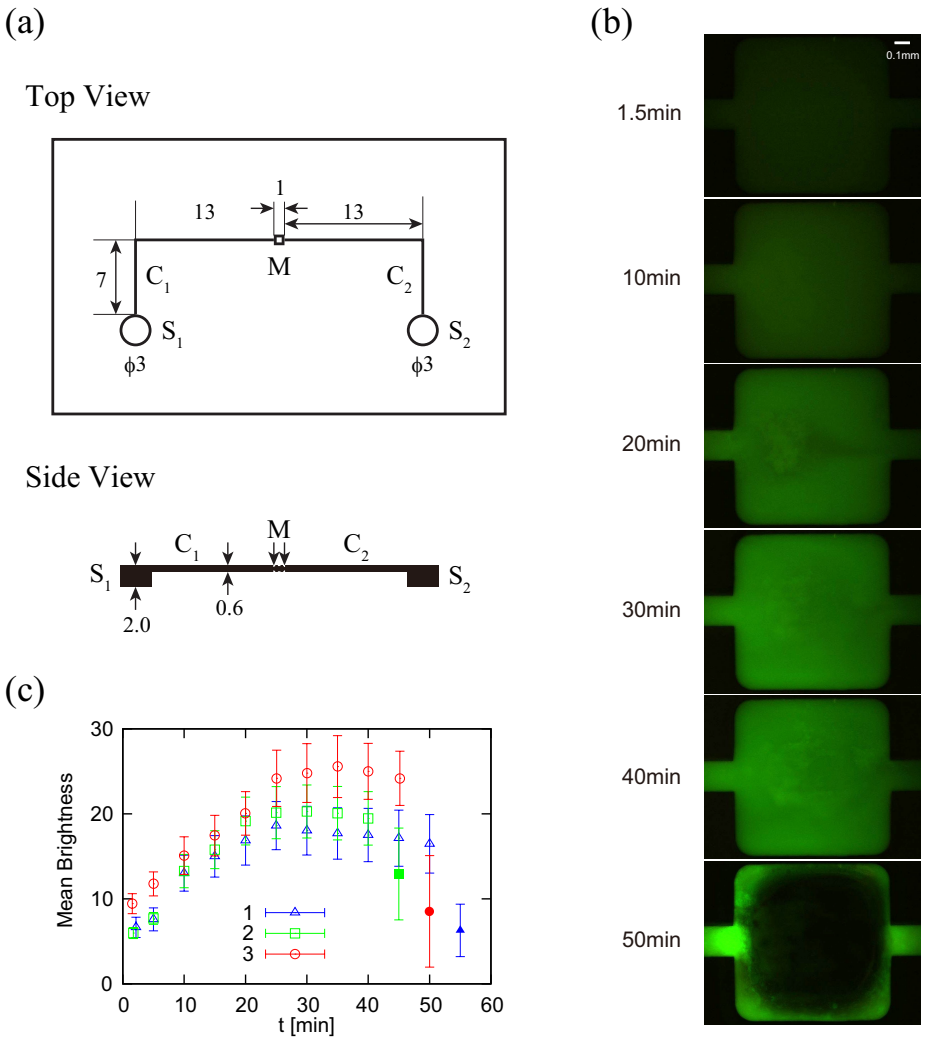

Fig. 7.5. The expression of the green florescence protein (GFP). **(a)** Top and side view of a micro device for mixing two solutions at a mixing spot M. All the numbers are lengths whose units are mm. **(b)** Progress of the expression of GFP in the square-shaped mixing spot M (of the sides 1mm), at which 20mm^3 of Liquid 1 containing DNA, and the same volume of Liquid 2 containing mimicking cytoplasm or protein expression system in bacteria (E.coli), are mixed after they are injected in the circular spots S1 and S2, respectively, at $t = 0$ min. The brightnesses of the snapshot are multiplied by 256/140 times for RGB colors by using Image J to obtained a visible brightness change. The inhomogeneity of the color of the mixing spot M is due to the liquid flow inside the spot. The evaporation is not significant except for the bottom snapshot. **(c)** Mean brightness vs time. The brightness obtained from three independent experiments are plotted as a function of the elapsed time. The data labeled 3 correspond to the experiment shown in the snapshots, and the filled symbols suggest that the liquid in the mixing spot M is almost completely evaporated as seen in the bottom snapshot in (b). All figures are reprinted from [41] Fig.3(b) and supplemental information.

of biochemical reactions in this demonstrations can be estimated as about 30 min. from plateau region in the plot, which is reasonable value considering other reported values in the literature, *e.g.*, [56]. It is to be noted that we did not control temperature during demonstrations, rather there was extra heat caused by the UV light to take pictures.

7.5.3 Advantages and disadvantages of the devices with open capillary

The advantages of our devices, which consist of open-channels and use capillary force as the driving force, are the following: (1) Easier fabrication. The open channels are fabricated on a PMMA plate with numerical controlled micro-milling system outside a clean room. In addition, the sealing by another plate, which is difficult for PMMA, is unnecessary. (2) Durability for reuse and washing. PMMA is mechanically strong than PDMS gel conventionally used for closed-channel devices. Furthermore, our devices are free from adhesion for lids and from connection to a pump system, both of which usually undermine durability of conventional closed-channel devices. Actually, the demonstration for the BTB solution as shown in Fig.7.4 was carried out after the many times of the same experiments on the same device with washing (supersonic washing or simple rinsing by pure water) and/or surface treatment being performed between experiments, which proves a possibility of reuse. (3) Advanced control of wettability. Various effective and repeated surface treatments are available even to the surfaces of the channels, because the surfaces are free from lids and have high durability. Actually, the advanced control (by hydrophilic coating liquid) is performed in the BTB demonstration. (4) Collection of liquids after reactions. The absence of lids gives flexibility for the collection of the liquids from mixing spots. (5) Portability. Our devices use capillary force as driving force, namely our devices do not need any pumps. Thus, the systems can be smaller than conventional ones using pumps, which probably allows us to use them for various purposes such as complex medical tests at a small clinic, outside clinics, or developing countries. (6) Suitability to usages of viscous liquids. We need high-power pumps for usages of high viscous liquids with the conventional devices with pumps, which can become a problem especially in the case of tests of biochemical reactions. On the other hand, we can use viscous liquids as demonstrated with the expression of GFP, only if we can make the surfaces of the channel wettable by the liquids, again

because capillary force is used as the driving force in our devices. Liquid can continue flowing although the flow velocity decreases with increases of viscosity and length of the channels due to the scaling law eq.(7.3).

There are also some disadvantages which should be solved: (1) Evaporation and (2) Contamination, which are caused by the absence of lids, although the evaporation is not effective until around 40 min. in the demonstration of GFP expression as shown in Fig.7.5. These problems can be solved by putting an additional cover on the PMMA plates. The cover should not directly touch with the channels to avoid a flow between the channels and the edges of the cover. (3) Slowing down dynamics. The velocity of the flow of liquids decreases with the scaling law eq.(7.3), differently from an almost constant velocity in the case of devices with pumps. It may become a disadvantage, while the velocity and the time when the liquid arrives at each spot can be calculated from the scaling law eq.(7.3).

It is to be stressed that these advantages indicated above can exceed the disadvantages mentioned above; our open-capillary devices have big capabilities and worth trying to solve disadvantageous points. Although the two demonstrations done here are quite simple examples, more complex and combinatorial devices such as conventional devices used in many microfluidic applications, are available and probably show their capabilities clearly; for studies such as droplet manipulation by flow [57], generation of concentration gradient [58], sorting of particles [59], and mixing [60], in diverse fields including molecular analysis, biodefence, molecular biology and microelectronics [24].

7.5.4 The scaling law as a guiding principle

The scaling law for the imbibition dynamics in the initial regime (eq.(7.3) or eq.(7.4)) plays an important role as a guiding principle to design open-capillary devices such as devices used in two demonstrations; flow velocities or times we need can be predicted almost precisely by the simple scaling law in a wide range of physical parameters. For example, when we need a device for mixing two liquids with different viscosities, we can design it with two different ways based on the prediction from the scaling law: (1) Same channel length and different depositing time. Let us consider the case where the length of the channel C1 and C2 is same, which is similar to the device for the GFP expression, and the liquid 1 (L1) deposited at S1 is more viscous than the liquid 2 (L2) deposited at

S2. In this case, L1 needs longer time to arrive at the mixing spot M. The delay time t_{delay} can be predicted because the time that each liquid needs to arrive at M can be calculated with eq.(7.3). Thus, if we deposit L2 at S2 t_{delay} later than deposition of L1 at S1, we can make both liquids arrive at M at the same time. (2) Different channel length and same depositing time. When we want to deposit both liquids at the same time (in this case, we can use combinatorial pipettes to deposit liquids), we can determine each channel length by calculation with eq.(7.3).

For the width w and depth d of the channels, a standard recommendation would be $w = 0.2$ mm and $d = 0.6$ mm, as employed in our device. As discussed above, we derived the scaling laws for deep channels ($d > w/2$), so that deeper channels are preferable. On the other hand, deeper channels require larger amount of liquids, which is not good especially when the liquids are expensive, for example in the cases of DNA or proteins. As shown in Fig.7.2(b), the initial dynamics of the bulk liquid column for open capillaries whose depth are $d = 0.4$ mm is well on the straight line, namely the deep channel assumption is sufficiently satisfied for $d = 0.4$ mm. Thus, we recommend $d = 0.6$ mm as the depth of the channels with width $w = 0.2$ mm. Here, the width w, roughly the diameter of the drill tip for fabrication, is selected as 0.2 mm because narrower channel needs much time and wider channel needs lager amount of liquids. The actual width and depth of the channel can be slightly different from the desired values which are determined by the drill tip diameter and other milling conditions, and can be inhomogeneous along the channel. Thus, we can determine the actual width as the averaged value calculated from eq.(7.1) with the maximum height of capillary rise of the bulk liquid column, as indicated in sec.7.3.

When one wants to reduce the amounts of liquids, the width w and the depth d should be made smaller even to sub-micrometer. Even in such a case, scaling laws eq.(7.1) and eq.(7.3) still hold although a possible modification may appear when the scales of the channel become close to nanoscales, because small roughness of the surfaces brought about during processes of fabrication are not negligible as discussed in the case of a closed channel [61]. To fabricate devices on sub-micrometer scales, we may have to use a silicon mold made by photolithography to make a sealed channel device with PDMS gel (the seal will be preferable to reduce evaporation for the devices with this scale), which may be appropriate if the cost of liquids is significant.

7.6 Conclusion

We fabricated open capillaries whose cross-sections are rectangular shapes on a PMMA plate by a computer numerical controlled (CNC) micro-milling system. We carried out imbibition experiments; one end of the capillary is touched with the horizontal surface of the liquid bath, here PDMS bath, and then liquid rises up inside the capillary. From the experiments, we found two regions: the bulk liquid column (LC), where capillary is almost completely filled with liquid, and precursor film (PF), which proceeds ahead of the bulk liquid column. For LC, the statics (final height) and both of the initial (viscous) and final (visco-gravitational) imbibition dynamics are well described by simple scaling laws developed with assumptions (complete wetting and rectangular shaped cross-section of LC), and with deep channel approximation, for the wide parameter range. On the other hand, the proceeding of PF scales as $t^{1/3}$ with t being the elapsed time, which is seen for the capillary rise into corners [34] and [35]; the proceeding of precursor film is regarded as the capillary rise into corners of the open capillary, here. Furthermore, to show capabilities of our open capillary, we demonstrated (1) multiple color changes of the BTB solution and (2) the expression of green florescence protein (GFP). Our open-capillary devices do not need adhesion process of lids and any pumps working as driving force, which are advantageous compared with the conventional closed-channel with a pump system, only if we can solve problems such as evaporation or contamination. The simple scaling law for the dynamics of the LC in the initial (viscous) regime can work well as a guiding principle to design open-capillary devices.

Chapter 8

Summary

We studied imibibition of two types of micro-patterned surfaces: one is the surface of a leg of wharf roach and artificial surfaces mimicking it, and the other open-capillary. Combing the conclusion of each chapter, we summarize as follows: for imbibition of the surface of the VIth leg of a wharf roach, we found the characteristic imbibition dynamics; imbibition front seems to start proceeding to the next podite only after the lower podite is almost completely filled, from which might result the unusual non-slowing down dynamics (length scales linearly with time) on a coarse-graind level. Although we could not reproduce the non-slowing down dynamics through imbibition experiments with our artificial surfaces partially mimicking the surface of the leg, we found that imbibition of hybrid surfaces is faster than that of non-hybrid surfaces. Both non-slowing down dynamics and faster imbibition have advantages for transportation of liquids. On the other hand, for imbibition of open-capillary, we confirmed that the statics and both the initial (viscous) and final (visco-gravitational) imbibition dynamics of bulk liquid column, where capillary is almost completely filled with the liquid, are described by respective simple scaling laws. We also found that the proceeding of the precursor film, which proceeds ahead of the liquid column, is obeyed by another scaling law which has been confirmed for capillary rise into corners. In particular, the scaling law confirmed for the imbibition dynamics for the liquid column in the initial (viscous) regime for wide parameter ranges can work as a guiding principle for designing open-capillary devices. Our open-capillary devices without pumps seem to have capabilities of new devices as demonstrated by multiple color changes of the BTB solution and the expression of GFP.

As mentioned in the introduction and the previous studies of imbibition of

micro-patterned surfaces (chapter 5), imbibition dynamics seems to depend on the geometry and size of the textured surface, but the cross-over of exponents appearing in the scaling law has yet to be found; we have not obtained comprehensive understanding. In this work, we experimentally and theoretically studied imbibition of open capillaries whose cross-sections are rectangular shapes. To study imbibition of open capillary with different geometry, *e.g.*, round bottom, round edges etc., is one of future works. I note that this seems to be fundamentally important for understanding imbibition dynamics. Another future work is imbibition of textured surfaces with an imhomogeneous array of micro pillars, or hybrid textured surfaces. These seems to help to find another scaling law which has advantages for liquid transportation.

Finally, it is to be stressed that we should learn much more from nature. Even if we confine our attention to wetting phenomena, there are a lot of animals, insects and plants that have advantages in wettability. Some of them have micro structures on the entire or some part of their surface to get high wettability or better liquid transportation; they know what they should do to obtain tough surface, they know what they should do to transport liquid with low energy, and so on. Learning from them and understanding these mechanism may help us to achieve the world with earth friendly products.

Acknowledgement

I would like to express my deep gratitude to my supervisor Professor Ko Okumura for his fully support. He continuously guides, understands and encourages my research with warm and patients during the coarse of my graduate studies.

I also thank Professor Tetsuo Deguchi, a co-supervisor. He frequently advises me of my research and gives me a lot of valuable comments and encouragement.

Special thanks go out Professor Nozomu Hamaya, Professor Takanori Kono, and Professor Masashi Ban for critical reading of this thesis.

Then, I would like to thank the following researchers: Professor. Daisuke Ishii, Mr. Shuto Ito, Professor Takahiko Hariyama, and Professor Masatsugu Shimomura for the work on capillary rise for a leg of a wharf roach, and Professor Ryuji Kawano and Dr. Koki Kamiya for the work on imbibition of open capillary.

I would like to thank JASSO and Ochanomizu University for their financial support, and JSPS for fellowship for young researchers and KAKENHI.

Finally, I would like to thank group members and my family for their support and encouragement.

Appendix

A Contact angle

A.1 Dynamical contact angle

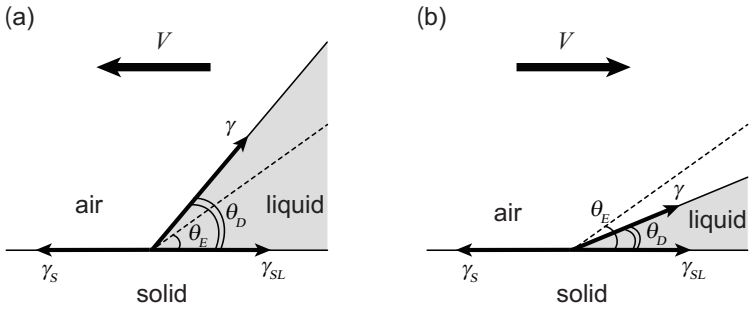

Fig. 1. Dynamical contact angle θ_D and the velocity of the contact line V **(a)** when the contact line advances $\theta_D > \theta_E$, and **(b)** when the contact line recedes $\theta_D < \theta_E$.

In most cases, values of the dynamical contact angle θ_D, which is defined as the angle between liquid and substrate when the contact line (or triple line) moves, are different from those of equilibrium contact angle θ_E, which is defined when the contact line does not move (here the case of contact angle hysteresis is not taken into account). $\theta_D > \theta_E$ when a drop spreads on the substrate (contact line advances), while $\theta_D < \theta_E$ when a drop shrinks on the substrate (contact line recedes) as shown in Fig.1. The dynamical contact angle θ_D depends on $V^{1/3}$ (V is the velocity of the contact line), which is experimentally founded by Hoffman in 1975 for the case of complete wetting ($\theta_E = 0$) [53]. The relation between θ_D and V has been also described theoretically for example in textbook [42], for the case of that $\theta_D > \theta_E$ (contact line advances) and $\theta_D \ll 1$;

$$V = \frac{V^*}{6l}\,\theta_D(\theta_D^2 - \theta_E^2), \tag{1}$$

which yields $V \sim \theta_D^3$ for the complete wetting ($\theta_E = 0$) as reported by Hoffman. In this formula, $V^* \equiv \gamma/\eta$ is characteristic velocity which is comparable to the velocity of capillary rise in viscous region, and l is a numerical number about 15-20 related to the normalized length where viscous dissipation is effective.

A.2 Contact angle hysteresis

(Equilibrium) Contact angle may depend on the way to put the drop. When one makes a drop on a plate by adding liquid, the contact line between liquid and solid does not move for a while, and then suddenly moves. In other words, the contact angle increases for a while, and then suddenly decreases and the drop moves as the contact angle exceeds the higher limit value. This contact angle is called "advancing contact angle" θ_a. On the other hand, when one makes a drop by decreasing liquid, the contact line does not move and the contact angle decreases until the contact angle exceeds the lower limit called "receding contact angle" θ_r. The difference $\Delta\theta = \theta_a - \theta_r$ is called "contact angle hysteresis".

B Tanner's law

Tanner investigated the dynamics of a drop spreading on a substrate in the case of complete wetting; then found a scaling law called Tanner's law,

$$\theta_D \sim t^{-3/10}, \tag{2}$$

where θ_D is the contact angle between liquid (involatile liquid here) and substrate (smooth and clean surface), and t is elapsed time [54, 42]. The fact that θ_D does not depend on the spreading coefficient $S = \gamma_S - \gamma_{SL} - \gamma$ (eq.(2.10)) seems strange because the drop is strained with force which is comparable to S, because the precursor film proceeds ahead of the drop, which was found in another experiment performed by Hardy in 1919 [55]. The precursor film is a few nanometer thickness, and spreads far ahead of the drop. This precursor film is different from that we found in the work mentioned in sec.7.4; Our "precursor film" is much thicker and is caused by capillary rise into corners of the channels.

Reference

[1] W. Barthlott and C. Neinhuis, Purity of the sacred lotus, or escape from contamination in biological surfaces. *Planta* **202**, 1-8 (1997).

[2] B. Bhushan and E. K. Her, Fabrication of Superhydrophobic Surfaces with High and Low Adhesion Inspired from Rose Petal. *Langmuir* **26(11)**, 8207-8217 (2010).

[3] A. R. Parker and C. R. Lawrence, Water capture by a desert beetle. *Nature* **414**, 33-34 (2001).

[4] M. Liu, Y. Zheng, J. Zhai and L. Jiang, Bioinspired super-antiwetting interfaces with special liquid-solid adhesion. *Acc. Chem. Res.* **43**, 368-377 (2009).

[5] P. Bentley and W. Blumer, Uptake of water by the lizard, moloch horridus. *Nature* **194**, 699-700 (1962).

[6] M. Tani, D. Ishii, S. Ito, T. Hariyama, M. Shimomura and K. Okumura, Capillary rise on legs of a small animal and on artificially textured surfaces mimicking them. *PLOSOne* **9(5)** e96813 (2014).

[7] A. Lafuma and D. Quéré, Superhydrophobic states. *Nat. Mater.* **2**, 457-460 (2003).

[8] A. Tuteja *et al.*, Designing superoleophobic surfaces. *Science* **318**, 1618-1622 (2007).

[9] H. Gau, S. Herminghaus, P. Lenz, and R. Lipowsky, Liquid morphologies on structured surfaces: From microchannels to microchips. *Science* **283**, 46-49 (1999).

[10] T. M. Squires and S. R. Quake, Microfluidics: Fluid physics at the nanoliter scale. *Rev. Mod. Phys.* **77**, 977 (2005).

[11] K. -H. Chu, R. Xiao, and E. Wang, Uni-directional liquid spreading on asymmetric nanostructured surfaces. *Nat. Mater.* **9**, 413-417 (2010).

[12] N. A. Malvadkar, M. J. Hancock, K. Sekeroglu, W. J. Dressick and M. C. Demirel, An engineered anisotropic nanofilm with unidirectional wetting properties. *Nat. Mater.* **9**, 1023-1028 (2010).

[13] G. Lagubeau, M. Le Merrer, C. Clanet, and D. Quéré, Leidenfrost on a ratchet. *Nat. Phys.* **7**, 395-398 (2011).

[14] L. Courbin *et al.*, Imbibition by polygonal spreading on microdecorated surfaces. *Nat. Mater.* **6** 661 (2007).

[15] T. Ohzono, H. Monobe, K. Shiokawa, M. Fujiwara and Y. Shimizu, Shaping liquid on a micrometre scale using microwrinkles as deformable open channel capillaries. *Soft Matter* **5**, 4658-4664 (2009).

[16] A. Lafuma and D.Quéré, Slippery pre-suffused surfaces. *Europhys. Lett.* **96**, 56001 (2011).

[17] T. -S. Wong *et al.* Bioinspired self-repairing slippery surfaces with pressure-stable omniphobicity. *Nature* **477**, 443-447 (2011).

[18] X. Dai, B. B. Stogin, S. Yang and T. -S. Wong, Slippery Wenzel State, *ACS Nano* **9(9)**, 9260-9267 (2015).

[19] C. Neils, Z. Tyree, B. Finlayson and A. Folch, Combinatorial mixing of microfluidic streams. *Lab Chip* **4**, 342-350 (2004).

[20] A. Martinez, S. Phillips and G. Whitesides, Three-dimensional microfluidic devices fabricated in layered paper and tape. *Proc. Nat. Acad. Sci. (USA)* **105**, 19606-19611 (2008).

[21] E. C. Jensen *et al.*, Digitally programmable microfluidic automaton for multiscale combinatorial mixing and sample processing. *Lab Chip* **13**, 288-296 (2013).

[22] D. J. Beebe, G. A. Mensing, and G. M. Walker, Physics and applications of microfluidics in biology. *Ann. Rev. Biomed. Eng.* **4**, 261-286 (2002).

[23] H. A. Stone, A. Stroock and A. Ajdari, Engineering flows in small devices: Microfluidics Toward a Lab-on-a-chip. *Annu. Rev. Fluid Mech.* **36**, 381-411 (2004).

[24] G. M. Whitesides, The origins and the future of microfluidics. *Nature* **442**, 368-373 (2006).

[25] M. Schena, D. Shalon, R. W. Davis and P. O. Brown, Quantitative monitoring of gene expression patterns with a complementary DNS microarray. *Science* **270**, 467-470 (1995).

[26] M. Behr *et al.*, Comparative genomics of bcg vaccines by whole-genome DNA microarray. *Science* **284**, 1520-1523 (1999).

[27] D. Gershon, Microarray technology: an array of opportunities. *Nature* **416**, 885-891 (2002).

[28] M. J. Heller, DNA microarray technology: devices, systems, and applications. *Ann. Rev. Biomed. Eng.* **4**, 129-153 (2002).

[29] A. M. Belcher *et al.*, Control of crystal phase switching and orientation by soluble mollusc-shell proteins. *Nature* **381**, 56-58 (1996).

[30] L. Li *et al.*, Nanoliter microfluidic hybrid method for simultaneous screening and optimization validated with crystallization of membrane proteins. *Proc. Nat. Acad. Sci. (USA)* **103**, 19243-19248 (2006).

[31] C. Ishino, K. Okumura and D. Quéré, Wetting transitions on rough surfaces, *Europhys. Lett.* **68**, 419-425 (2004).

[32] C. Ishino, M. Reyssat, E. Reyssat, K. Okumura and D. Quéré, Wicking within forests of micropillars. *Europhys. Lett.* **79** 56005, http://iopscience.iop.org/0295-5075 (2007).

[33] J. Kim, M. -W. Moon, K. -R. Lee, L. Mahadevan and H. -Y Kim, Hydrodynamics of Writing with Ink. *Phys. Rev. Lett.* **107**, 264501 (2011).

[34] A. Ponomarenko, D. Quéré and C. Clanet, A universal law for capillary rise in corners. *Journal of Fluid Mechanics* **666** 146 (2011).

[35] L. -H. Tang and Y. Tang, Capillary rise in tubes with sharp grooves. *J. Phys. II France* **4**, 881, http://jp2.journaldephysique.org/en/ (1994).

[36] N. Obara and K. Okumura, Imbibition of a textured surface decorated by short pillars with rounded edges. *Phys. Rev. E* **86**, 020601(R) (2012).

[37] E. W. Washburn, The dynamics of capillary flow. *Phys. Rev.* **17**, 273-283(1921).

[38] M. Reyssat, L. Courbin, E. Reyssat and H. A. Stone, Imbibition in geometries with axial variations. *J. Fluid Mech.* **615**, 335-344 (2008).

[39] J. M. Bell and F. K. Cameron, The flow of liquids through capillary spaces. *J. Phys. Chem.* **10**, 658-674 (1906).

[40] V. R. Lucas, Ueber das zeitgesetz des kapillaren aufstiegs von flussigkeiten. *Kolloid Zeistschrift* **23**, 15-22 (1918).

[41] M. Tani, R. Kawano, K. Kamiya and K. Okumura, Toward combinatorial mixing devices without any pumps by open-capillary channels: fundamentals and applications. *Sci. Rep.* **5** 10263 (2015).

[42] P. G. de Gennes, F. B.-Wyart and D. Quéré, Capillarity and wetting phenomena: Drops, bubbles, pearls, waves. First Edition (Springer, 2004).

[43] 巽友正，流体力学，初版第 24 刷 （培風館，2011 年）

[44] L. D. Landau and E. M. Lifshitz, Fluid Mechanics. Third Revised English Edition (Pergamon Press, 1966)

[45] S. A. Safran, Statistical Thermodynamics of Surfaces, Interfaces, and Membranes. (Addison-Wesley Publishing Company, 1994)

[46] M. Hamamoto-Kurosaki and K. Okumura, On a moving liquid film and its instability on textured surfaces. *Euro. Phys. J. E* **30**, 283 (2009).

[47] H. Hasimoto, On the periodic fundamental solutions of the Stokes equations and their application to viscous flow past a cubic array of spheres. *J. Fluid Mech.* **5**, 317 (1959).

[48] C. J. Easley, R. K. P. Benninger, J. H. Shaver, W. S. Head, and D. W. Piston, Rapid and inexpensive fabrication of polymeric microfluidic devices via toner transfer masking. *Lab Chip* **9**, 1119 (2009).

[49] T. Cambau, J. Bico and E. Reyssat, Capillary rise between flexible walls. *Europhys. Lett.* **96** 24001 (2011).

[50] E. Spruijt, E. Le Guludec, C. Lix, M. Wagner and D. Quéré, Liquid filmification from menisci. *Europhys. Lett.* **112** 16002 (2015).

[51] H. Horiguchi, M. Hironaka, V. B. Meyer-Rochow and T. Hariyama, Water uptake via two pairs of specialized legs in ligia exotica. *Biol. Bull.* **213** 196-203 (2007).

[52] D. Ishii *et al.*, Water transport mechanism through open capillaries analyzed by direct surface modifications on biological surfaces. *Sci. Rep.* **3** 3024 (2013).

[53] R. L. Hoffman, A study of the advancing interface. I. Interface shape in liquid-gas systems. *J. Colloid Interface Sci.* **50**, 228 (1975).

[54] L. H. Tanner, The spreading of silicone oil drops on horizontal surfaces. *J. Phys. D: Appl. Phys.* **12**, 1473 (1979)

[55] W. B. Hardy, III. The spreading of fluids on glass. *Phil. Mag.* **38**, 49 (1919)

[56] T. Shingaki, and N. Nimura, Improvement of translation efficiency in an escherichia coli cell-free protein system using cysteine. *Protein Expr. Purif.* **77**, 193-197 (2011).

[57] S. L. Anna, N. Bontoux, and H. A. Stone, Formation of dispersions using "flow focusing" in microchannels. *Appl. Phys. Lett.* **82**, 364-366 (2003).

[58] S. K. Dertinger, D. T. Chiu, N. L. Jeon, and G. M. Whitesides, Generation of gradients having complex shapes using microfluidic networks. *Anal. Chem.* **73**, 1240-1246 (2001).

[59] W. -H. Tan and S. Takeuchi, A trap-and-release integrated microfluidic system for dynamic microarray applications. *Proc. Nat. Acad. Sci. (USA)* **104**, 1146-1151 (2007).

[60] W. Du, L. Li, K. P. Nichols and R. F. Ismagilov, Slipchip. *Lab Chip* **9**, 2286-2292 (2009).

[61] W. Stroberg, S. Keten and W. K. Liu, Hydrodynamics of capillary imbibition under nanoconfinement. *Langmuir* **28**, 14488-14495 (2012).